AD-A166 114

Best Available Copy

⑫

DNA-TR-84-212-V1

INVESTIGATION OF THE BASIC MECHANISMS OF RADIATION EFFECTS ON ELECTRONIC MATERIALS AND DEVICES AND DEVELOPMENT OF HARDENING TECHNIQUES
Volume I

Z. Shanfield   J. R. Srour
M. A. Hopkins   R. A. Hartmann
S. Cthmer   D. M. Newberry
Northrop Corporation
Northrop Research and Technology Center
One Research Park
Palos Verdes Peninsula, CA 90274-5471

DTIC
SELECTED
APR 1 0 1986
D

1 December 1983

Technical Report

20030121132

Prepared for
Director
DEFENSE NUCLEAR AGENCY
Washington, DC 20305-1000

DTIC FILE COPY

86 1 31 026

REPORT DOCUMENTATION PAGE

Form Approved
OMB No. 0704-0188
Exp. Date: jun 30, 1986

1a. REPORT SECURITY CLASSIFICATION	1b. RESTRICTIVE MARKINGS
UNCLASSIFIED	

2a. SECURITY CLASSIFICATION AUTHORITY	3. DISTRIBUTION / AVAILABILITY OF REPORT
N/A	Approved for public release; distribution is unlimited.
2b. DECLASSIFICATION / DOWNGRADING SCHEDULE	
N/A since Unclassified	

4 PERFORMING ORGANIZATION REPORT NUMBER(S)	5. MONITORING ORGANIZATION REPORT NUMBER(S)
NRTC 83-25R	DNA-TR-84-212-V1

6a. NAME OF PERFORMING ORGANIZATION	6b OFFICE SYMBOL (If applicable)	7a. NAME OF MONITORING ORGANIZATION
Northrop Corporation		Director Defense Nuclear Agency

6c. ADDRESS (City, State, and ZIP Code)	7b. ADDRESS (City, State, and ZIP Code)
Northrop Research and Technology Center One Research Park Palos Verdes Peninsula, CA 90274-5471	Washington, DC 20305-1000

8a. NAME OF FUNDING / SPONSORING ORGANIZATION	8b. OFFICE SYMBOL (If applicable)	9. PROCUREMENT INSTRUMENT IDENTIFICATION NUMBER
		DNA 001-82-C-0055

8c. ADDRESS (City, State, and ZIP Code)	10 SOURCE OF FUNDING NUMBERS			
	PROGRAM ELEMENT NO	PROJECT NO	TASK NO.	WORK UNIT ACCESSION NO.
	62715H	M99QAXV	A	DH275161

11. TITLE (Include Security Classification)

INVESTIGATION OF THE BASIC MECHANISMS OF RADIATION EFFECTS ON ELECTRONIC MATERIALS AND DEVICES AND DEVELOPMENT OF HARDENING TECHNIQUES: Volume 1

12. PERSONAL AUTHOR(S) Shanfield, Zef; Srour, Joseph R.; Hartmann, Robert A.; Hopkins, Mark A.; Othmer, Siegfreid; and Newberry, Deb M. (Control Data Corporation)

13a. TYPE OF REPORT	13b. TIME COVERED	14 DATE OF REPORT (Year, Month, Day)	15. PAGE COUNT
Technical Report	FROM 820101 TO 830101	831201	96

16. SUPPLEMENTARY NOTATION

This work was sponsored by the Defense Nuclear Agency under RDT&E RMSS Code B323082863 M99QAXVA00004 H2590D.

17	COSATI CODES		18 SUBJECT TERMS (Continue on reverse if necessary and identify by block number)
FIELD	GROUP	SUB-GROUP	Radiation Effects Soft Errors
9	1		Radiation Hardening, Single Event Phenomena,
18	6		Hard Errors : Neutron Damage

19. ABSTRACT (Continue on reverse if necessary and identify by block number)

This report presents results of a study of radiation effects on electronic materials and devices. Emphasis is placed on determining the basic mechanisms of the interaction of radiation with these materials and components with a view toward gaining understanding of benefit to developers of radiation-tolerant devices and circuits. Thermally stimulated current measurements have been performed on irradiated SiO_2 films in order to obtain basic mechanisms information regarding the nature of hole traps at the SiO_2-Si interface. The same activation energies (~ 0.85 and ~ 1.3 eV) were observed in both soft and hard oxides. Hard oxides simply have fewer hole traps than their soft counterparts. The effects of sodium contamination were also examined. Time-resolved charge collection measurements have been performed on GaAs devices bombarded with single 5.0-MeV alpha particles. Preliminary data indicate that charge funneling does occur in GaAs. Results of an experimental and analytical study of the effects of 14-MeV neutrons on silicon are presented. Emphasis was placed on examining whether the permanent damage that results from a single neutron inter-

20. DISTRIBUTION / AVAILABILITY OF ABSTRACT	21. ABSTRACT SECURITY CLASSIFICATION
☐ UNCLASSIFIED/UNLIMITED ☒ SAME AS RPT. ☐ DTIC USERS	UNCLASSIFIED
22a. NAME OF RESPONSIBLE INDIVIDUAL Betty L. Fox	22b. TELEPHONE (Include Area Code) (202) 325-7042	22c. OFFICE SYMBOL DNA/STTI

DD FORM 1473, 84 MAR
83 APR edition may be used until exhausted.
All other editions are obsolete.

18. SUBJECT TERMS (Continued)

Silicon	Hole Traps
Silicon Dioxide	VLSI
Gallium Arsenide	Ionizing Radiation Effects
MOS Devices	Bias-Temperature Stress
Thermally Stimulated Current	

19. ABSTRACT (Continued)

action could cause problems if that damage occurred in a sensitive region of a VLSI circuit. Experimental data obtained on small-geometry pinch resistors, bipolar transistors, and MOS transistors are presented.

TABLE OF CONTENTS

Availability Codes

Dist	Avail and/or Special
A-1	

TABLE OF CONTENTS (Concluded)

LIST OF ILLUSTRATIONS

LIST OF ILLUSTRATIONS (Continued)

LIST OF ILLUSTRATIONS (Concluded)

LIST OF TABLES

SECTION 1

INTRODUCTION

This report presents results of a study of radiation effects on electronic materials and devices. Emphasis is placed on determining the basic mechanisms of the interaction of radiation with these materials and components with a view toward gaining understanding of benefit to developers of radiation-tolerant devices and circuits. The work performed under Contract DNA 001-82-C-0055 is reported in the present document (Volume 1) and in a companion report (Volume 2). (Volume 2 is authored by A.H. Kalma, S. Othmer, M.A. Hopkins, R.A. Hartmann, and J.R. Srour.) In Section 2 of the present report, results of thermally stimulated current measurements on irradiated MOS capacitors are presented. Section 3 describes the initial results obtained in a study of soft errors in GaAs devices. In Section 4, findings obtained in an investigation of neutron-induced effects in VLSI structures are given. The remainder of the present section summarizes the major findings reported in this document.

Thermally stimulated current (TSC) measurements have been performed on irradiated SiO_2 films in order to obtain basic mechanisms information regarding the nature of hole traps at the SiO_2-Si interface. A comprehensive set of pre- and post-irradiation TSC measurements were made on MOS capacitors in this investigation. We observed pre-irradiation bias-temperature instabilities, both for negative and positive bias. The same activation energy (~ 1 eV) was noted for both positive and negative charge carriers. For "hole traps" in irradiated devices, the same activation energies (~ 0.85 and ~ 1.3 eV) were noted in both soft and hard oxides. Hard oxides simply have less traps than their soft counterparts. There appears to be an "intrinsic" hole trap at ~ 1.3 eV, possibly consisting of charged traps with a number of different activation energies. If the oxide has Na^+ contamination and those ions are moved to the Si-SiO_2 interface, there is an additional "hole trap" at ~ 0.85 eV.

Time-resolved charge collection measurements have been performed on GaAs devices bombarded with single 5.0-MeV alpha particles. This investigation was initiated to determine the relative roles of drift and diffusion in the charge collection process and to determine whether charge funneling occurs. Such information is needed to evaluate the susceptibility of GaAs devices to soft

7

errors and as a first step toward developing hardening techniques. Preliminary charge collection measurements indicate that funneling does occur in GaAs. Further work in this area will be performed under Contract DNA 001-83-C-0108.

An experimental and analytical study of the effects of 14-MeV neutrons on silicon devices has been performed. Emphasis was placed on examining whether the permanent damage that results from a single neutron interaction could cause problems if that damage occurred in a sensitive region of a VLSI circuit. Determination of the energy and angular distributions of primary knock-on atoms in 14-MeV neutron-irradiated silicon was made. These distributions were employed in a distributed cluster model that was used in an attempt to account for measured resistance changes in irradiated pinch resistors. Neutron irradiations of small-geometry bipolar transistors were also performed. Electrical measurements were dominated by damage produced in the extrinsic base region. An approach was developed for determining the effect on current gain of a single interaction in the intrinsic base region, and such experimentally-based calculations are planned. Neutron irradiations on MOS/VLSI transistors were performed. Observed threshold voltage shifts appeared to be largely attributable to background ionizing radiation present during the neutron irradiations. Slope changes were noted occasionally in plots of threshold voltage shift versus neutron fluence. Further study is needed to determine whether these slope changes are attributable to neutron interactions, to ionizing radiation, or to device instabilities.

SECTION 2

THERMALLY STIMULATED CURRENT MEASUREMENTS
ON IRRADIATED MOS CAPACITORS

2.1   INTRODUCTION

The degradation of silicon MOS devices by ionizing radiation[1] is a well-known phenomenon which has been studied extensively.[2] Ionizing radiation interacts with SiO_2 layers resulting in the generation of holes that are preferentially trapped near the $Si-SiO_2$ interface and the generation of interface states. These radiation-induced effects cause threshold voltage shifts and other unwanted changes in device characteristics. Once the nature of hole traps and interface states is determined and the device processing procedures necessary to control them are developed, it should be possible to "engineer" the hardness of integrated circuits and thereby realize ultrahard MOS devices.

The purpose of the present investigation is to provide basic information regarding the nature of hole traps in irradiated MOS devices. Even though much work has been done to elucidate the nature of hole traps, uncertainty still exists regarding their microscopic properties, the differences between radiation-soft and radiation-hard oxides, and the effects of various processing steps. A comprehensive series of thermally stimulated current (TSC) measurements on irradiated oxides was undertaken to determine the density of trapped holes and their associated thermal activation energies. These measurements were performed on MOS capacitors in conjunction with conventional capacitance-voltage (C-V) techniques in order to monitor the amount of charge in the oxide. In order to obtain a coherent view of the nature of radiation-induced trapped charge at the $Si-SiO_2$ interface, analysis of the effects of pre-irradiation bias-temperature stressing as well as the radiation-induced trapped charge was necessary.

During the initial phase of the investigation, the experimental technique was established and demonstrated using MOS capacitors fabricated at NRTC. Additionally, a mask set for the fabrication of the full matrix of samples was furnished by NRTC to the Center for Radiation-Hardened Microelectronics (CRM) at Sandia National Laboratories. Here we report the initial results of measurements on these samples. In Section 2.2, a summary of hole

9

trap characteristics obtained from various measurement techniques is presented. Section 2.3 reviews the theory of the TSC technique and its interpretation; details of the experimental method are presented in Section 2.4. Results are discussed in Section 2.5 and conclusions are given in Section 2.6.

The investigation of hole trap properties using TSC measurements will continue in our laboratory in 1983 under Contract DNA 001-83-C-0108. Much of the information presented here is preliminary and is essentially an interim report.*

2.2 BACKGROUND

A number of different measurement approaches and techniques have been applied in the past to identify the nature of hole traps in SiO_2 films, including annealing studies, thermoluminescence, photodepopulation, and thermally stimulated current (TSC) and capacitance. Various experiments have also been conducted to correlate the introduction rate of trapped holes with oxide growth parameters and other characteristics such as mobile ion concentrations.

A variety of annealing results have been obtained. Woods and Williams[3] reported the disappearance of trapped positive charge in irradiated MOS devices after anneals above 150°C. Aitken[4] found that 80% of the radiation-induced charge is removed upon annealing to 400°C. Regarding the activation energy for the release of trapped holes, a variety of values have been reported. Nicollian et al.[5] quote an activation energy of 0.35 eV. Lindmayer[6] found activation energies to range from 1.3-1.5 eV. Using isothermal annealing coupled with capacitance measurements, Manchanda et al.[7] found an activation energy for hole detrapping of 1-1.5 eV. Bakowski[8] performed thermally stimulated current measurements on dry and wet oxides and found two values of activation energy, one in the range of 0.8-1.3 eV, and the other 1.8-2.4 eV. (The method employed by Bakowski to extract activation energies differed from that employed here and is believed to be in error. If the present method were applied the calculated activation energies for his data would be considerably smaller (by as much as 40%).

---

*For an updated description of TSC measurements on irradiated MOS capacitors, the reader is referred to a paper by Z. Shanfield in the December 1983 issue of the IEEE Transactions on Nuclear Science.

Hughes and Thomas[9] performed extensive TSC measurements in a study which compared hard and soft, dry and wet oxides using several diagnostic techniques. The wet oxide specimens appeared to be dominated by mobile ion contributions to the thermally stimulated current. Dry oxides, which were not thus affected, did not exhibit the structure in the TSC response observed by Bakowski.[8] Sampl behavior was also found to be altered by pre-irradiation bias-temperature stressing.

In contrast to the above results, optical measurements of the photo-ionization cross section of trapped holes have consistently yielded no photo-depopulation of the trapped charge. Harari, Wang, and Royce[10] were unable to photodepopulate hole traps in measurements performed at 77 K with photons up to 5 eV in energy. Snow, Grove, and Fitzgerald[11] found the threshold for the disappearance of trapped holes to be 4.3 eV, which is the energy at which electron excitation from the silicon valence band to the SiO_2 conduction band becomes energetically allowed (internal photoemission). It is quite likely that neutralization of trapped holes occurred rather than photodepopulation.

Grunthaner et al.[12] and others[13] have used XPS and other spectroscopic techniques to identify the local chemical nature of the $Si-SiO_2$ interface. They have found a very abrupt chemical interface (one monolayer or less) and a bond strain region extending ~30 Å into the oxide. They correlated the radiation hardness of the oxide with the extent of this bond strain region, with harder oxides having less strain. They proposed a model in which the ionizing radiation breaks a strained bond leaving a Si^+ site, which is the trapped hole, and a mobile nonbridging oxygen (NBO) that propagates, by the action of the strain gradient, toward the interface. In their model, if the NBO reaches the interface it generates an interface state.

2.3 THEORY

The TSC method is one of a number of techniques based on thermally stimulated relaxation (TSR)[14] phenomena which includes TSCAP, thermally stimulated exoemission, emission time spectroscopy, and DLTS. These techniques have been used for many years in the study of solids.[15] Also included are thermally stimulated luminescence (thermoluminescence or "glow curves") in which electron traps are depopulated in insulators[16] and, more recently, the use of thermally

stimulated ionic currents (TSIC) in studies of ionic impurities in SiO_2 and Al_2O_3.[17] Thermoluminescence is also a standard technique for radiation dosimetry. The extension of the thermally stimulated current technique to the study of hole traps in SiO_2 films is a straightforward application of previous work.

A TSC measurement is made by applying a bias across the insulator in an MOS capacitor (Figure 1a) and recording the current as the sample temperature is raised (Figure 1b). The measurement is repeated in order to determine the background current which is attributable to carrier injection and displacement currents and is unrelated to the thermal depopulation of traps. The difference between the two currents is interpreted as arising from the thermal depopulation of charged traps. The fact that both trapped electrons and holes may be present, that discrete and continuous trap levels may exist, and that recombination and retrapping processes can occur complicates the analysis. Since hole trapping predominantly occurs very near the Si-SiO_2 interface in thermally grown SiO_2, for a sufficiently high applied field retrapping can be ignored, thereby eliminating these complications. In the present case of irradiated thermal SiO_2, hole traps have much larger capture cross sections than electron traps so the TSC spectra should predominantly reflect the release of trapped holes.

The simplified rate equation governing the depopulation of traps is

$$\frac{d n_t}{dt} = -n_t \nu e^{-\Delta E/kT(t)} , \qquad (1)$$

where n_t is the occupied trap density, ν is the "attempt-to-escape" frequency, ΔE is the activation energy of the detrapping process, and T is the temperature in Kelvins, which is a function of time. In general, an analytic solution of this equation does not exist. However, as shown by Hickmott[17] for TSIC studies with discrete energy levels, a hyperbolic temperature ramp allows an analytic integration of the rate equation. For high-field TSC using a linear temperature ramp, Simmons and coworkers[18] have shown that the TSC spectrum is, to a good approximation, a direct image of the energy distribution of occupied traps when retrapping does not occur. For a linear temperature ramp with a constant rate β, the sample temperature is given by

$$T = T_0 + \beta t , \qquad (2)$$

12

(a)

(b)

(c)
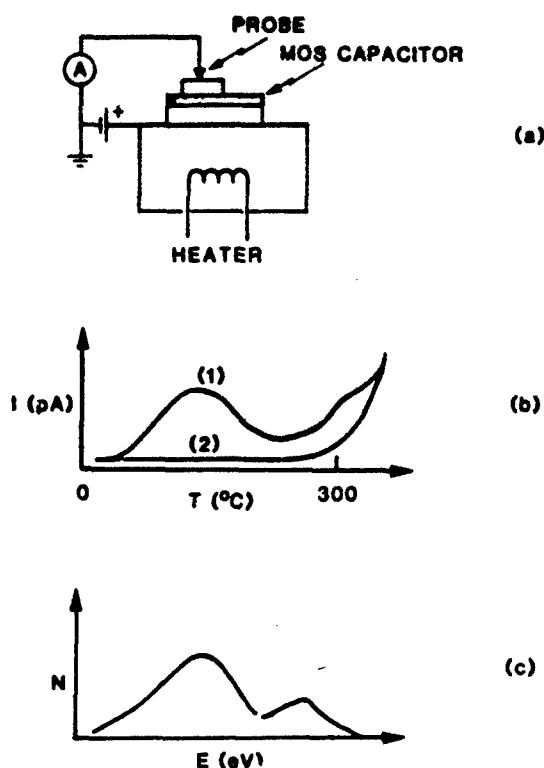
Figure 1. Schematic representation of the TSC technique: (a) experimental con-
figuration; (b) example plots of experimental currents where (1) is
the first measurement (called "data") while (2) is the second measure-
ment (called "baseline") made immediately after (1) is taken and the
device is allowed to cool; (c) resultant TSC spectrum.

where T_0 is the initial temperature and t is time. The measured current is
recorded as a function of temperature; a representative curve is shown in Fig-
ure 1b(1). A second measurement is made to establish the baseline (Figure
1b(2)). The TSC spectrum is the difference between the two currents (Figure 1c).
For a distribution of occupied hole traps, $N(\Delta E)$, where N has dimensions of
traps/cm$^3 \cdot$eV, the current per unit area I is given by

$$I = \frac{1}{2} qLD \, N(\Delta E) \quad , \tag{3}$$

where q is the electronic charge, L is the thickness of the insulating layer,
and

$$D = 1.2 \, \beta \, \Delta E/T \quad . \tag{4}$$

The energy scale (eV) is linearly related to temperature by

13

$$\Delta E = T(1.92 \times 10^{-4} \log \frac{\nu}{\beta} + 3.2 \times 10^{-4}) - 0.0155 \quad . \tag{5}$$

Because the dependence of ΔE on ν is weak, the specific value of ν used is not critical. A value between 10^{10} and 10^{12} sec^{-1} is usually taken. In this analysis 10^{11} sec^{-1} was used. Explicit determination of the best value is possible by measuring the spectra at two different ramp rates, β_1 and β_2, and measuring the temperatures, T_1 and T_2, at which a prominent peak occurs. The emission rate, ν, is then calculated from $\nu = 10^y$ where

$$y = \frac{T_2 \log \beta_2 - T_1 \log \beta_1}{T_2 - T_1} - 1.66 \quad . \tag{6}$$

2.4 EXPERIMENTAL TECHNIQUE

During 1981 the feasibility of the TSC technique for studying irradiated MOS capacitors was established and the experimental methodology, equipment, and analysis were developed. Here we present a summary of the experimental technique. A number of modifications regarding sample mounting and electronics were made in 1982 which are also discussed.

A necessary requirement for a successful TSC measurement is sensitivity to picoampere currents in the presence of a noisy environment arising from the heater and thermal ramp circuits. To meet this requirement, very careful isolation and grounding was needed. It is necessary that no extraneous current be measured. This necessitates the use of a probe in order to couple the sample under test to the current measuring circuit. The probe was mounted on its own stand, thereby electrically isolating it from the sample except for the probe tip in contact with the gate electrode.

The experimental apparatus is shown in Figure 2. This apparatus was used for both TSC and C-V measurements. A schematic diagram of the TSC system is shown in Figure 3. Note that two independent heater circuits were used, one of which was connected to a dc supply and the other of which was connected to a servo circuit. Additionally, independent thermocouples were provided for measurement and control. To assure thermal integrity the measurement thermocouple was thermally lagged to the sample block, and for maximum thermal response frequency the control thermocouple was imbedded in the sample block.

14

Figure 2. Experimental TSC apparatus incorporating probe contacts to MOS test samples.
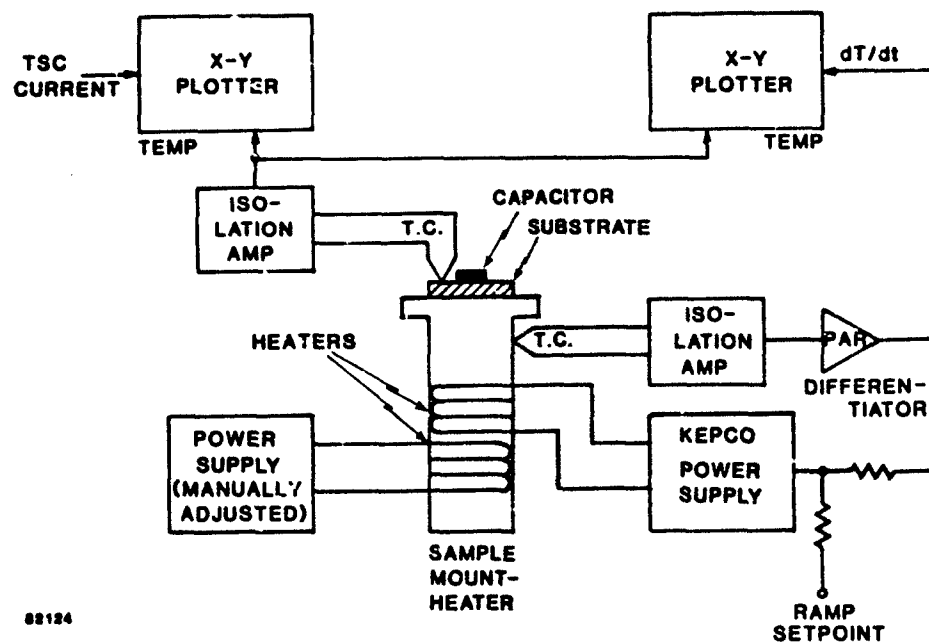
Figure 3. Diagram of the final TSC system.

15

Samples were die-attached to gold-chrome metallized 25-mil alumina substrates, which were in turn clamped to the copper surface of the sample block by means of lugs fabricated from machineable ceramic (Figure 4). The measurement thermocouple was clamped to the substrate using one of these lugs, and the metallization was scribed using a diamond saw in such a way as to maintain electrical isolation of the thermocouple from the current measurement circuit. The bias supply wire was then clamped under the other lug. An Everett/Charles spring contact probe with pointed tip was found to produce a good electrical contact without damaging either the probe or the sample.

Initially, samples were bonded to the gold-chrome metallized substrate using a Cu adhesive which was cured at low temperature. TSC measurements resulted in rapid electrical failure of the samples. It is believed that diffusion of the Cu into the semiconductor occurred, although this point was not investigated. The problem was resolved using die attachment with a low-ionic-impurity, silver-filled epoxy which was stable to the maximum temperature reached during TSC measurements.

TOP VIEW
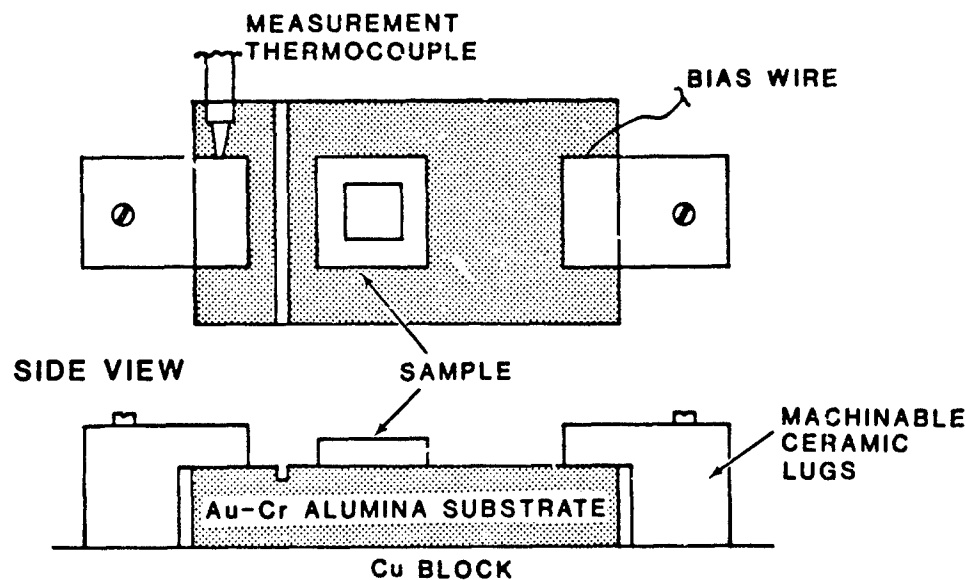
Figure 4. Sample mounting configuration.

16

The circuits employed for linear sample heating control are shown in Figure 5. The derivative of the temperature is obtained by use of the high-pass filter on the PAR 113 preamp. The amplified signal from the control thermocouple is summed with the manually adjustable setpoint voltage at the summing junction of a Kepco power operational amplifier which supplies power to the control heater. The measurement thermocouple was mounted on an alumina substrate for isolation. The setpoint voltage could be adjusted as necessary to maintain constant temperature derivative, as monitored by means of an X-Y plotter. The manually adjusted bias heater determined the dynamic range of the control system. The temperature ramp procedure was the following: 1) establish the appropriate setpoint for the closed-loop control system, and 2) increment the bias heater supply as necessary in order to maintain reasonably stable output on the Kepco operational amplifier. A TSC run required about 15 minutes under the chosen conditions of ramp rate (0.3°C/sec).

The current measurement was made using a Keithley 616 digital electrometer operating in the fast (feedback) mode. The capacitor substrate was biased to +3.0 V during TSC measurements. The output of the electrometer was fed to the Y input of one of the X-Y recorders. The C-V and G-V measurements were made using a PAR Model 410 C-V plotter operating at 1 MHz with 15 mV modulation signal. A typical voltage ramp rate used was 0.2 V/sec.

As mentioned previously, a critical requirement was careful grounding of the total TSC system. The heater circuit and the current measuring circuit were completely isolated from each other except at power ground and at the X-Y recorder used for gathering the TSC current vs temperature data (Figure 5). For the current measurement circuit, ground was the Keithley 616 case, with all other components kept floating. All parts of the vacuum shroud of the experimental apparatus (Figure 2) were electrically connected so that induced currents were returned directly to the case of the electrometer. Even with these precautions, 60 Hz low-pass filters were necessary on the inputs of the X-Y recorder in order to minimize pickup from equipment operating in the vicinity of the experiment (i.e., Northrop TRIGA reactor facility).

The MOS capacitors were irradiated at the Northrop Co-60 source. Initially the samples were irradiated in the measurement apparatus. However, noisy leakage currents were observed from insulators in that apparatus.

17
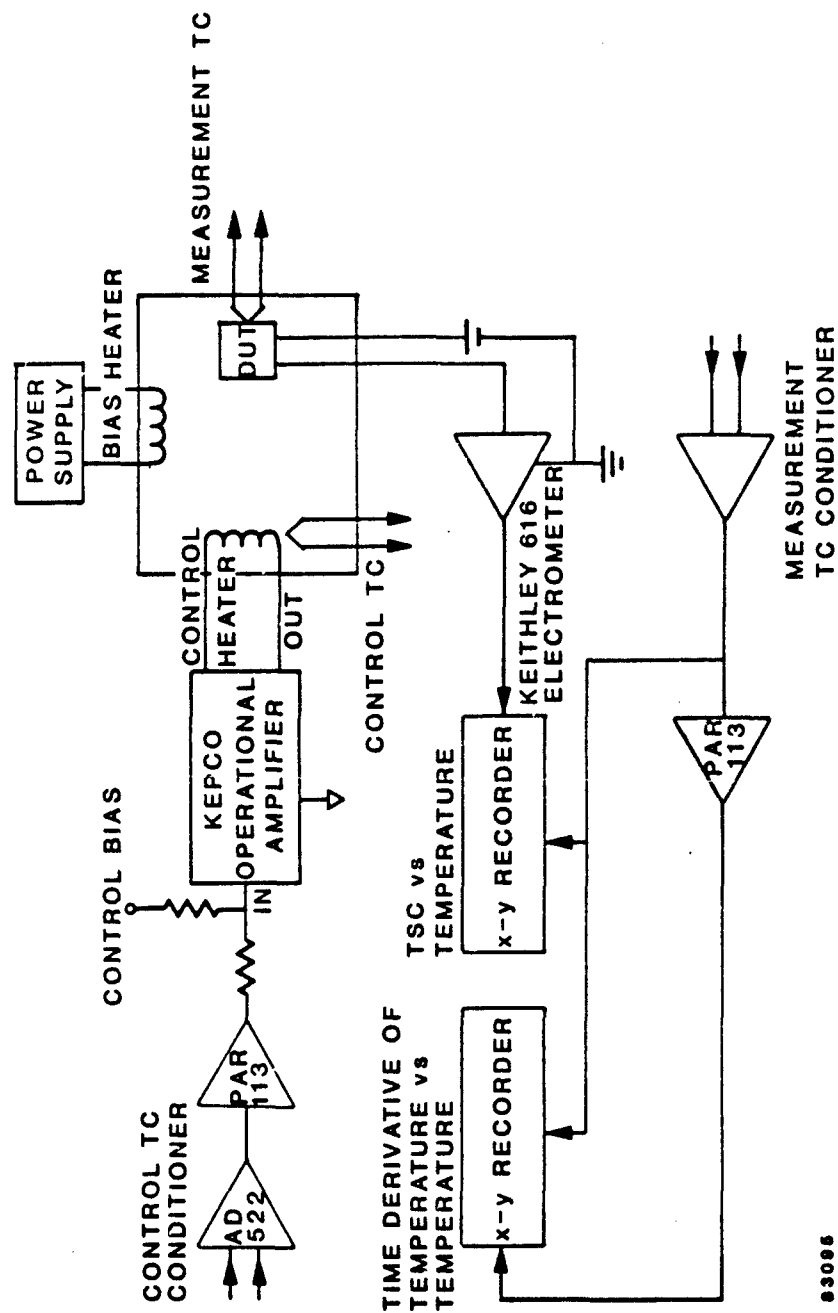
Figure 5. Diagram of circuit used for TSC measurements and control.

18

A separate fixture which allowed the irradiation under bias of up to four samples was built. The metallized alumina substrates to which capacitors were die attached was clamped under a brass lug which was wired into the biasing circuit. A probe contacted the Al-gate electrode of an MOS capacitor. All irradiations were made at room temperature in air with a positive gate bias of 7 volts. Irradiation doses ranged from ~0.25 Mrad(Si) to ~1.25 Mrad(Si) at a dose rate of ~80 krad(Si)/hr. Dosimetry measurements were made using a small ion chamber mounted to the irradiation fixture at the location where samples were usually mounted.

During this study, a variety of measurement sequences was undertaken for different samples. For many capacitors, a sequence of TSC measurements was made before irradiation with both positive and negative bias. If pre-irradiation TSC measurements were made, the final pre-irradiation TSC run always was made under negative gate bias to move any positive ionic charge to the gate electrode. For other devices, irradiation was the first step in the sequence. In all cases, the charging of hole traps was produced by Co-60 gamma-ray irradiation at room temperature under positive gate bias. Conventional C-V measurements were made before and after each irradiation and each TSC run. The observed negative flatband shift is indicative of the trapping of positive charge. Once the hole traps were charged, TSC measurements were made. During the measurement, holes trapped near the $Si-SiO_2$ interface were thermally released as the device temperature was raised. With a negative bias applied to the gate electrode, these holes were swept toward the gate and produced current peaks in the TSC spectrum. This process, which is equivalent to negative bias-temperature stressing, also caused a positive flatband voltage shift in C-V measurements, which is indicative of the release of trapped holes.

Devices were fabricated at Sandia National Laboratories. Two separate device lots prepared by Sandia were investigated; all devices in both lots were prepared on n-type Si of (100) orientation, and all had 1 mm^2 Al gate electrodes (except for a portion of the devices in the first lot which had poly-Si electrodes). Dry oxides were grown at 1000°C to a thickness of approximately 700 Å, while pyrogenic oxides were steam grown at 900°C. All samples were annealed at 450°C in nitrogen after metallization. To produce the radiation-soft samples, certain wafers were annealed in nitrogen at 1100°C for 30 minutes.

The first lot included capacitors with pyrogenic and dry oxides (both soft and hard). TSC and C-V measurements revealed that these samples contained mobile ions with a density of 10^{11} to 10^{12} cm^{-2}. The observed pre-irradiation TSC spectra were typical of those reported in the literature for oxides containing Na ions and possibly K ions.[17] The second lot studied consisted of only dry oxide devices (again both hard and soft). These samples showed no ion contamination within the sensitivity of the measurements. Triangular voltage sweep (TVS) measurements made at Sandia indicated mobile ion concentrations below 10^{10} cm^{-2}.

2.5 RESULTS AND DISCUSSION

The first samples received from Sandia were wet oxide capacitors from lot 1. As described above, use of the Cu adhesive resulted in rapid sample failure so that no useful TSC data were obtained. Once the Ag-filled epoxy was used for mounting samples, well-defined TSC peaks were observed in the data. Both irradiation and TSC measurements were initially made in the same apparatus. The data was often noisy and difficult to reproduce. Once a separate irradiation fixture was built, reproducible data were obtained. Representative spectra are shown in Figure 6 for two radiation doses for the same sample. Before irradiation, both positive and negative gate bias TSC measurements were made. The peaks observed in these spectra are discussed below. The peak at ~ 0.85 eV was clearly visible and was located on a very flat baseline. At higher temperatures ($>295°$C), the baseline current rapidly increases due to <u>thermal</u> injection of charge into the SiO$_2$. Even though most of the broad peak at ~ 1.3 eV lies well below this region, large uncertainties regarding this peak initially existed. These uncertainties resulted from the less than optimum reliability of the first samples studied and the frequent breakdown which occurred until limits were placed on the bias applied to the sample and the maximum temperature and TSC current that was allowed before a measurement was terminated. Once limits were placed on the operating parameter, especially the maximum TSC current, the ~ 1.3 eV peak became very reproducible.

Results of C-V and TSC measurements are discussed below. First, pre-irradiation effects are reported including the effects of ion contamination in lot 1 samples and the bias-temperature instability observed in lot 2 samples. Next, irradiation effects are described, both intrinsic effects and those associated with the presence of ions.

20

TEMPERATURE (°C)

WET HARD Al GATE I-5-5
Na CONTAMINATED
PRE-CLEANED
(A) 1.3 Mrad(Si)
(B) 0.15 Mrad(Si)
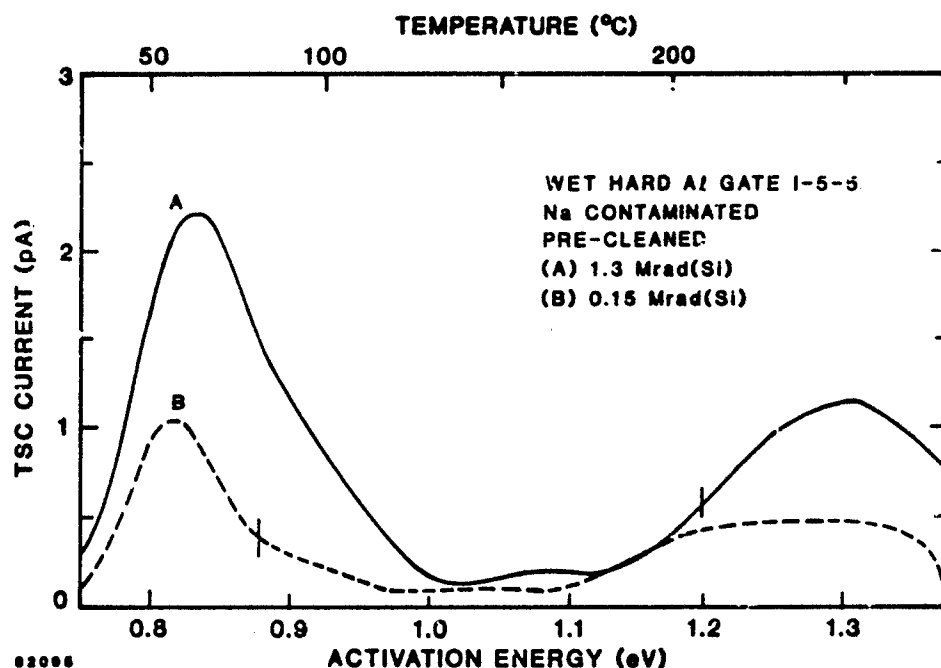
Figure 6. TSC spectrum of an irradiated pyrogenic, Na contaminated Al
gate MOS capacitor. Precleaning indicates that Na had been
moved to and then away from the Si-SiO$_2$ interface.

2.5.1 Pre-Irradiation Effects

Pre-irradiation TSC and C-V measurements were made to evaluate the degree
of mobile ion contamination in the present samples. This is equivalent to bias-
temperature (BT) stressing. As mentioned above, a mobile ion concentration of
10^{11} to 10^{12} cm^{-2} was found for samples from lot 1. For lot 2 samples, mobile
ion concentrations were below the sensitivity of these measurements; however,
a bias-temperature instability (often called a slow trapping instability)[19]
was observed for this lot.

2.5.1.1 **Mobile Ion Motion.** Measurements on lot 1, including both dry and
pyrogenic oxides, revealed appreciable mobile ion contamination. TSC measure-
ments showed the typical peaks and energies reported in the literature for
other studies of ion-contaminated SiO$_2$ using thermally stimulated ionic cur-
rents (TSIC).[20] In Figure 7 typical results of TSC measurements on Al gate,
lot 1 samples are shown. Curve A shows the first TSC spectrum for ion motion
from the Al gate electrode toward the Si-SiO$_2$ interface, while Curve B is the
current for ions returning from the Si-SiO$_2$ interface toward the gate electrode.
The peak between 0.8 and 0.9 eV is associated with Na$^+$ ions while the very
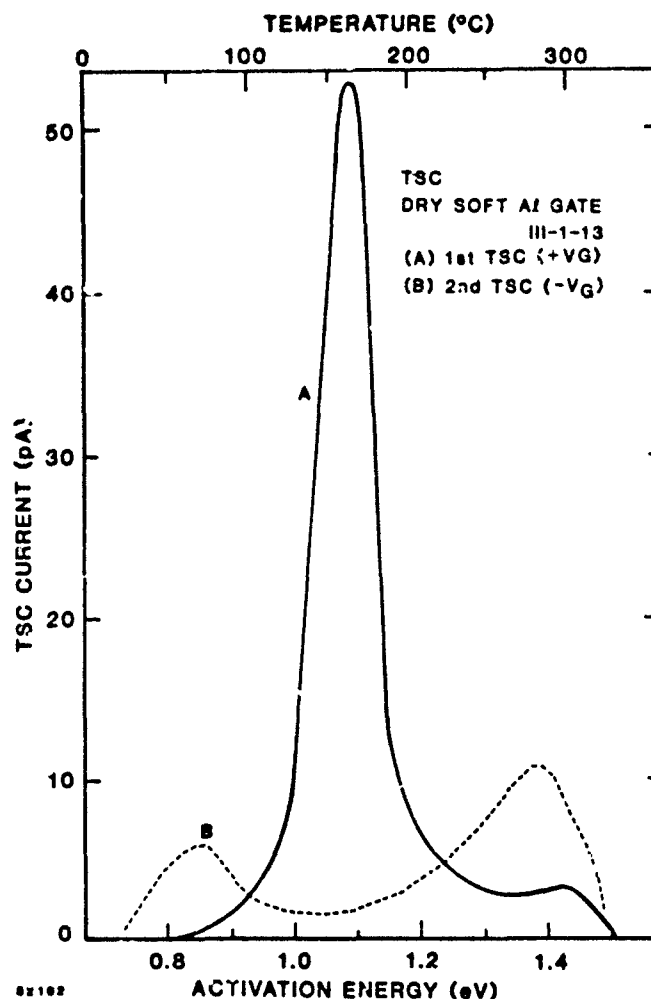
Figure 7. TSC spectrum of an unirradiated MOS
capacitor. See text for details.

broad peak around 1.3 eV has previously been assigned to K^+ ions.[21] If the initial TSIC is made under positive bias, a peak at ~ 1.1 eV is found, while little or no current occurred if made under negative bias. This indicates that most of the ion contamination was initially near the gate electrode.

As shown in Figure 6, one of the predominant irradiation peaks occurs at the same energy as the Na^+ TSIC peak (~ 0.85 eV). Because of the long irradiation times, it is possible that the Na^+ located at the gate electrode could migrate at room temperature to the $Si-SiO_2$ interface under the positive irradiation bias and be the cause of the ~ 0.85 eV peak. To test this conjecture,

22

the following experiment was conducted. First, positive and negative gate
bias TSC measurements were conducted leaving the ions at the Al gate electrode.
Figure 8, Curve A shows the final TSC spectrum obtained under negative bias.
The sample was next placed under the same positive bias that would be used for
irradiation, but not irradiated. A negative-bias TSC measurement was then
made as if the sample had been irradiated. The results are shown in Curves B
and C of Figure 8 for two different biasing times. A small amount of Na^+ does
drift back to the $Si-SiO_2$ interface, but much less than that which is moved
during the TSC measurement and an order of magnitude less than the current ob-
served in the ~0.85 eV irradiation peak.

A pre-irradiation TSC measurement was also made on one poly Si gate capaci-
tor from lot 1. The results (Figure 9) show large currents. Because of the ion
contamination problem associated with the Al gate samples from lot 1, no further
investigation of these samples was undertaken.

A summary of pre-irradiation results of measurements on the lot 1 samples
is given in Table 1. The energy maxima in the TSC distributions are listed
along with the amplitude ratios of the TSC peaks normalized to the lowest tem-
perature peak in each spectrum. The column labeled interface specifies from
which interface the ions are released. The ratio of the charge determined from
the C-V flatband shift to that determined by integrating the TSC current should
be considered only an estimate. The high energy side of the higher temperature
peaks extends into the region where the baseline current is increasing rapidly.
Since the subtraction of peaks from the baseline in this region often involves
small differences between large numbers, large uncertainties can arise. The
temperature at which injection occurs also varies, possibly depending on oxide
space charge distributions and oxide damage. The total charge contained in
current peaks that extend significantly into this region can have uncertainties
of at least a factor of two even though the peak positions are known to much
greater accuracy.

2.5.1.2 <u>Bias-Temperature Instability</u>. C-V characteristics associated with
the BT instability in lot 2 samples are shown in Figure 10. The result of a
<u>negative</u> BT stressing, produced by a negative TSC measurement, is to produce a
<u>negative</u> flatband voltage shift (curve A to B). For <u>positive</u> BT stressing,
also produced by a TSC measurement but with positive bias, a very small positive
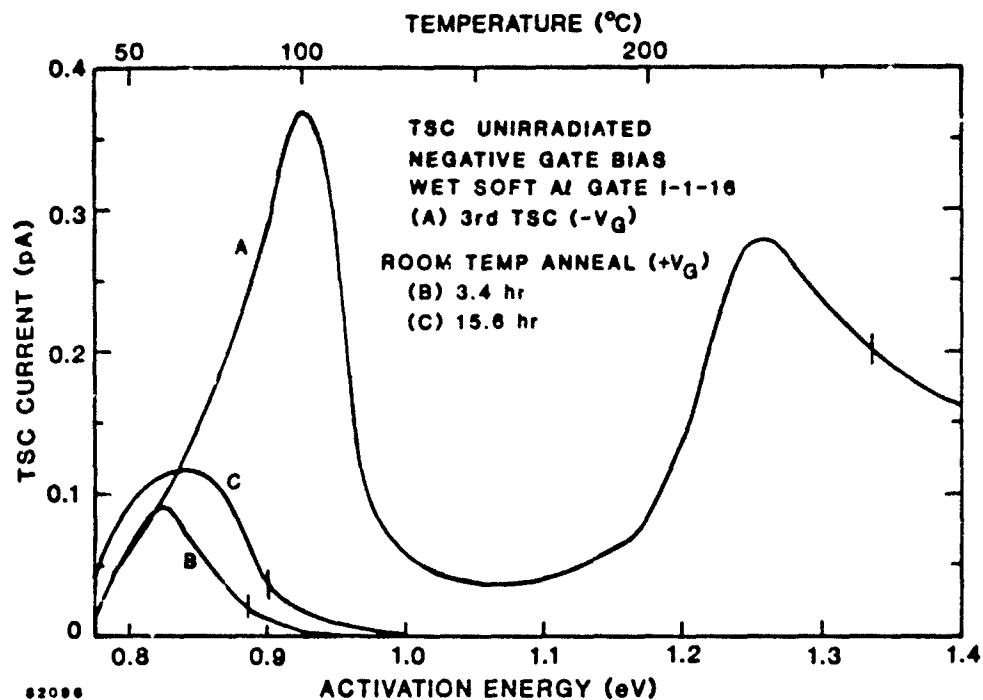
Figure 8. TSC spectrum of an unirradiated MOS capacitor.
See text for details.
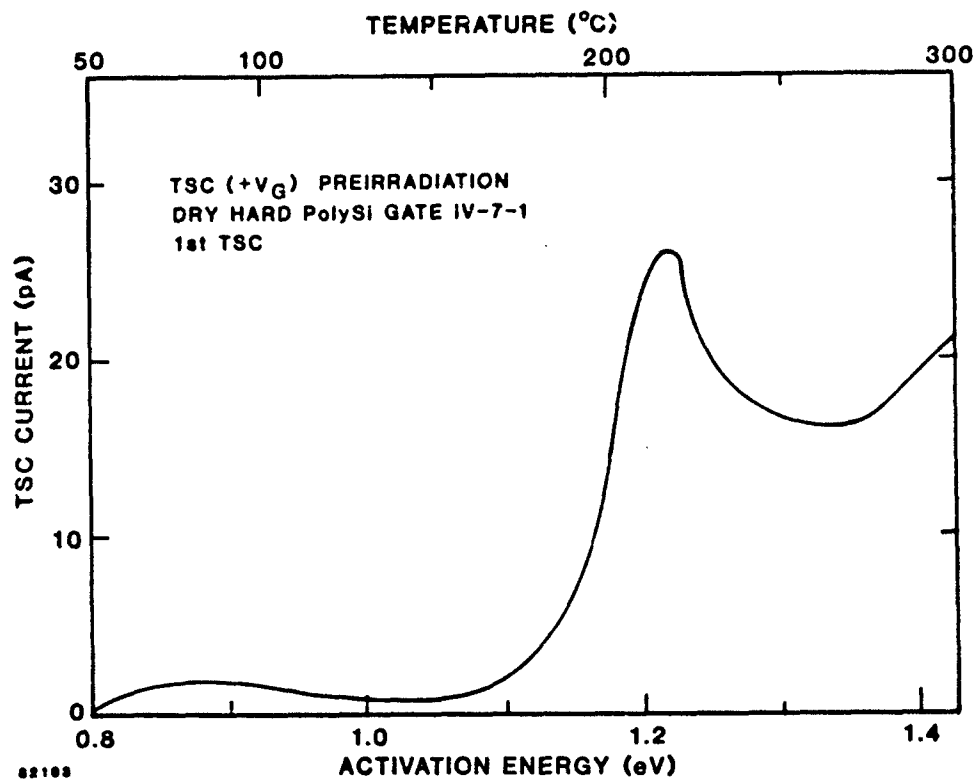
Figure 9. TSC spectrum of an unirradiated polysilicon-gate MOS capacitor.

24

Table 1. Results for unirradiated Sandia MOS capacitors.

Al GATE		POLY Si GATE	INTERFACE
Wet	Dry	Dry	
TSC Peaks in eV (Peak Amplitude Ratios)			
1.0 (1)			$Al-SiO_2$
1.1 (0.7)	1.1		$Al-SiO_2$
0.9 (1)	0.85 (1)		$Si-SiO_2$
1.3 (0.75)	1.35 (2)		$Si-SiO_2$
		0.9 (1)	gate electrode
		1.2 (13)	gate electrode
$C_{ox}V_{FB}/Q_{TSC}$			
	1/20		$Al-SiO_2$
	1/10		$Si-SiO_2$
		1/6	gate electrode
Ion Contamination (cm^{-2})			
10^{11}	5×10^{11}	5×10^{11}	
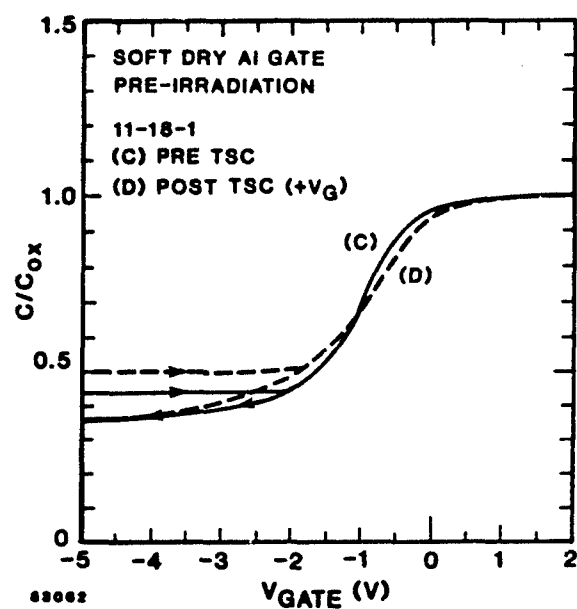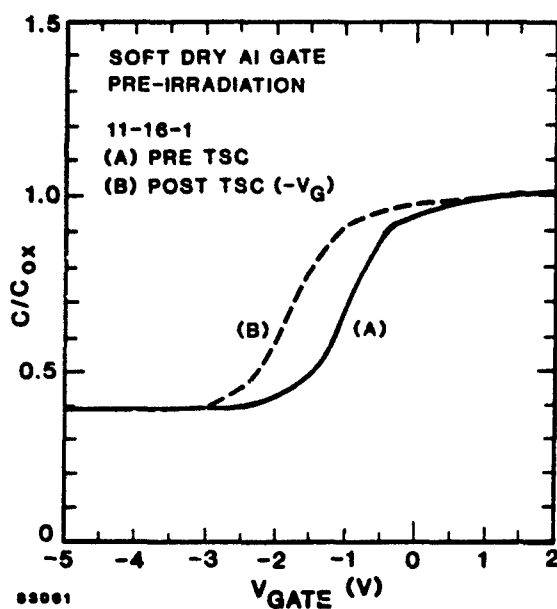
Figure 10. C-V measurements associated with the bias-temperature (BT) instability for both positive and negative bias used during TSC measurements.

flatband shift occurs (curve C to D). Note that these shifts are opposite to those expected for mobile ions. Another feature characteristic of the negative BT instability reported in the literature[22] is the introduction of interface states. Observe that the C-V stretchout in Figure 10 for the positive BT case is consistent with this effect, although lateral nonuniformities cannot be ruled out.

Representative TSC spectra observed for negative and positive BT instabilities are shown in Figure 11. These spectra were obtained from the first TSC measurements made on the five samples. Note that an approximate peak activation energy of 1 eV holds for all samples (soft and hard) and for both bias polarities. (On a few samples a second peak at ~1.2 eV was noted.) The magnitude of these peaks was not observed to correlate with either bias polarity or radiation hardness, although more data would be required to substantiate this point.
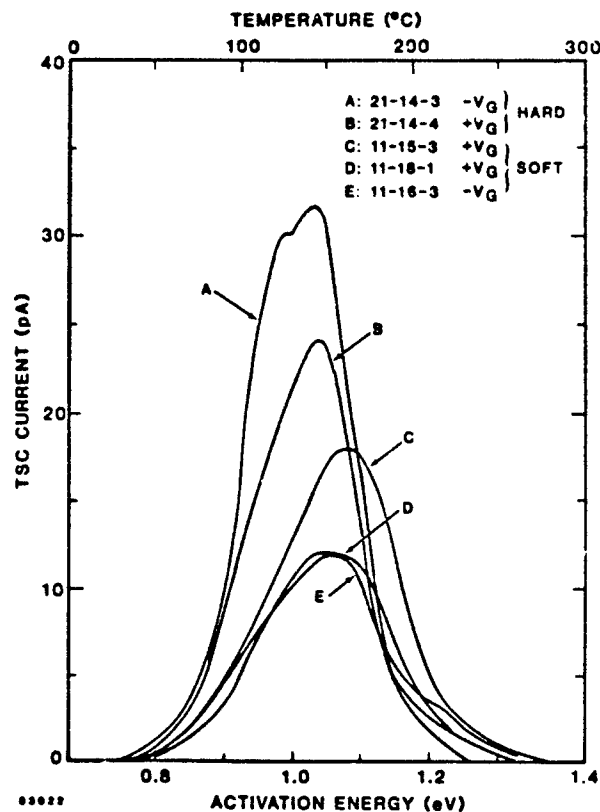
Figure 11. TSC spectra associated with negative and positive BT instabilities. Bias used during TSC measurements was 1.0 MV/cm with the polarity indicated.

The literature contains a large number of references to the negative BT instability.[23] Few references to the positive BT instability exist, except in the early literature[24] and in recent work dealing with poly Si MOS devices.[25] This is understandable based on the very small flatband shift which is barely observable in C-V measurements. However, the amount of released charge involved in both instabilities is of approximately the same magnitude, as determined by TSC measurements.

The measured flatband shift (ΔV_{FB}) and integrated TSC current (Q_{TSC}) for positive ($+V_G$) and negative gate ($-V_G$) can be written as

$$C_{ox} \Delta V_{FB} = -(Q_+ d_+ - Q_- d_-)/t \tag{7}$$

$$Q_{TSC}(+V_G) = -C_{ox} \Delta V_{FB} + Q_- \tag{8}$$

$$Q_{TSC}(-V_G) = -C_{ox} \Delta V_{FB} - Q_+ \tag{9}$$

where Q_+ and d_+ are the magnitude and distance from the gate electrode of the residual positive charge, Q_- and d_- are the magnitude and distance for the residual negative charge, and t is the oxide thickness. If it is assumed that only charge of one sign is released for each bias, these equations can be solved for the residual charge and its location. For both biases, the location of the centroid was found to be within 50 Å of the gate electrode, with the sign of the residual charge for positive gate bias being negative, while for negative bias charge of the opposite sign occurred. The activation energies for both charge polarities were the same. However, there is no experimental justification for assuming that only one carrier is involved for each bias. Therefore, insufficient information is available to determine unambiguously residual charge magnitudes and locations. We observed a change of sign of the flatband shift with change of sign of gate bias, which indicates that the distribution of residual charge is dependent on the polarity of the applied bias. However, the activation energies are the same for both carriers and both bias polarities. These observations are independent of which analysis is invoked. No explanation for this behavior is offered at present.

2.5.2 Irradiation Effects

2.5.2.1 Intrinsic Effects.

The effects of irradiation and subsequent TSC measurements on MOS capacitors are shown in the C-V plots of Figures 12 and 13. Even though these curves are for samples from lot 2, the same effects occur for those from lot 1. It is observed that the negative flatband shift which occurs upon irradiation is almost completely eliminated by a subsequent TSC measurement. This shows that the current observed during the TSC measurement corresponds to the trapped hole charge introduced by Co^{60} irradiation. Also seen is stretch-out in the C-V curves for irradiated devices which is consistent with the generation of interface states.

Representative TSC spectra observed for lot 2 samples are shown in Figure 14. The same spectrum is observed independent of any initial pre-irradiation TSC measurements. The same peak also occurred in all lot 1 samples along with the ~ 0.85 eV peak described previously. The ~ 0.85 eV peak is discussed in detail below in the section dealing with Na-induced radiation effects. In Figure 14, the variation in TSC spectra between nominally the same type of sample (dry, soft, Al gate, lot 2) irradiated to the same dose is shown. Figure 15 shows the degree of reproducibility for repeated irradiations and TSC measurements on the same sample. After a number of TSC measurement cycles (depending on sample, dose, and maximum TSC current) the sample will finally fail. Until this occurs, Figure 15 shows that the data are generally reproducible.

Initially the very broad peak, centered at ~ 1.3 eV with FWHM of over 0.2 eV, was believed to be a single distribution. Note, however, that in curve C of Figure 15, a large shoulder exists near 1.4 eV. For other samples from both lots, structure was evident within this broad manifold with apparent overlapping distributions (see Figures 16 and 17). The nature of this structure will require further investigation. This ~ 1.3 eV peak occurs in all irradiated MOS capacitors so it is identified as being associated with "intrinsic" hole trap distribution in thermally grown SiO_2.

2.5.2.2 Na-Induced Radiation Effects.

In Figure 17, a representative TSC spectrum for a sample from lot 1 is shown. In addition to the ~ 1.3 eV peak, a small peak is evident at ~ 0.85 eV. This is the same peak that was clearly

DRY SOFT Aℓ GATE 11-16-1
(A) PREIRRADIATION
(B) POST-IRRADIATION 0.24 Mrad(Si)
(C) POST TSC (-V_G)
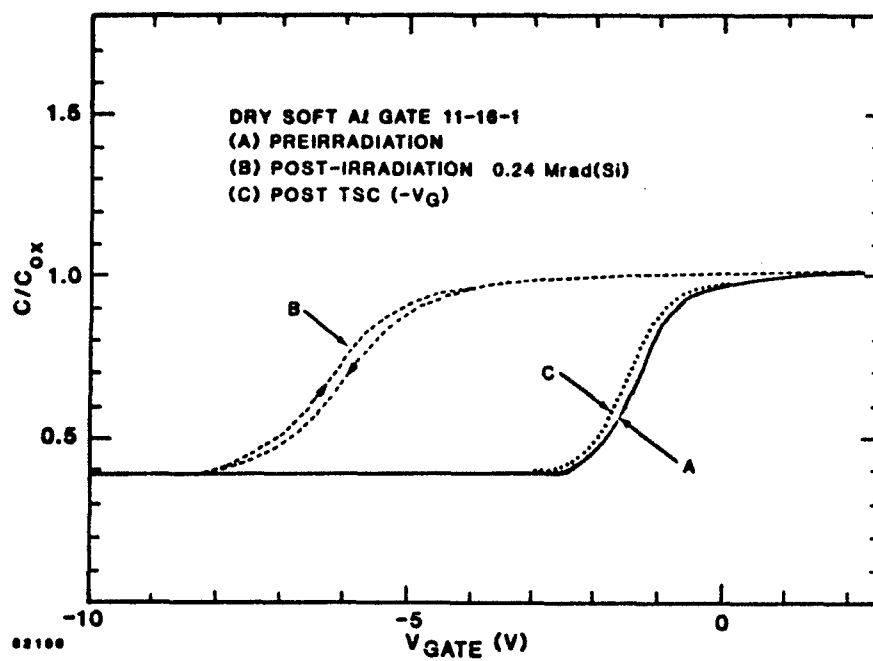
Figure 12. C-V measurements for an irradiated soft MOS capacitor.

DRY HARD Aℓ GATE 21-14-2
(A) PREIRRADIATION & POST-IRRADIATION
    POST TSC (-V_G)
(B) POST-IRRADIATION 1.27 Mrad(Si)
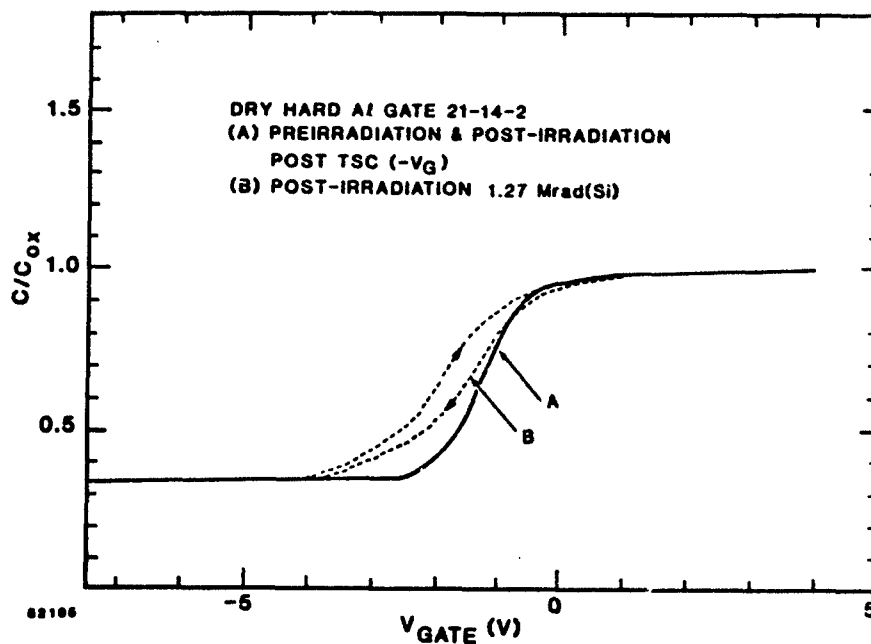
Figure 13. C-V measurements for an irradiated hard MOS capacitor.

29

Figure 15. TSC spectrum of an MOS capacitor for repeated irradiations.

TSC (-V_G)
DRY SOFT Al GATE 11-15-1
(A) 0.24 Mrad(Si) (+V_G)
(B) 0.24 Mrad(Si) (+V_G)
(C) 0.39 Mrad(Si) (+V_G)

Figure 14. TSC spectra for irradiated MOS capacitors without Na contamination.

TSC (-V_G)
DRY SOFT Al GATE
0.24 Mrad(Si) (+V_G)
Na FREE
(A) 11-15-1
(B) 11-16-1
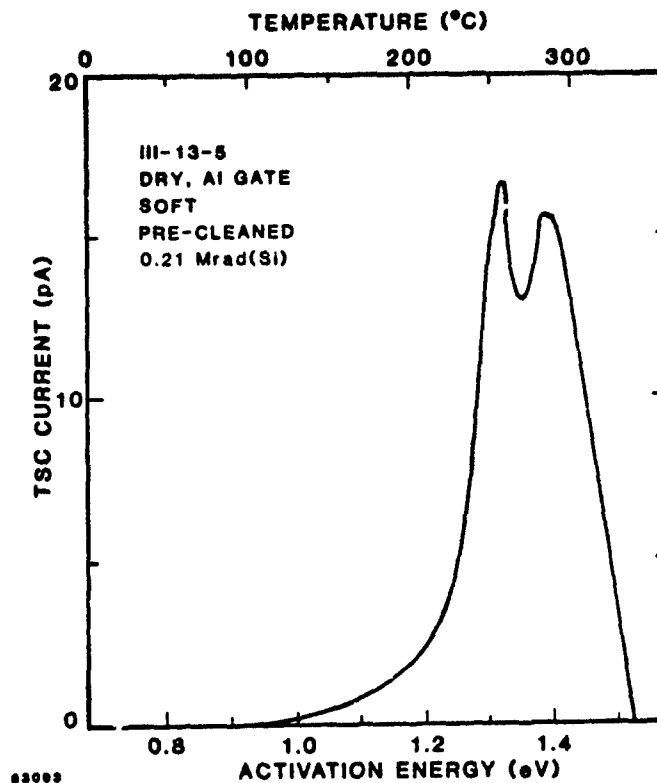
Figure 16. TSC spectrum of an irradiated MOS capacitor with structure in the intrinsic peak.
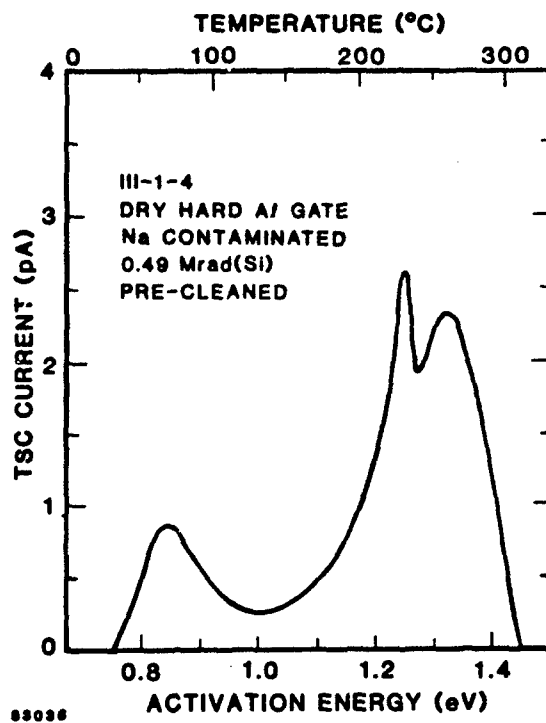
Figure 17. TSC spectra for an irradiated MOS capacitor with Na contamination after "pre-cleaning". See text for details.

31

evident in Figure 6 in the early TSC measurements of lot 1 samples. Figure 17 is labeled "pre-cleaned" which indicates that a series of pre-irradiation TSC measurements were made which moved the mobile ions to the Si-SiO$_2$ interface and back to the Al gate before irradiation. If this "pre-cleaning" step is not performed, the ~0.85 eV peak does not occur. For <u>dry</u> oxides, the large ~1.3 eV peak can mask the smaller peak at ~0.85 eV (Figure 16).

A direct comparison of the non-precleaned versus precleaned spectra is shown in Figure 18. Observe that the ~0.85 eV peak in the precleaned spectrum is larger than the intrinsic peak located at 1.3 eV for these hard lot 1 samples. Of considerable interest is the question of whether repeated movement of Na ions to the Si-SiO$_2$ interface would additively produce more traps, thereby causing an initially hard oxide to become softer with temperature and bias changes. This possibility has not yet been addressed experimentally.
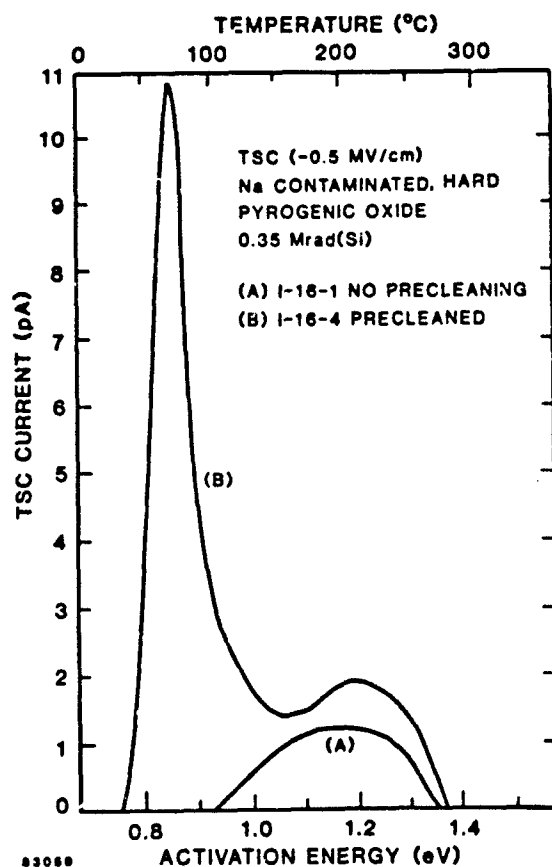
Figure 18. TSC spectra comparing "pre-cleaning" to no "pre-cleaning" for irradiated pyrogenic MOS capacitors.

32

One possible explanation for this effect is that moving Na ions to the Si-SiO$_2$ interface leaves a "footprint" by introducing a new trap site distinct from traps associated with the ~1.3 eV peak. Another possibility is that of radiation-induced ion mobility.[26] Even though there is no appreciable drift of ions under the bias used in these experiments at room temperature, radiation may induce an increased mobility. This would occur only after bias-temperature stressing is performed since samples without any TSC measurement do not show the ~0.85 eV peak. A test of this possibility would be to first perform a negative-bias TSC measurement on a lot 1 sample for which no ion peaks are observed. If, after irradiation, the TSC spectrum contains no ~0.85 eV peak, the possibility of radiation-induced mobility can be discounted. Such experiments are planned.

2.6 CONCLUSIONS

In summary, we have observed pre-irradiation bias-temperature instabilities, both for negative and positive bias. The same activation energy (~1 eV) was noted for both positive and negative charge carriers. For "hole traps" in irradiated devices, the same activation energies (~0.85 and ~1.3 eV) were noted in both soft and hard oxides. Hard oxides simply have less traps than their soft counterparts. There appears to be an "intrinsic" hole trap at ~1.3 eV, possibly consisting of charged traps with a number of different activation energies. If the oxide has Na$^+$ contamination and those ions are moved to the Si-SiO$_2$ interface, there is an additional "hole trap" at ~0.85 eV.

SECTION 3

SOFT ERROR STUDIES IN GaAs DEVICES

3.1 INTRODUCTION

The inherent radiation tolerance of GaAs devices makes them candidates for utilization in future systems required to operate in a radiation environment. Hence, there is an increasing interest in the susceptibility of GaAs integrated circuits to soft errors. A soft error is a transient upset of a device caused by a single ionizing particle. These upsets are produced by incident radiation such as alpha particles emitted from trace elements in packaging materials and cosmic rays. The upset mechanism is the collection of ionization-induced charge at sensitive nodes (typically a reverse-biased pn junction) by drift and diffusion. In general, the drift component consists of charge generated in the depletion region and charge that is collected from beyond that region by charge funneling.[27,28] The diffusion component is simply that charge which diffuses to the edge of the depletion region and is then swept to the sensitive node.

In order to develop effective hardening techniques for soft errors, it is important to determine the relative roles of drift and diffusion as charge collection mechanisms and, in particular, to determine whether funneling is present. One way to accomplish this task is to perform time-resolved charge collection measurements. Such measurements have been performed for silicon.[29] In this section, preliminary charge collection measurements on GaAs devices bombarded with single alpha particles are reported. These initial results indicate that charge funneling does occur in GaAs.

3.2 EXPERIMENTAL PROCEDURE

The devices used in this study were Au – n-type GaAs Schottky-barrier diodes fabricated at NRTC. A schematic representation of the devices is shown in Figure 19. Au dots with a diameter of 10 mils were evaporated onto a S-doped epitaxial layer. The epi layer was ~7-μm thick with a net doping density of ~1 x 10^{15} cm^{-3}, and was grown on a Te-doped semiconducting substrate. An ohmic contact was made to the substrate with silver paste which also served to attach a given device to a TO-5 header. A reverse bias was applied and charge collection measurements following a single alpha event were then made.
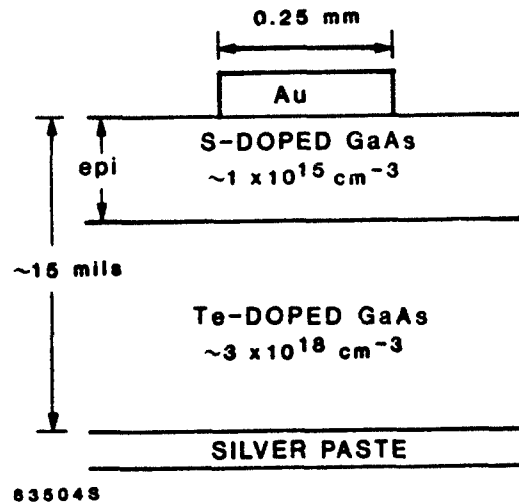
Figure 19. Schematic representation of the device
structure used in charge collection
measurements.

A schematic of the experimental configuration used in charge collection
measurements is shown in Figure 20. A Cm^{244} thin foil which emits primarily
5.8-MeV alpha particles was used as the source. An aperture was fitted over
the foil and the source then placed ~9 mm from the device under test so that
normal incidence was achieved. (The air gap and Au degrade the alpha energy
to ~5.0 MeV before entering the GaAs.) The alpha-induced charge was measured
by a Tektronix P6201 FET probe. The probe has a 1-GHz bandwidth, unity gain,
and a nominal input capacitance of 3 pF in parallel with a 100 kΩ resistance.
The system mainframe is a Tektronix 7912AD transient digitizer. The digitizer
has a bandwidth of 500 MHz and is capable of measuring sub-nanosecond rise-
times. The two plug-ins used in the mainframe were the Tektronix 7A29 ampli-
fier and the 7B90P timebase. The 7A29 is a 1-GHz bandwidth amplifier with a
maximum sensitivity of 10 mV/div. The 7B90P timebase is calibrated to a sweep
speed of 500 ps/div. The resulting system risetime was found to be ~1 ns
(10% to 90%).

3.3 RESULTS AND ANALYSIS

A typical data trace is shown in Figure 21 which reveals the prompt and
delayed components of the collected charge. Figure 22 shows preliminary results
of the charge collection experiment. Both the prompt and total collected charge
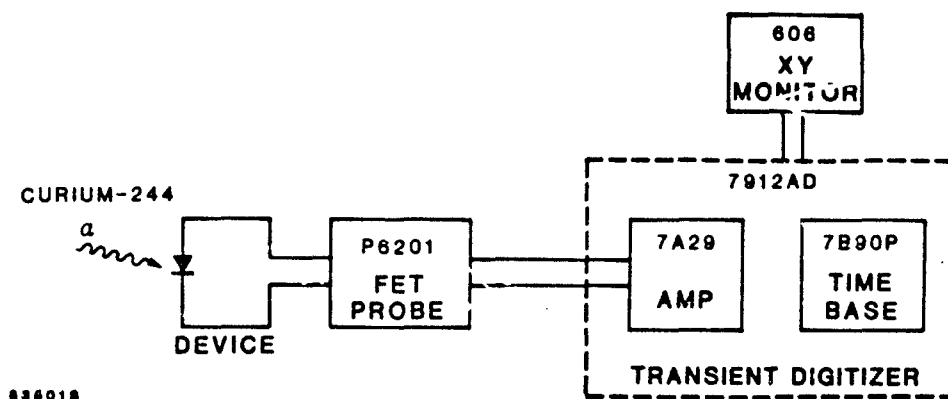
Figure 20. Experimental configuration used in charge collection measurements.
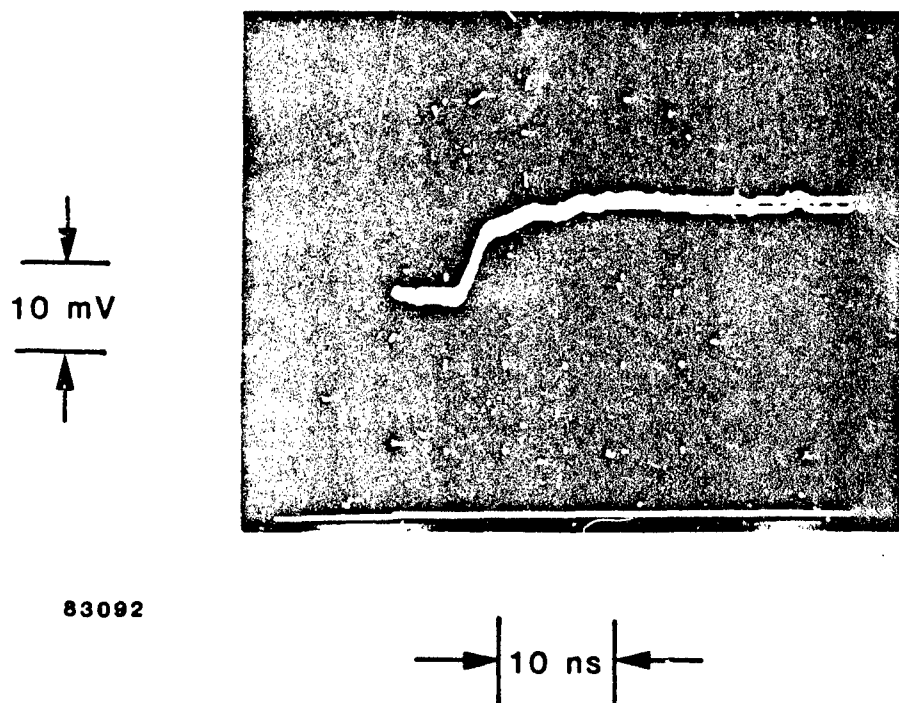
Figure 21. Example of charge-collection data trace showing the prompt and delayed components of collected charge.
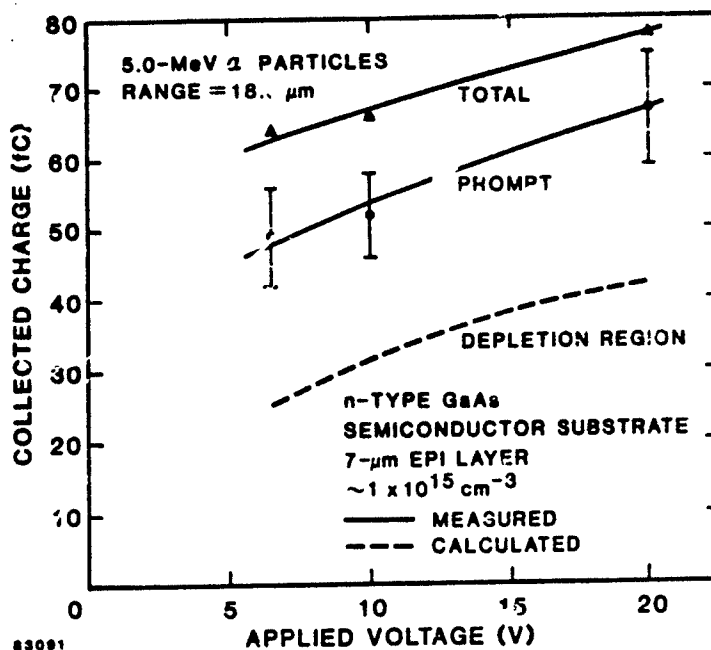
Figure 22. Collected charge vs. applied voltage
for 5.0-MeV alpha particles incident
on Au—n-type Schottky-barrier diode.

are displayed as a function of applied bias. Fifteen measurements were made
at each bias and then averaged. The error bars shown for the prompt component
include one standard deviation from the mean as well as the experimental uncer-
tainty in the integrating capacitance. The contribution to the prompt compo-
nent by charge created in the initial (i.e., equilibrium) depletion region is
also shown. This contribution was calculated from a Bragg curve developed for
GaAs. The calculation assumes that prompt recombination is negligible.

Qualitatively, the difference between the depletion region component and
the measured prompt charge strongly suggests that charge funneling is occurring.
However, before quantifying the magnitude of the funnel effect, a number of
issues must be addressed. One such issue is prompt recombination. At early
times, the charge density along the track is very high. Hence radiative or
Auger recombination may play a role in reducing the amount of charge available
for collection. Prompt recombination would cause an underestimation of the
funnel length. Second, the amount of diffusion charge which would be collected

37

during the system risetime needs to be estimated. Depending on the length of the funnel as well as its collection efficiency, some charge may diffuse to the edge of the depletion region during the system risetime. This charge would be counted as being collected by drift causing an overestimation of the funnel length.

Further work is clearly needed and will be performed under Contract DNA 001-83-C-0108. Nevertheless, the preliminary data indicate that funneling does occur in GaAs devices.[*]

---

[*]For an updated treatment of charge collection in GaAs devices, the reader is referred to a paper by M.A. Hopkins and J.R. Srour in the December 1983 issue of the IEEE Transactions on Nuclear Science.

INVESTIGATION OF NEUTRON-INDUCED EFFECTS IN VLSI STRUCTURES

4.1 INTRODUCTION

Transient upsets due to the ionization produced in a circuit by a single incident particle are of considerable interest at present. Single particles also create permanent damage due to displacement of lattice atoms. If that damage occurs in a sensitive region of a VLSI circuit, the issue arises whether the resulting changes in electrical properties are significant enough to be a problem. We have explored this issue experimentally and analytically for the case of 14-MeV neutrons incident on silicon devices. In Section 4.2, findings for small-geometry bipolar transistors and pinch resistors are described. Section 4.3 summarizes results of an experiment designed to observe single neutron induced damage regions. Experiments on MOS/VLSI transistors are presented in Section 4.4. A summary of this investigation is given in Section 4.5.

4.2 STUDIES ON BIPOLAR TRANSISTORS AND PINCH RESISTORS

4.2.1 Introductory Remarks

Descriptions of our earlier studies of neutron effects on small-geometry bipolar transistors and pinch resistors have been presented previously.[30,31] That work was extended and the experimental and analytical results obtained are described herein. The experimental methods employed are described in Section 4.2.2. Experimental findings for pinch resistors are presented in Section 4.2.3. In Section 4.2.4 analytical and modeling efforts performed to account for the pinch resistor data are described. Results for bipolar transistors are given in Section 4.2.5.

4.2.2 Experimental Methods

Test chips containing both bipolar transistors and pinch resistors were fabricated at Northrop Research and Technology Center. A population of 100 pinch resistors with approximate dimensions of 2.3 x 3.1 x 0.25 μm (Figure 23) was employed to obtain basic insight regarding neutron interactions in silicon devices. The doping concentration in the active region of these resistors was $\sim 5 \times 10^{16}$ cm^{-3}. Ninety of these devices were irradiated with 14-MeV neutrons

TOP VIEW

80-505S
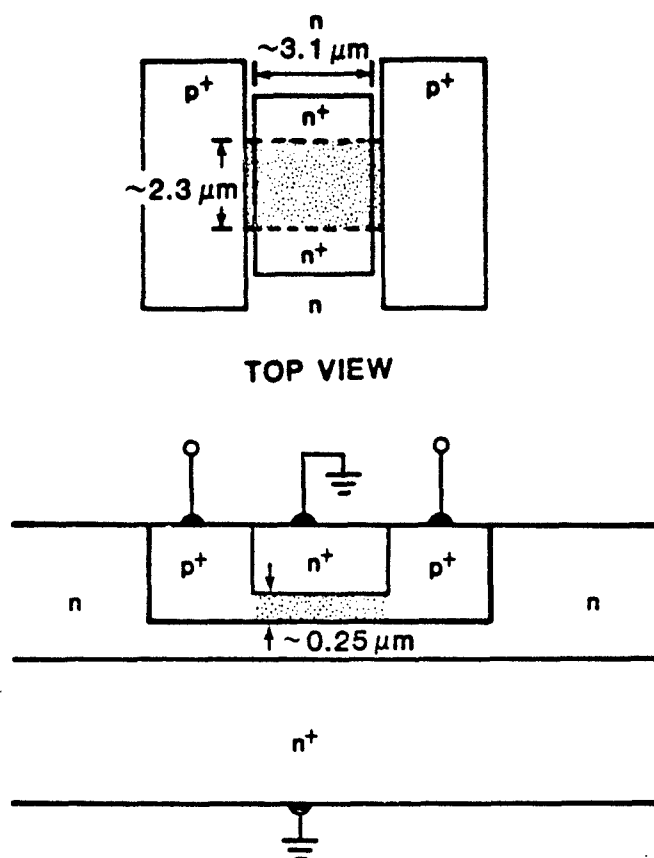
Figure 23. Schematic illustration of pinch resistors.

at the Lawrence Livermore Laboratory RTNS-II source in eleven increments.
Cumulative fluences ranged from 5.3 x 10^{10} to 2.9 x 10^{12} n/cm^2, as listed in
Table 2. The remaining ten devices were employed as unirradiated controls.
Very accurate measurements of resistance were performed pre- and post-irradi-
ation by averaging multiple data runs, as described below. A typical standard
deviation, expressed as a percentage of the mean value, was 0.01%.

Bipolar transistors used in this study had the configuration shown in
Figure 24. The intrinsic basewidth was ~0.25 μm (doping concentration
~5 x 10^{16} cm^{-3}) and the collector dimension ℓ_c was ~2.3 μm for 83 devices
and ~3.1 μm for 38 devices. For these populations, six of the 2.3-μm tran-
sistors and two of the 3.1-μm transistors were maintained as unirradiated
controls. Thus, 77 2.3-μm and 36 3.1-μm devices were irradiated. Irradia-
tions performed were the same as those for pinch resistors (Table 2) since
the same chips were employed.

40

Table 2. 14-MeV neutron fluences used in irradiations of bipolar transistors and pinch resistors.

Irradiation Number	Incremental Fluence	Cumulative Fluence
1	5.3×10^{10} n/cm^2	5.3×10^{10} n/cm^2
2	5.3×10^{10}	1.1×10^{11}
3	1.2×10^{11}	2.3×10^{11}
4	1.1×10^{11}	3.3×10^{11}
5	1.1×10^{11}	4.4×10^{11}
6	2.1×10^{11}	6.5×10^{11}
7	2.1×10^{11}	8.6×10^{11}
8	5.3×10^{11}	1.4×10^{12}
9	5.2×10^{11}	1.9×10^{12}
10	5.2×10^{11}	2.4×10^{12}
11	5.2×10^{11}	2.9×10^{12}

TOP VIEW
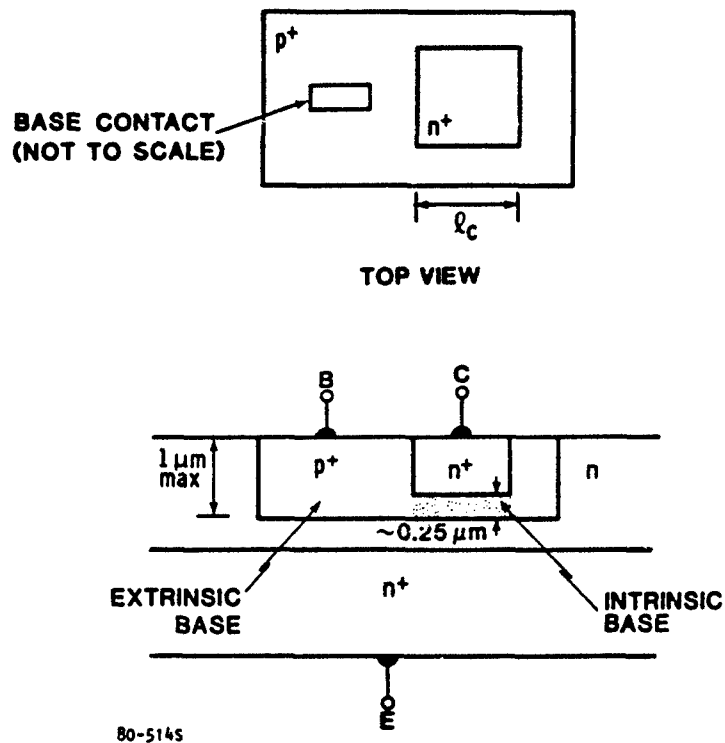
Figure 24. Schematic illustration of bipolar transistors.

Twenty test chips were studied. Each chip contained five pinch resistors and, depending on yield, up to eleven transistors. The transistors and resistors were sequentially switched into test circuits under computer control. The measurement system and its capabilities are now described.

Figure 25 shows a simplified version of the test circuit used to measure transistor collector current (I_c). A fixed base-emitter voltage (V_{BE}) of 720 mV was applied and monitored for each I_c measurement. Each I_c value was adjusted for variations in V_{BE}, and if V_{BE} varied more than 500 μV the test was aborted. A fixed collector-emitter voltage of 1.000 volt was applied and monitored. If it varied more than 500 μV the test was also aborted. The collector current was converted to a voltage by a Keithley Model 616 Electrometer and monitored by a Hewlett-Packard Model 3456A Digital Voltmeter (DVM). The DVM was programmed, under computer control, to make a series of ten readings of the voltage on the 616. Each of the ten readings was averaged over one hundred power line cycles to reduce any common-mode voltages. The ten readings were then averaged and this average value, along with its standard deviation, was stored in the computer. (The percent standard deviation was typically less than 0.02%, with a maximum of 0.1%.) Finally, temperature was monitored for each I_c measurement and the I_c value adjusted accordingly. If the temperature varied more than 0.1°C from 30°C the test was aborted.

An h_{FE} measurement was also made for a subset of the transistor population using a separate test fixture. Base current was varied until a desired collector current was obtained and the resultant h_{FE} was computed.

Figure 26 shows a simplified version of the test circuit used to measure the resistance of pinch resistors. The Hewlett-Packard Model 3456A DVM was used in its resistance-measurement mode with an excitation current of 500 nA. This low current was used to minimize the voltage drop across the pinch resistors (typically 10 to 30 millivolts). Sets of 10 readings were made in the same manner as for the transistor collector currents. Temperature was also monitored and corrected for in a similar manner. Figure 27 shows a detailed wiring diagram for the circuit used in testing both the transistors and the pinch resistors. A simplified version of the computer test flow diagram is shown in Figure 28.
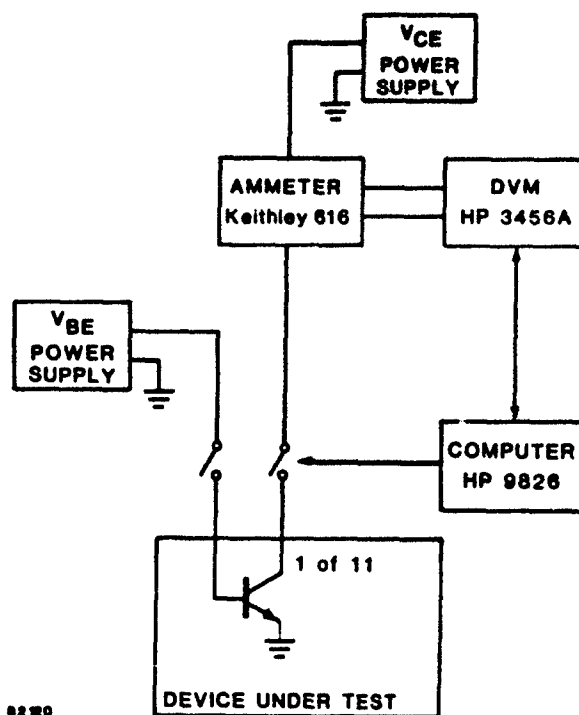
Figure 25. Simplified diagram of test set-up used to measure transistor collector current.
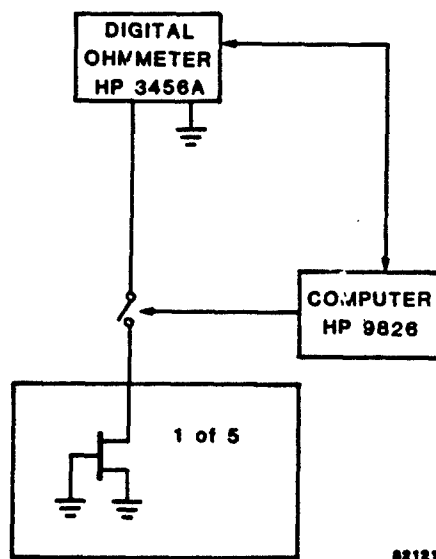
Figure 26. Simplified diagram of test set-up used to measure the resistance of pinch resistors.
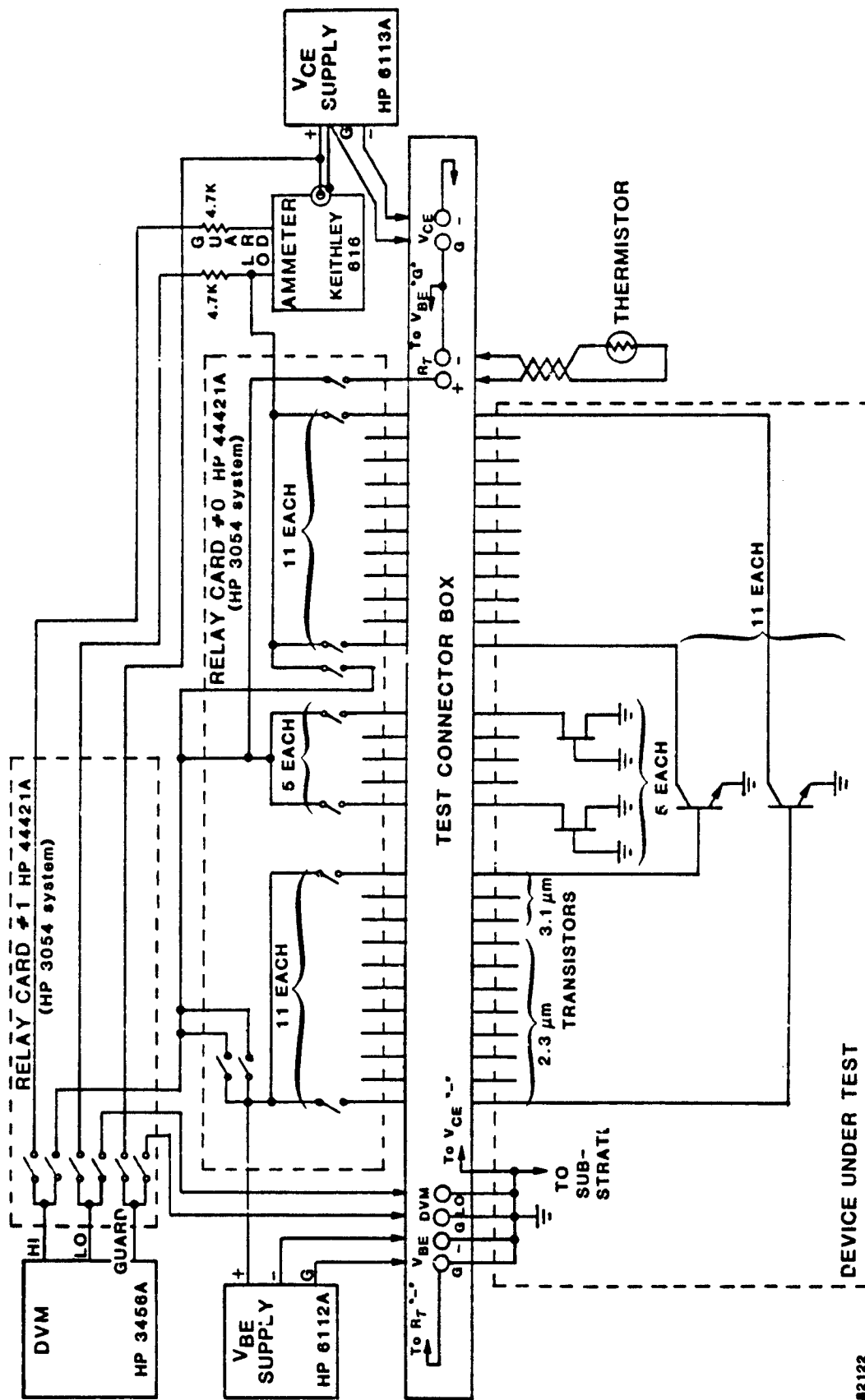
Figure 27. Wiring diagram for the circuit used in testing transistors and pinch resistors.
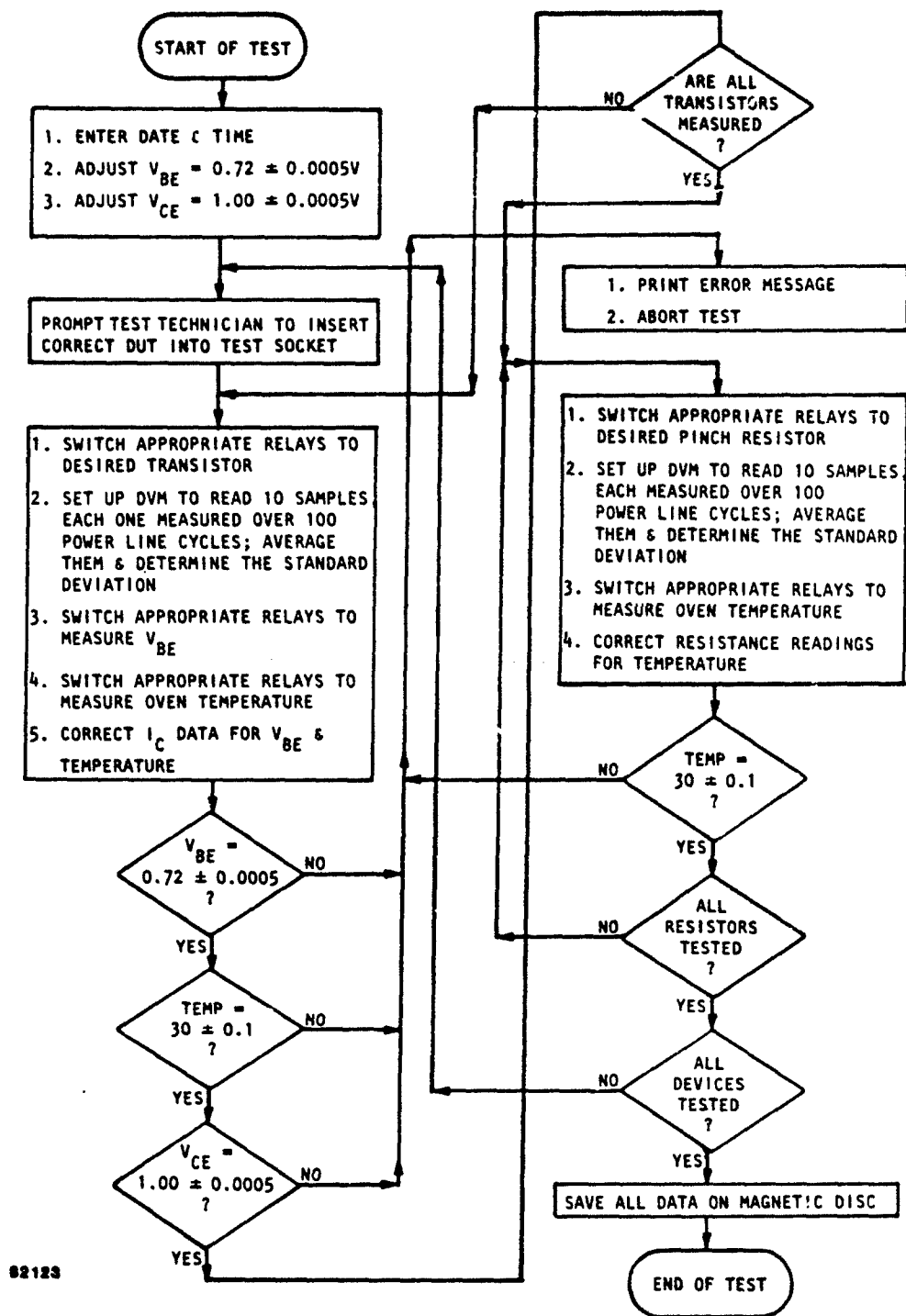
Figure 28. Simplified computer test flow diagram employed in transistor and pinch resistor measurements.

4.2.3 Pinch Resistor Results

Figure 29 is a histogram showing percent change in resistance for the pinch resistor population after the first irradiation. One device stands out from the population at 0.4%. We interpret this as being due to the creation of a single, relatively large damaged region by a neutron interaction in that resistor. Figure 30 shows discrete changes in resistance that occurred for five devices at various fluences. The relatively large change that occurred for device number 22/13 (solid line) near 2×10^{12} n/cm^2 may have been due to multiple neutron interactions. Figure 31 shows a histogram for the pinch resistor population after 1.4×10^{12} n/cm^2. A similar histogram after 2.9×10^{12} n/cm^2 is shown in Figure 32. Most of the resistance changes are relatively small, which is consistent with the analysis described below. Also, if the population had been considerably larger (e.g., 1000 devices instead of 90), a broad, continuous distribution of resistance changes would have been observed. Table 3 gives the complete history of all 100 pinch resistors (including the ten controls). Shown is percent change in resistance measured for all devices after each of the eleven irradiations. This comprehensive set of pinch resistor data provides insight regarding the statistics of 14-MeV neutron interactions in silicon. Analytical and modeling efforts related to these data are now described.

4.2.4 Analysis and Modeling of Pinch Resistor Data

Analysis and modeling were performed for the case of 14-MeV neutrons incident on silicon for the purpose of obtaining basic information regarding neutron interactions and the nature of damaged regions. Calculations were made to determine the energy and angular distributions of primary knock-on atoms (PKAs) for elastic and inelastic scattering. A distributed cluster model was then developed in an attempt to account for the resistor data. Results of these efforts are now described.

4.2.4.1 Determination of PKA Distributions. To predict the effects of single neutron-induced damage regions on semiconductor devices, it is necessary to determine the energy and angular distributions of PKAs. These distributions can be calculated from cross sections given in the literature.[32-34] Both elastic and inelastic interactions have approximately the same probability of occurring for 14-MeV neutrons in Si but each has very different differential angular cross sections which need to be taken into account in determining PKA distributions.
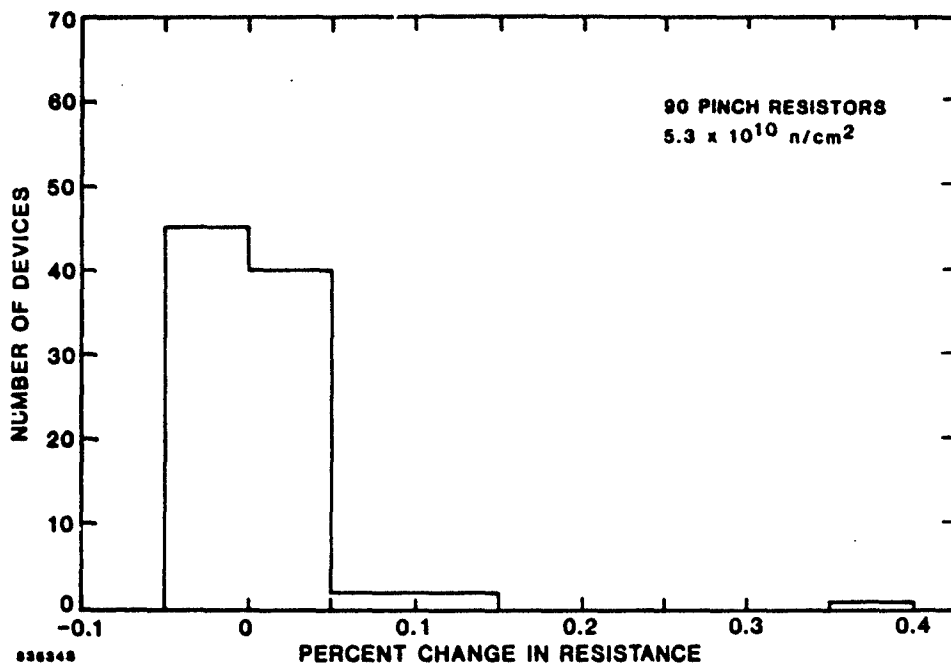
Figure 29. Histogram showing percent change in resistance for the irradiated pinch resistor population after 5.3×10^{10} n/cm^2.
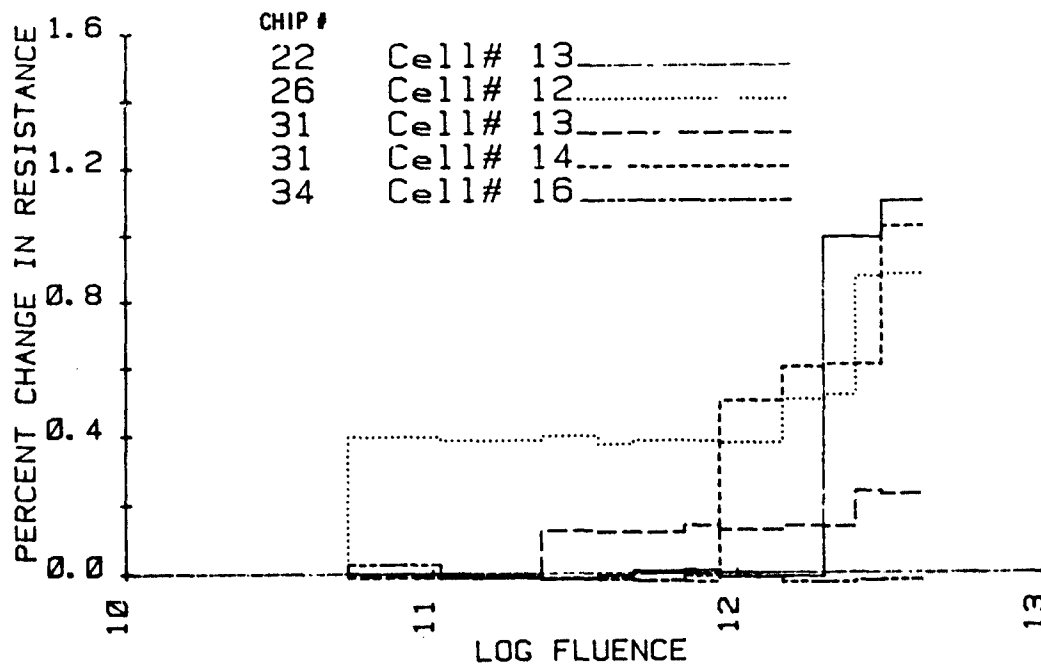
Figure 30. Percent change in resistance vs. fluence for five pinch resistors.

47
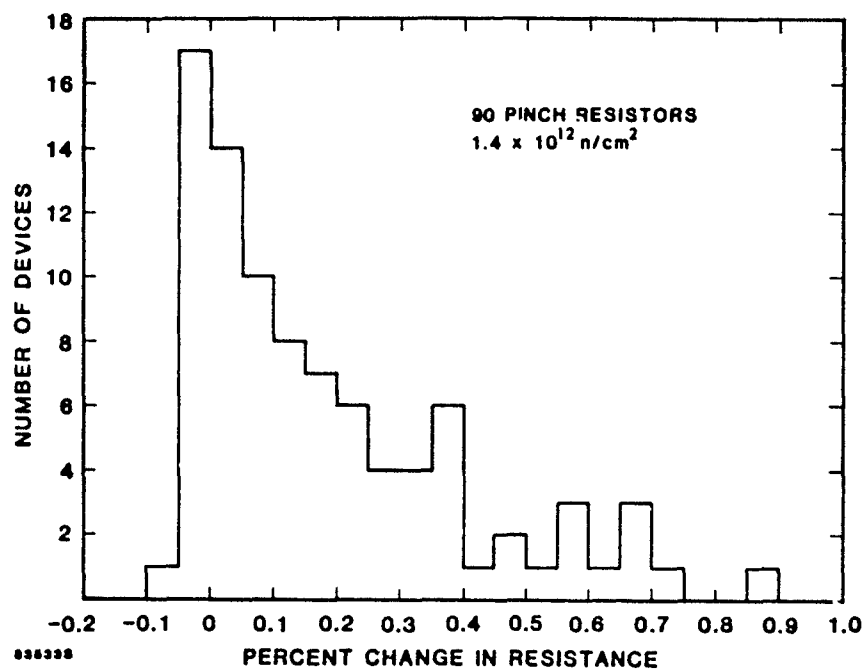
Figure 31. Histogram showing percent change in resistance for the irradiated pinch resistor population after 1.4×10^{10} n/cm^2.
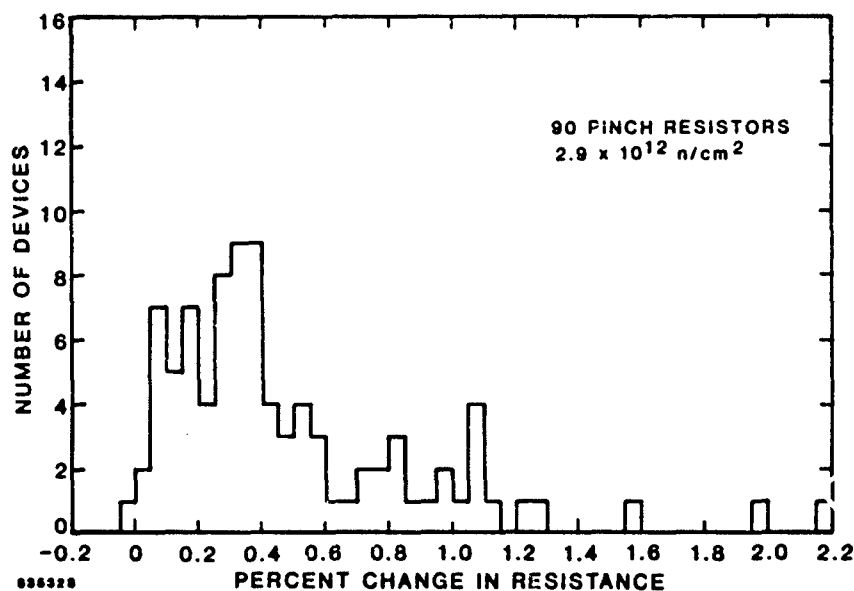
Figure 32. Histogram showing percent change in resistance for the irradiated pinch resistor population after 2.9×10^{12} n/cm^2.

48

Table 3. Percent change in resistance measured for a population of pinch resistors after each of eleven 14-MeV neutron irradiations. (Neutron fluences are given in Table 2.) The first ten devices listed are unirradiated controls.

DEVICE NUMBER	IRRADIATION NUMBER										
	1	2	3	4	5	6	7	8	9	10	11
21/12	-0.02	-0.02	-0.04	-0.03	-0.02	-0.04	-0.05	-0.04	-0.02	-0.05	-0.04
21/13	-0.02	-0.01	-0.02	-0.03	-0.02	-0.02	-0.03	-0.03	-0.02	-0.04	-0.03
21/14	-0.02	-0.01	-0.02	-0.03	-0.02	-0.01	-0.02	-0.03	-0.01	-0.04	-0.03
21/15	-0.03	-0.04	-0.04	-0.05	-0.03	-0.04	-0.05	-0.06	-0.04	-0.07	-0.06
21/16	-0.05	-0.05	-0.07	-0.06	-0.05	-0.04	-0.08	-0.08	-0.07	-0.07	-0.06
32/12	0.01	-0.00	0.01	-0.01	-0.01	-0.01	-0.02	-0.01	-0.01	-0.01	-0.02
32/13	0.01	0.00	0.01	-0.00	-0.01	-0.00	-0.02	-0.02	-0.02	-0.03	-0.02
32/14	0.01	-0.00	0.01	-0.02	-0.02	-0.01	-0.03	-0.02	-0.02	-0.02	-0.02
32/15	0.01	-0.01	0.01	-0.03	-0.04	-0.02	-0.05	-0.04	-0.04	-0.05	-0.04
32/16	0.01	-0.02	-0.01	-0.04	-0.04	-0.03	-0.05	-0.06	-0.05	-0.06	-0.06
22/12	-0.01	-0.02	-0.01	-0.02	-0.03	-0.03	-0.02	-0.04	-0.00	0.23	0.30
22/13	-0.00	-0.01	-0.02	-0.01	0.01	0.01	-0.01	-0.01	0.99	0.99	1.10
22/14	0.01	-0.01	-0.02	-0.01	-0.02	-0.02	-0.03	-0.03	0.06	0.03	0.16
22/15	-0.02	-0.02	-0.02	-0.03	-0.02	0.04	0.01	0.09	0.14	0.16	0.17
22/16	-0.03	-0.02	-0.04	-0.03	-0.03	0.01	0.03	0.04	0.50	0.53	0.54
23/12	-0.01	-0.00	-0.02	-0.02	-0.02	0.09	0.17	0.28	0.31	0.31	0.32
23/13	-0.00	-0.01	-0.02	-0.00	-0.02	-0.02	-0.02	0.10	0.14	0.12	0.12
23/14	-0.00	-0.02	-0.03	-0.01	-0.03	0.01	0.40	0.38	0.93	1.06	1.07
23/15	-0.00	0.26	0.22	0.24	0.22	0.23	0.22	0.21	0.58	0.57	0.58
23/16	-0.03	0.01	-0.04	-0.03	-0.05	-0.02	0.02	0.01	0.03	0.03	0.06
24/12	-0.00	0.01	-0.01	-0.00	-0.01	-0.01	-0.00	0.11	0.46	0.45	0.45
24/13	0.00	-0.00	-0.01	-0.00	-0.01	-0.02	-0.01	-0.01	0.01	0.01	0.02
24/14	-0.00	0.01	-0.00	-0.00	-0.00	0.01	0.04	0.34	0.44	0.41	1.07
24/15	-0.00	0.01	-0.01	-0.00	-0.02	-0.01	-0.00	0.01	0.06	0.02	0.06
24/16	-0.02	-0.01	-0.03	-0.02	-0.04	-0.01	-0.02	0.29	0.31	0.78	0.80
25/12	-0.02	0.07	0.03	0.07	0.05	0.40	0.41	0.40	0.56	0.56	0.54
25/13	-0.00	-0.01	-0.02	0.00	-0.00	-0.02	-0.00	-0.02	0.00	0.05	0.05
25/14	-0.00	0.01	0.02	0.47	0.45	0.48	0.48	0.65	0.77	1.39	2.17
25/15	-0.02	0.01	0.02	-0.01	-0.03	-0.02	-0.01	-0.02	-0.02	0.27	0.31
25/16	0.00	0.04	0.02	-0.01	-0.03	-0.02	-0.03	0.05	0.07	0.07	0.53
26/12	0.40	0.38	0.40	0.37	0.38	0.38	0.38	0.50	0.51	0.87	0.88
26/13	0.03	-0.01	0.02	-0.00	0.01	0.02	-0.02	0.21	0.36	0.40	0.70
26/14	0.04	0.01	0.06	0.05	0.05	0.06	0.02	0.04	0.02	0.25	0.27
26/15	0.02	-0.01	0.00	-0.02	-0.02	0.00	-0.02	0.06	0.04	0.12	0.13
26/16	0.02	-0.01	-0.02	-0.03	-0.02	0.00	-0.00	0.00	0.22	0.22	0.25
27/12	0.01	0.00	-0.01	-0.01	-0.01	0.01	-0.02	-0.01	0.04	0.18	0.20
27/13	0.02	0.01	-0.02	-0.01	-0.01	0.01	-0.02	0.09	0.08	0.09	0.41
27/14	0.04	0.01	-0.02	-0.03	-0.03	0.02	-0.02	0.17	0.16	0.28	0.30
27/15	0.03	0.01	-0.02	-0.03	0.04	0.16	0.12	0.12	0.12	0.25	0.36
27/16	0.02	0.01	-0.04	-0.03	-0.02	0.32	0.26	0.33	0.32	0.34	0.36
28/12	0.00	-0.01	0.02	0.01	0.02	0.01	0.01	0.01	0.02	0.18	0.19
28/13	-0.00	-0.01	-0.00	-0.01	-0.00	-0.02	0.02	0.03	0.02	0.21	0.25
28/14	-0.00	-0.02	-0.03	-0.03	0.12	0.12	0.12	0.15	0.17	0.17	0.19
28/15	-0.00	-0.02	-0.03	-0.03	0.02	0.16	0.18	0.16	0.19	0.16	0.18
28/16	-0.00	-0.02	-0.03	-0.01	0.11	0.12	0.16	0.40	0.41	0.41	0.41
29/12	-0.02	0.07	0.10	0.08	0.08	0.11	0.11	0.26	0.25	0.37	0.35
29/13	-0.00	-0.04	0.05	0.46	0.46	0.47	0.47	0.45	0.96	0.96	1.25
29/14	0.00	-0.02	-0.03	-0.03	-0.03	0.38	0.41	0.59	0.61	0.80	0.82
29/15	0.00	-0.04	-0.03	-0.03	-0.03	-0.02	0.05	0.01	0.13	0.49	0.54
29/16	-0.00	-0.02	-0.03	0.04	0.14	0.15	0.22	0.17	0.65	0.64	0.72

Table 3. Percent change in resistance measured for a population of pinch resistors after each of eleven 14-MeV neutron irradiations. (Neutron fluences are given in Table 2.) The first ten devices listed are unirradiated controls. (Concluded)

DEVICE NUMBER	IRRADIATION NUMBER										
	1	2	3	4	5	6	7	8	9	10	11
30/12	0.01	0.01	0.43	0.39	0.40	0.37	0.36	0.36	0.41	—	0.44
30/13	0.03	0.01	0.02	-0.00	0.02	0.00	0.00	0.01	0.01	0.02	0.04
30/14	0.13	0.14	0.12	0.10	0.12	0.11	0.12	0.14	0.14	0.15	0.27
30/15	0.01	-0.01	0.00	-0.02	-0.01	-0.02	-0.02	0.01	0.22	0.21	0.31
30/16	0.02	0.00	-0.01	-0.02	-0.02	-0.01	0.33	0.32	0.32	1.25	1.56
31/12	-0.01	-0.01	-0.01	-0.01	-0.02	-0.02	-0.04	-0.03	-0.03	0.07	0.35
31/13	-0.01	-0.01	0.12	0.12	0.12	0.14	0.12	0.13	0.13	0.23	0.23
31/14	-0.01	-0.01	-0.01	-0.02	-0.02	-0.02	0.50	0.60	0.61	0.61	1.02
31/15	0.01	0.02	0.00	-0.01	-0.01	0.33	0.33	0.90	1.97	1.95	1.99
31/16	0.01	-0.00	0.00	0.02	-0.00	0.11	0.11	0.11	0.20	0.21	0.35
33/12	0.11	0.10	0.18	0.18	0.28	0.42	0.54	0.64	0.89	1.04	1.12
33/13	0.01	-0.01	0.00	0.00	-0.00	0.01	0.00	0.39	0.37	0.38	0.38
33/14	-0.01	-0.01	-0.00	-0.02	-0.03	-0.00	-0.02	0.16	0.16	0.27	0.31
33/15	0.03	0.04	0.03	0.02	0.02	0.04	0.03	0.01	0.49	0.49	0.60
33/16	-0.01	-0.02	0.17	0.16	0.16	0.22	0.15	0.17	0.15	0.16	0.18
34/12	0.03	0.01	0.08	0.08	0.07	0.08	0.12	0.17	0.25	0.25	0.28
34/13	0.06	-0.00	0.00	0.01	0.00	0.01	0.01	-0.00	0.02	0.25	0.36
34/14	-0.01	-0.01	-0.01	-0.02	-0.02	-0.01	-0.01	-0.02	0.22	0.20	0.20
34/15	0.03	-0.01	-0.02	-0.02	0.00	0.03	0.01	0.07	0.10	0.73	0.99
34/16	0.03	-0.01	-0.02	-0.02	-0.02	-0.01	0.01	-0.03	-0.03	-0.02	-0.02
35/12	-0.00	0.00	0.01	-0.01	-0.01	-0.00	0.00	0.30	0.32	0.47	0.49
35/13	0.02	0.02	0.03	0.03	0.02	0.45	0.44	0.47	0.47	0.48	0.47
35/14	-0.01	0.03	0.03	0.07	0.11	0.10	0.10	0.36	0.37	0.36	0.36
35/15	-0.01	-0.00	-0.02	-0.02	-0.02	-0.01	-0.03	-0.01	0.02	0.21	0.23
35/16	-0.02	-0.00	-0.02	0.00	-0.00	0.17	0.22	0.22	0.22	0.33	0.56
36/12	-0.01	-0.01	0.00	0.00	0.00	-0.01	-0.02	-0.01	-0.01	0.91	0.91
36/13	-0.01	-0.01	0.01	0.01	0.01	-0.01	-0.01	0.06	0.08	0.06	0.06
36/14	-0.02	-0.00	0.01	0.01	0.00	0.01	-0.01	0.25	0.25	0.31	0.34
36/15	0.07	0.06	0.06	0.05	0.06	0.22	0.22	0.24	0.22	0.23	0.25
36/16	0.01	0.00	0.01	-0.02	0.03	0.04	0.03	0.05	0.13	0.11	0.12
37/12	-0.00	-0.05	0.01	0.03	-0.02	0.24	0.65	0.59	0.60	0.74	1.26
37/13	0.03	-0.04	0.00	0.03	-0.07	0.10	0.06	0.15	0.22	0.22	0.58
37/14	-0.01	-0.08	0.00	0.03	-0.10	0.06	-0.01	-0.01	0.13	0.09	0.09
37/15	-0.02	-0.09	-0.04	-0.01	-0.16	-0.05	-0.10	0.19	0.24	0.20	0.36
37/16	0.04	-0.03	0.15	0.16	0.00	0.13	0.07	0.04	0.30	0.30	0.49
38/12	-0.02	0.06	0.09	0.01	0.06	0.59	0.57	0.73	0.92	0.96	1.07
38/13	-0.02	0.22	0.22	0.15	0.20	0.21	0.13	0.21	0.13	0.19	0.16
38/14	-0.02	0.08	0.08	0.04	0.08	0.29	0.19	0.26	0.79	0.87	0.85
38/15	-0.03	0.07	0.07	0.03	0.08	0.06	-0.03	0.09	0.00	0.10	0.07
38/16	-0.05	0.05	0.06	0.01	0.06	0.02	0.01	0.07	0.36	0.39	0.34
39/12	0.01	0.01	0.01	0.02	0.01	0.02	-0.01	-0.00	0.02	0.01	0.12
39/13	0.02	0.01	0.02	0.03	0.02	0.03	0.00	0.02	0.03	0.06	0.80
39/14	0.02	0.01	0.01	0.03	0.02	0.03	-0.01	0.44	0.47	0.48	0.76
39/15	0.01	0.00	0.06	0.07	0.30	0.58	0.55	0.68	0.66	0.64	0.66
39/16	0.01	-0.01	-0.02	0.01	-0.01	-0.01	-0.03	0.06	0.07	0.27	0.28
40/12	0.03	-0.00	0.25	0.22	0.20	0.29	0.29	0.67	0.77	0.87	0.96
40/13	0.03	-0.01	0.02	0.06	0.03	0.08	0.09	0.01	0.09	0.04	0.12
40/14	0.05	-0.00	0.04	0.01	0.00	0.05	0.06	-0.01	0.06	-0.00	0.09
40/15	0.03	-0.01	0.02	-0.02	-0.02	0.01	0.05	-0.01	0.07	0.02	0.37
40/16	0.03	-0.03	0.02	-0.02	-0.04	0.01	0.01	-0.05	0.36	0.32	0.38

The predominant interactions between 14-MeV neutrons and Si are elastic (n,n) and inelastic (n,n') scattering. These reactions are assumed to occur with Si^{28} which has an abundance of 92.3%. All other reactions, such as (n,p), (n,α), (n,d), and (n,np), have much smaller cross sections. Both (n,n) and (n,n') interactions have cross sections of approximately 0.9 barns. In past work, most interest focused on the elastic reaction while ignoring the inelastic.

Because of the high energy of the 14-MeV neutron, elastic scattering of Si^{28} produces the typical "diffraction-like" differential elastic cross section, $d\sigma_{el}/d\Omega$. The $d\sigma/d\Omega$ reported in the literature is in center-of-mass coordinates (CM). To be useful in analyzing effects in pinch resistors, cross sections need to be converted to the laboratory frame of reference (LAB). The relationship between LAB and CM angles is $\theta_{LAB} = \frac{1}{2}(\pi - \theta_{CM})$, while the LAB recoil energy (T) of the Si is given by

$$T = T_m \sin^2(\theta_{CM}/2) \quad , \tag{10}$$

where T_m is the maximum recoil energy.[35] Using standard statistical methods based on the theory of probability distributions for functions of random variables,[36] $d\sigma_{el}/d\Omega$ was converted to an elastic recoil energy distribution (Figure 33) and a recoil LAB angular distribution (Figure 34). These two distributions are not independent. For each energy there is a specific angle for which a recoil occurs. The elastic energy distribution is highly peaked at low energies. These low-energy PKAs will be scattered nearly perpendicular to the incident neutron direction. High-energy PKAs due to elastic scattering are relatively rare but much more forward directed.

The Si^{28} nucleus contains a very large number of states below 14 MeV. Starting with the first excited state at 1.78 MeV above the ground state, other excited states are at 4.61, 4.97, 6.27, and 6.88 MeV.[37] The compound nucleus formed with a 14-MeV neutron is sufficiently excited to allow the use of the statistical model for inelastic scattering of 14-MeV neutrons from Si^{28}. In the CM, the angular distribution is isotropic while the scattered neutrons are said to "evaporate" from the compound nucleus with an energy spectrum

$$F(E) = C E \exp(-E/T_o) \quad , \tag{11}$$

51
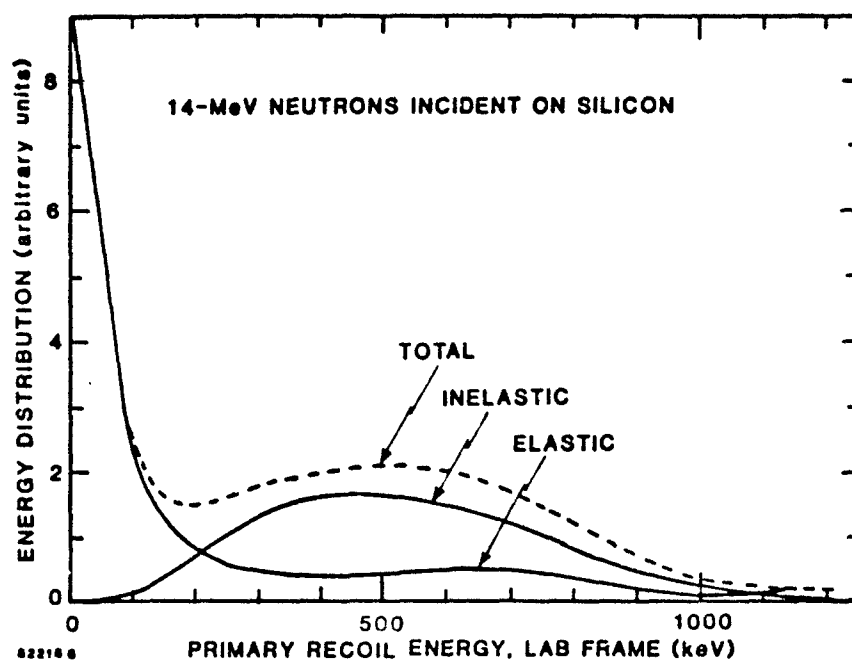
Figure 33. Distributions of primary recoil energies for elastic
and inelastic interactions in 14-MeV neutron-irradiated
silicon.
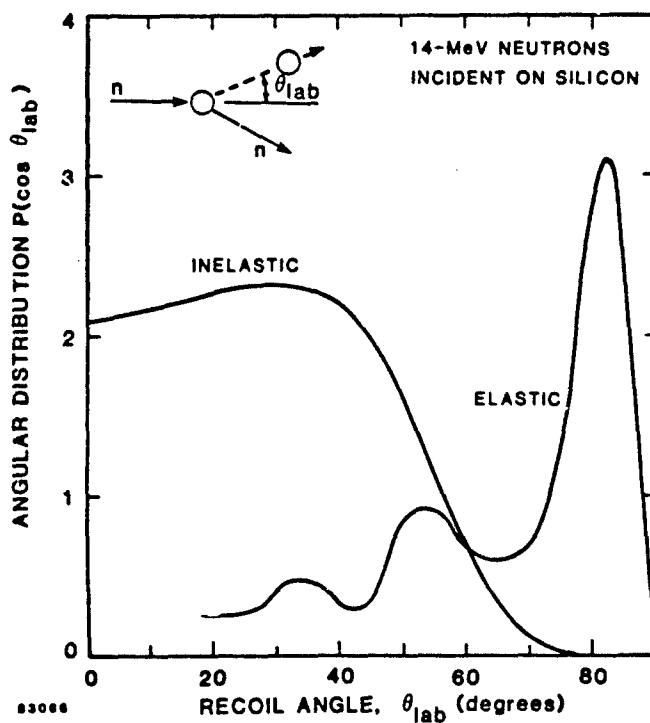
Figure 34. Angular distributions for elastic and inelastic
interactions in 14-MeV neutron-irradiated silicon.

where E is the energy of the emitted neutron in the CM frame and T_o is an effective temperature of the excited nucleus.[38] By conservation of momentum, the CM distribution of the recoil Si can be found.

The relationship connecting the LAB and CM reference frames is

$$\vec{V} = \vec{V'} + \vec{V}_c \quad , \tag{12}$$

where $\vec{V}$ and $\vec{V'}$ are the recoil velocities of the Si atom in LAB and CM frames, respectively; $\vec{V}_c$ is the velocity of the CM.[35] Since the recoil angular and energy distributions in the CM are independent, standard statistical methods can be used to calculate the recoil energy and recoil angular distributions.[36] Results are shown in Figures 33 and 34, respectively.

While the elastic recoil energy distribution is strongly peaked at very low energies, the inelastic distribution is very broad with a FWHM of ~600 keV and a peak at ~450 keV. The elastic angular distribution is peaked near 90° with respect to the direction of the incident neutron. Inelastically scattered recoil atoms are very strongly forward directed. The use of both interactions is necessary for an accurate description of the recoil atom.

4.2.4.2 Modeling. In order to analyze the pinch resistor results, the following physical model of the effects of neutron irradiation on these resistors was adopted. A flux of 14-MeV neutrons incident on the pinch resistors produces a distribution of PKAs with various energies and emission directions. These distributions were shown in Figures 33 and 34 for elastic and inelastic interactions. The PKAs interact with other Si atoms causing displacements and producing more recoiling atoms. The density of displacements is small near the beginning of the PKA range and large near the end. The low-defect-density regions probably contribute little to the measured change in resistance except as compensation centers. The high-defect-density regions can be viewed as localized damage clusters which act as nonconducting voids. Only those voids that overlap the sensitive volume of the pinch resistor will cause an increase in resistance. Since there is a distribution of PKA energies and angles, there are limits on the location of the neutron interactions which produce a PKA that can cause an overlapping void. The energy and angular distributions also result in a distribution of void sizes. Combining these effects results in a

53

distribution of resistance changes caused by the statistical nature of neutron interactions, PKA paths, and void sizes.

To make the model tractable, the following simplifications were adopted. Although the total differential cross section has been used to determine PKA energy distributions, only the relationship between angle and energy for elastic scattering is employed to calculate the resistance change distribution. This allows the use of a single independent distribution function (energy) instead of the two that would be required for inelastic scattering (energy and angle). The result is an underemphasis of the larger voids and the corresponding larger resistance changes. The pinch resistors used in the experiment have finite widths. By ignoring this in the model, edge effects are avoided.

Various estimates have been made of the extent and shape of the nonconducting void. The conventional picture developed by Gossick[39] and elaborated on by others has recently come into question based on detailed calculations using the binary-collision simulation code MARLOWE.[40] In the Gossick model, the PKA cascade produces a localized cluster of high defect density whose dimensions are a large fraction of the PKA range. This high defect density gives rise to a space-charge region which can be much larger than the defect cluster, depending on doping density. Alternatively, the MARLOWE code calculations predict that PKAs produce long trails of low defect density, some of which branch out, with very small clusters of approximately 50 Å diameter located at the end of the tracks. These tracks are expected to have much less of an effect on resistance than the small clusters which can be viewed as nonconducting voids.

In our approach, termed a distributed cluster model, we assume the conventional neutron-induced cluster model but take into account the detailed energy and elastic angular distributions. The cluster volume is treated as a spherical majority-carrier void. For each PKA energy, an average void diameter is obtained from EDEP code calculations.[41] This approach leads to a distribution of resistance changes that can be compared with experiment. Combining the use of only the elastic angular dependence with a spherical approximation for cluster shapes causes an underestimate of large resistance changes.

The calculations give the distribution of the resistance changes ($\Delta R/R$) for one cluster in the sensitive region of the pinch resistor. For a given

fluence, there are probabilities for obtaining different numbers of clusters given by a Poisson distribution. Multiple clusters will affect the resistance differently. To calculate the effects of multiple clusters, it was assumed that no overlapping voids occur. This results in calculating an overly large and very uniform resistance change distribution at large values of $\Delta R/R$ which is caused by many clusters. In addition, the fall-off from small $\Delta R/R$ is expected to be too fast. The difference between this model and the one used earlier[30] is that the previous distribution of resistance changes was proportional to the distribution of the number of clusters, with each cluster causing an average resistance change.

The results of the above calculations are shown in Figure 35 along with experimental data for a fluence of 5.2×10^{11} n/cm^2. Discrepancies between the predictions and the data are evident, as expected. Above $\Delta R/R$ of 0.5%, the calculated distribution is approximately uniform. Most importantly, the fall-off for the calculated distribution is much faster than that for the data. It is expected that modifications of the approximations used would produce a distribution that more closely reflects the data. However, the MARLOWE code predicts many very small clusters which we believe would enhance the discrepancies between calculations and data. Thus, even though no definitive conclusion can be made regarding the actual damage shapes introduced by the PKAs, our analysis indicates that the distributed cluster model provides a better prediction of the pinch resistor data than would a model based on MARLOWE code calculations.

4.2.5 Bipolar Transistor Results

Table 4 lists the percent change in collector current (I_c) for 2.3-μm bipolar transistors measured after each of the eleven irradiations. A similar listing for 3.1-μm devices is given in Table 5. Several transistors, including a few of the controls, exhibited behavior that was atypical of that for the two device populations. For the 2.3-μm device population, two of the controls (32/3 and 32/5) exhibited a significant unexplained decrease in I_c in the second set of measurements (column 2, Table 4). These two devices then remained as stable as the other four 2.3-μm controls for the remainder of the

55
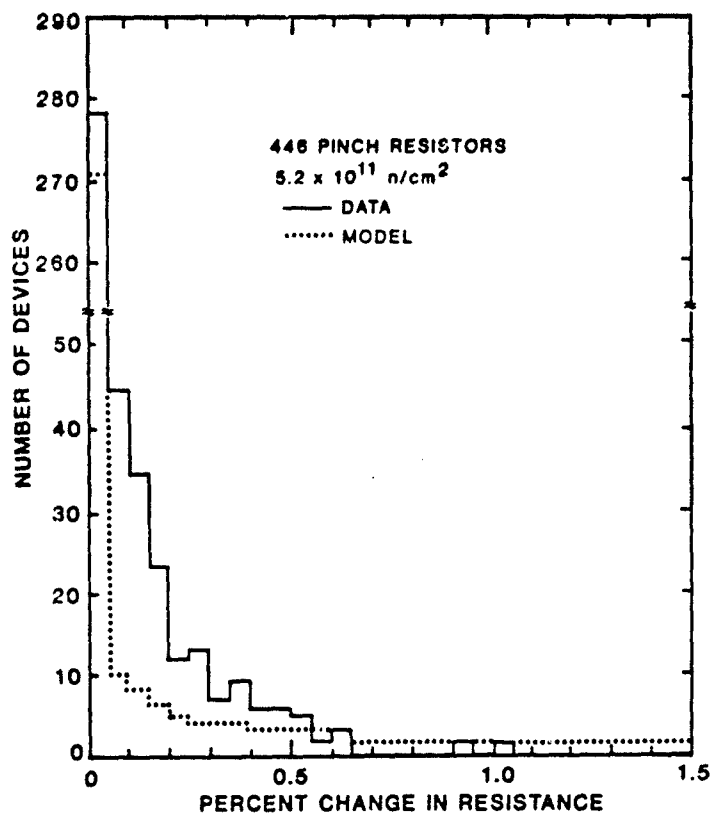
Figure 35. Comparison of experimental data for pinch
resistors with model calculations described
in the text.

experiment. One irradiated device (28/8) exhibited an atypically large decrease
in I_c ($\sim 2\%$) after the second irradiation. Its behavior thereafter was consis-
tent with the rest of the irradiated population. If this decrease was due to
the presence of a single damaged region in the intrinsic base, then from a sta-
tistical viewpoint similar decreases would have been observed in other devices
during the series of eleven irradiations. The absence of such decreases caused
us to throw out Device 28/8 in further data analysis. The effect observed in
this device is unexplained, but is most likely a reliability problem. The sim-
ilar effect noted in the two controls may have the same origin. The remainder
of the 2.3-μm device population was quite well-behaved and exhibited mutually
consistent behavior over the course of the entire experiment. This indicates
that only a few devices were unstable and that the remainder of the population
yielded a valid, reliable data set.

Table 4. Percent change in collector current measured for a population of 2.3-μm bipolar transistors after each of eleven 14-MeV neutron irradiations. (Neutron fluences are given in Table 2.) The first six devices listed are unirradiated controls.

DEVICE NUMBER	IRRADIATION NUMBER										
	1	2	3	4	5	6	7	8	9	10	11
21/1	0.06	0.14	0.15	0.24	0.18	0.19	0.23	0.28	0.29	0.29	0.19
21/3	0.06	0.03	-0.05	0.00	-0.11	-0.00	0.13	0.01	0.02	0.02	-0.07
21/7	0.05	0.03	-0.02	0.03	0.03	0.05	0.04	0.06	0.03	0.02	0.02
32/3	0.02	-0.61	-0.65	-0.79	-0.82	-0.72	-0.68	-0.77	-0.64	-0.76	-0.56
32/5	-0.01	-0.43	-0.39	-0.59	-0.61	-0.42	-0.42	-0.49	-0.31	-0.61	-0.31
32/7	0.07	0.07	0.12	-0.09	-0.10	-0.02	-0.07	-0.06	-0.09	-0.12	0.00
22/1	-0.04	-0.11	-0.29	-0.37	-0.45	-0.57	-0.66	-1.12	-1.73	-2.07	-2.31
22/2	-0.06	-0.16	-0.29	-0.34	-0.56	-0.76	-0.92	-1.28	-1.85	-2.28	-2.47
22/3	-0.00	-0.20	-0.34	-0.45	-0.62	-0.82	-0.84	-1.44	-1.83	-2.18	-2.45
22/4	-0.12	-0.27	-0.28	-0.35	-0.46	-0.63	-0.81	-1.24	-1.77	-2.06	-2.37
22/5	-0.08	-0.11	-0.36	-0.39	-0.46	-0.48	-0.58	-0.86	-1.16	-1.17	-1.16
22/7	-0.13	-0.33	-0.44	-0.49	-0.69	-0.86	-0.91	-1.46	-1.86	-2.20	-2.59
22/8	-0.13	-0.27	-0.46	-0.54	-0.73	-0.86	-0.98	-1.59	-1.78	-2.16	-2.50
23/3	0.01	-0.08	-0.18	-0.24	-0.32	-0.44	-0.47	-0.87	-1.08	-1.39	-1.72
23/4	-0.06	-0.07	-0.19	-0.19	-0.30	-0.37	-0.45	-0.59	-0.74	-0.91	-1.00
23/5	0.01	-0.12	-0.38	-0.32	-0.42	-0.32	-0.44	-0.63	-0.75	-0.85	-0.97
23/8	0.00	-0.24	-0.37	-0.45	-0.57	-0.64	-0.68	-1.14	-1.37	-1.67	-1.94
24/1	-0.06	-0.24	-0.35	-0.37	-0.57	-0.71	-0.93	-1.27	-1.56	-1.81	-2.14
24/2	-0.05	-0.27	-0.45	-0.51	-0.72	-0.74	-0.98	-1.28	-1.65	-2.03	-2.28
24/8	0.10	-0.13	-0.22	-0.31	-0.33	-0.44	-0.42	-0.77	-0.91	-1.19	-1.21
25/1	-0.20	-0.32	-0.54	-0.54	-0.68	-0.77	-0.98	-1.15	-1.34	-1.51	-1.68
25/2	-0.11	-0.12	-0.28	-0.37	-0.55	-0.60	-0.81	-1.02	-1.28	-1.45	-1.67
25/3	-0.12	-0.14	-0.40	-0.53	-0.74	-0.88	-0.97	-1.57	-1.82	-2.26	-2.66
25/4	-0.23	-0.26	-0.36	-0.42	-0.59	-0.56	-0.73	-0.95	-1.30	-1.31	-1.46
25/5	-0.11	-0.28	-0.57	-0.59	-0.73	-0.71	-1.03	-1.33	-1.62	-1.74	-1.80
25/6	-0.12	-0.26	-0.34	-0.53	-0.72	-0.78	-0.98	-1.40	-1.53	-1.72	-1.84
25/7	-0.12	-0.29	-0.39	-0.53	-0.69	-0.77	-0.90	-1.27	-1.53	-1.69	-1.88
26/1	0.10	-0.11	-0.14	-0.27	-0.30	-0.44	-0.81	-1.06	-1.46	-1.78	-2.05
26/2	0.16	-0.11	-0.12	-0.34	-0.39	-0.43	-0.66	-0.90	-1.37	-1.63	-1.89
26/5	0.18	-0.18	-0.19	-0.26	-0.13	-0.09	-0.32	-0.44	-0.89	-1.07	-0.80
27/1	-0.19	-0.28	-0.56	-0.68	-0.72	-0.76	-0.94	-1.19	-1.53	-1.70	-1.98
27/2	-0.14	-0.29	-0.62	-0.79	-0.86	-0.83	-1.04	-1.31	-1.72	-1.89	-1.97
28/1	-0.13	-0.30	-0.36	-0.51	-0.59	-0.67	-0.87	-1.20	-1.44	-1.71	-1.87
28/2	-0.13	-0.37	-0.46	-0.55	-0.57	-0.70	-0.85	-1.17	-1.35	-1.60	-1.59
28/4	-0.25	-0.45	-0.49	-0.69	-0.70	-0.70	-0.96	-1.18	-1.31	-1.47	-1.43
28/5	-0.15	-0.40	-0.49	-0.62	-0.70	-0.79	-0.93	-1.43	-1.68	-2.06	-2.24
28/6	-0.18	-0.38	-0.51	-0.61	-0.75	-0.82	-1.07	-1.42	-1.65	-1.91	-1.93
28/7	-0.03	-0.25	-0.43	-0.57	-0.72	-1.00	-1.14	-1.69	-2.14	-2.61	-2.85
28/8	0.05	-2.07	-2.30	-2.43	-2.65	-2.92	-3.07	-2.89	-3.19	-3.53	-3.71
29/1	-0.08	-0.25	-0.28	-0.40	-0.53	-0.48	-0.62	-0.82	-1.17	-1.22	-1.39
29/3	-0.15	-0.31	-0.24	-0.38	-0.42	-0.36	-0.31	-0.57	-0.53	-0.56	-0.63
29/5	-0.17	-0.39	-0.42	-0.51	-0.65	-0.45	-0.50	-0.68	-0.87	-0.80	-0.94
29/8	-0.13	-0.36	-0.45	-0.58	-0.60	-0.60	-0.63	-0.84	-1.08	-1.00	-0.95
30/1	-0.08	-0.15	-0.31	-0.36	-0.51	-0.59	-0.83	-1.02	-1.30	-1.50	-1.44
30/2	-0.14	-0.22	-0.40	-0.59	-0.78	-0.92	-1.09	-1.35	-1.68	-1.98	-1.92
30/3	-0.20	-0.16	-0.41	-0.55	-0.66	-0.73	-0.80	-1.00	-1.10	-1.37	-1.26

Table 4. Percent change in collector current measured for a population of
2.3-μm bipolar transistors after each of eleven 14-MeV neutron
irradiations. (Neutron fluences are given in Table 2.) The first
six devices listed are unirradiated controls. (Concluded)

| DEVICE | IRRADIATION NUMBER | | | | | | | | | | |
NUMBER	1	2	3	4	5	6	7	8	9	10	11
31/2	-0.26	-0.42	-0.52	-0.76	-0.90	-1.04	-1.33	-1.83	-2.31	-2.65	-3.03
31/5	-0.20	-0.38	-0.43	-0.52	-0.72	-0.60	-0.85	-1.25	-1.44	-1.77	-1.95
31/6	-0.22	-0.32	-0.36	-0.44	-0.59	-0.54	-0.69	-1.03	-1.18	-1.19	-1.43
31/7	-0.11	-0.26	-0.29	-0.43	-0.53	-0.62	-0.79	-1.18	-1.54	-1.71	-2.01
31/8	-0.11	-0.27	-0.30	-0.43	-0.52	-0.55	-0.64	-0.90	-1.15	-1.22	-1.40
33/3	-0.15	-0.15	-0.54	-0.69	-0.91	-1.09	-1.28	-1.82	-2.14	-2.50	-2.70
33/4	-0.19	-0.09	-0.37	-0.56	-0.77	-1.02	-1.18	-1.59	-2.07	-2.52	-2.91
33/5	-0.43	-0.47	-0.73	-0.86	-1.11	-1.13	-1.36	-1.82	-2.06	-2.43	-2.65
33/6	-0.28	-0.28	-0.62	-0.86	-0.9?	-1.27	-1.56	-2.18	-2.60	-2.92	-3.22
33/7	-0.19	-0.26	-0.49	-0.68	-0.78	-1.05	-1.25	-1.78	-2.12	-2.34	-2.56
33/8	-0.23	-0.23	-0.47	-0.67	-0.83	-1.06	-1.29	-1.99	-2.40	-2.80	-3.04
34/1	-0.23	-0.45	-0.58	-0.61	-0.83	-0.96	-1.00	-1.32	-1.55	-1.83	-1.95
34/2	-0.07	-0.29	-0.42	-0.48	-0.68	-0.71	-0.85	-1.24	-1.34	-1.66	-1.71
34/8	-0.18	-0.48	-0.65	-0.83	-1.04	-1.22	-1.37	-1.82	-2.05	-2.29	-2.47
35/6	-0.18	-0.19	-0.42	-0.38	-0.48	-0.71	-0.93	-1.34	-1.67	-1.86	-1.96
35/7	-0.13	-0.12	-0.26	-0.32	-0.47	-0.70	-0.95	-1.43	-1.76	-2.09	-2.33
35/8	-0.18	-0.12	-0.29	-0.30	-0.41	-0.67	-0.89	-1.39	-1.61	-1.74	-1.88
36/1	-0.30	-0.41	-0.43	-0.49	-0.65	-0.74	-0.77	-1.12	-1.15	-1.33	-1.32
36/2	-0.20	-0.33	-0.39	-0.54	-0.70	-0.85	-1.00	-1.48	-1.78	-1.97	-2.17
36/6	-0.29	-0.39	-0.46	-0.53	-0.69	-0.69	-0.79	-1.08	-1.18	-1.29	-1.36
36/7	0.03	-0.17	-0.23	-0.21	-0.30	-0.19	-0.22	-0.26	-0.41	-0.37	-0.10
36/8	-0.15	-0.24	-0.35	-0.43	-0.52	-0.58	-0.74	-0.96	-0.92	-1.05	-1.12
37/4	-0.17	-0.23	-0.35	-0.56	-0.74	-0.92	-1.12	-1.56	-1.94	-2.24	-2.46
37/7	-0.04	-0.06	-0.26	-0.36	-0.58	-0.68	-0.81	-1.10	-1.33	-1.63	-1.84
37/8	-0.02	-0.08	-0.27	-0.34	-0.52	-0.62	-0.80	-1.34	-1.66	-1.94	-2.07
38/1	-0.18	-0.20	-0.43	-0.64	-0.80	-1.08	-1.36	-1.90	-2.26	-2.43	-2.69
38/3	-0.12	-0.11	-0.40	-0.54	-0.75	-1.00	-1.30	-1.87	-2.29	-2.62	-2.86
38/4	-0.21	-0.21	-0.38	-0.58	-0.77	-0.98	-1.27	-1.70	-2.15	-2.59	-3.06
38/5	-0.29	-0.30	-0.55	-0.73	-0.77	-0.97	-1.17	-1.53	-1.77	-2.00	-2.03
38/6	-0.18	-0.19	-0.43	-0.45	-0.69	-0.88	-1.07	-1.45	-1.72	-1.84	-2.18
38/7	-0.08	-0.08	-0.33	-0.45	-0.63	-0.86	-1.11	-1.63	-1.93	-2.14	-2.41
38/8	-0.04	0.08	-0.22	-0.26	-0.39	-0.55	-0.84	-1.19	-1.38	-1.71	-1.84
39/1	-0.08	-0.18	-0.18	-0.38	-0.54	-0.64	-0.84	-1.33	-1.63	-2.13	-2.42
39/4	-0.15	-0.23	-0.19	-0.42	-0.52	-0.56	-0.70	-1.20	-1.60	-2.02	-2.18
39/7	0.15	-0.04	-0.11	-0.15	-0.36	-0.39	-0.66	-1.19	—	-1.88	-2.11
39/8	0.06	-0.07	-0.23	0.34	-0.45	-0.51	-0.67	-1.17	-1.39	-1.91	-2.06
40/3	-0.20	-0.29	-0.44	-0.63	-0.91	-1.10	-1.26	-1.83	-1.96	-2.39	-2.53

For the 3.1-μm device population, one control device (32/11) and one irradiated device (40/11) exhibited anomalous behavior. The same argument given above for 2.3-μm transistors applies here as well. We have judged that the remainder of the 3.1-μm device population yielded a valid, reliable data set.

The most striking feature of the data is illustrated in Figures 36-38, where histograms for the 2.3-μm device population are shown after three of the eleven irradiations. In general, the entire population shifts with irradiation and discrete effects occurring in individual devices are not evident. This result is in sharp contrast to the pinch resistor data described above where the occurrence of isolated events is obvious. The gradual shift in the two transistor populations is illustrated in Figure 39 where the average percent change in I_c is plotted versus fluence for the eleven irradiations. A monotonic

Table 5. Percent change in collector current measured for a population of 3.1-μm bipolar transistors after each of eleven 14-MeV neutron irradiations. (Neutron fluences are given in Table 2.) The first two devices listed are unirradiated controls.

DEVICE NUMBER	IRRADIATION NUMBER										
	1	2	3	4	5	6	7	8	9	10	11
21/11	0.06	-0.01	-0.03	0.10	0.05	0.02	0.09	0.10	0.18	0.15	0.10
32/11	0.01	-1.65	-1.76	-2.09	-2.20	-2.63	-2.70	-2.49	-2.47	-2.67	-2.44
22/9	0.05	-0.18	-0.40	-0.52	-0.74	-0.93	-1.14	-1.64	-2.05	-2.27	-2.58
22/10	-0.03	-0.18	-0.37	-0.50	-0.70	-1.00	-1.04	-1.54	-1.99	-2.37	-2.78
22/11	0.00	-0.16	-0.29	-0.39	-0.54	-0.85	-0.93	-1.45	-1.86	-2.17	-2.51
23/9	0.15	-0.17	-0.34	-0.38	-0.57	-0.73	-0.90	-1.35	-1.65	-1.96	-2.36
23/11	0.07	-0.12	-0.31	-0.34	-0.51	-0.68	-0.79	-1.12	-1.38	-1.66	-2.06
24/9	-0.01	-0.26	-0.39	-0.48	-0.66	-0.83	-0.99	-1.42	-1.83	-2.20	-2.41
24/10	-0.04	-0.20	-0.34	-0.36	-0.59	-0.76	-0.86	-1.24	-1.56	-1.91	-2.19
26/10	0.15	-0.01	0.01	-0.08	-0.07	-0.08	-0.36	-0.47	-0.71	-0.79	-0.86
27/9	-0.16	-0.39	-0.73	-0.88	-1.03	-1.11	-1.29	-1.74	-2.21	-2.36	-2.55
27/10	-0.17	-0.30	-0.68	-0.94	-0.96	-1.02	-1.38	-1.89	-2.29	-2.51	-2.89
27/11	-0.18	-0.73	-1.03	-1.27	-1.32	-1.43	-1.70	-2.23	-2.68	-2.86	-3.18
28/10	-0.26	-0.42	-0.64	-0.80	-0.85	-1.11	-1.33	-1.79	-2.02	-2.39	-2.57
28/11	-0.22	-0.42	-0.63	-0.79	-0.86	-1.05	-1.17	-1.68	-2.06	-2.36	-2.52
29/9	-0.11	-0.36	-0.49	-0.73	-0.84	-0.95	-1.07	-1.52	-1.75	-1.99	-2.27
29/10	-0.21	-0.34	-0.42	-0.61	-0.67	-0.70	-0.83	-1.10	-1.46	-1.61	-1.81
29/11	-0.18	-0.35	-0.50	-0.65	-0.70	-0.77	-0.81	-1.31	-1.47	-1.64	-1.80
30/9	-0.20	-0.15	-0.58	-0.77	-1.01	-1.29	-1.49	-1.90	-2.32	-2.75	-2.82
30/11	-0.16	0.00	-0.45	-0.64	-0.79	-0.92	-1.13	-1.52	-1.87	-2.25	-2.37
31/9	-0.20	-0.36	-0.44	-0.68	-0.76	-0.79	-1.03	-1.51	-1.92	-2.16	-2.41
31/10	-0.17	-0.31	-0.45	-0.62	-0.76	-0.92	-1.13	-1.50	-1.84	-2.15	-2.47
31/11	-0.26	-0.38	-0.57	-0.77	-0.83	-0.89	-1.10	-1.43	-1.67	-1.83	-2.10
33/9	-0.20	-0.23	-0.54	-0.74	-0.94	-1.12	-1.34	-1.87	-2.08	-2.41	-2.60
33/10	-0.24	-0.24	-0.53	-0.63	-0.78	-1.17	-1.35	-1.82	-2.12	-2.37	-2.63
34/9	-0.30	-0.52	-0.73	-0.84	-1.01	-1.21	-1.30	-1.79	-2.16	-2.53	-2.72
35/9	-0.25	-0.22	-0.56	-0.66	-0.78	-1.03	-1.27	-1.78	-2.24	-2.63	-2.97
35/10	-0.27	-0.23	-0.53	-0.56	-0.69	-0.81	-1.00	-1.31	-1.57	-1.80	-2.04
36/11	-0.22	-0.35	-0.55	-0.66	-0.85	-0.98	-1.14	-1.40	-1.71	-1.92	-2.10
37/9	-0.11	-0.21	-0.40	-0.59	-0.73	-0.81	-0.85	-1.32	-1.65	-1.85	-2.16
37/10	-0.12	-0.13	-0.32	-0.51	-0.57	-0.70	-0.77	-1.18	-1.42	-1.70	-1.89
37/11	-0.08	-0.13	-0.33	-0.48	-0.66	-0.77	-0.95	-1.41	-1.65	-1.91	-2.10
39/9	-0.04	-0.23	-0.31	-0.56	-0.68	-0.79	-0.94	-1.52	-1.69	-2.20	-2.35
39/10	-0.06	-0.17	-0.23	-0.46	-0.54	-0.68	-0.93	-1.39	-1.72	-2.14	-2.28
39/11	-0.10	-0.21	-0.25	-0.46	-0.55	-0.61	-0.82	-1.34	-1.70	-2.05	-2.19
40/9	-0.21	-0.51	-0.80	-0.95	-1.32	-1.44	-1.64	-2.36	-2.57	-2.97	-3.19
40/10	-0.24	-0.36	-0.57	-0.65	-0.92	-1.36	-1.55	-2.21	-2.50	-2.79	-2.89
40/11	-1.03	-1.21	-1.42	-1.69	-2.30	-3.36	-3.67	-3.33	-3.55	-4.14	-4.35

decrease in I_c with fluence is evident for both device geometries. Another feature of the data, as shown in Figures 36-38, is that a spread in the spectrum occurs with increasing fluence in addition to a shift in the average value.

In our original study of neutron effects on bipolar transistors and pinch resistors identical to those used here,[30] only one fluence (3.1 x 10^{12} n/cm^2) was used. The resistor data were reasonably well understood, but the transistor data were not satisfactorily explained. We later decided[31] that
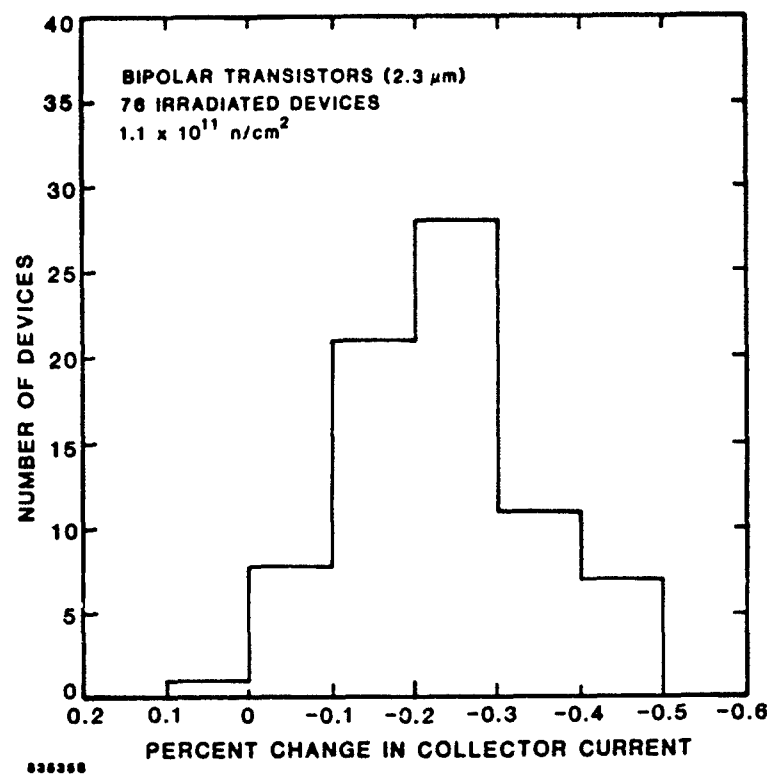
Figure 36. Histogram showing percent change in collector current for the irradiated 2.3-μm bipolar transistor population after 1.1×10^{11} n/cm^2.
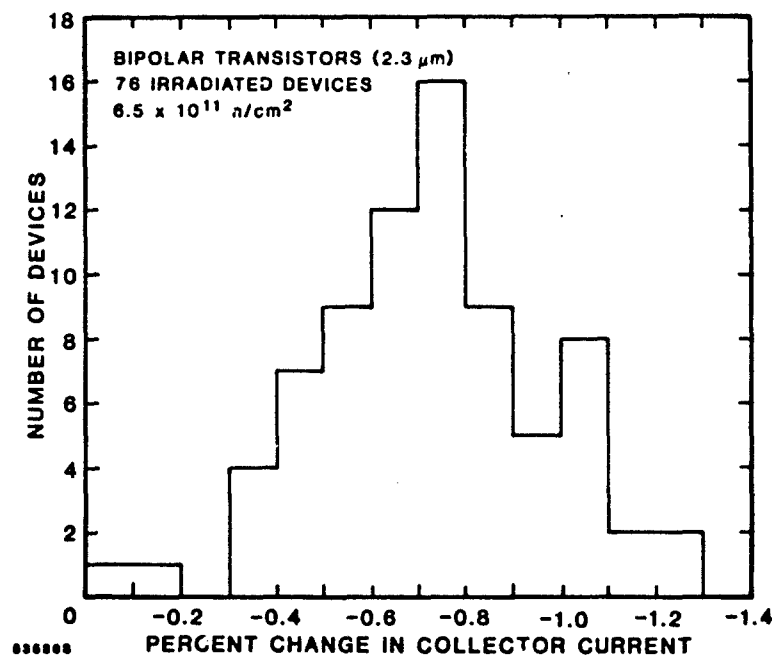
Figure 37. Histogram showing percent change in collector current for the irradiated 2.3-μm bipolar transistor population after 6.5×10^{11} n/cm^2.
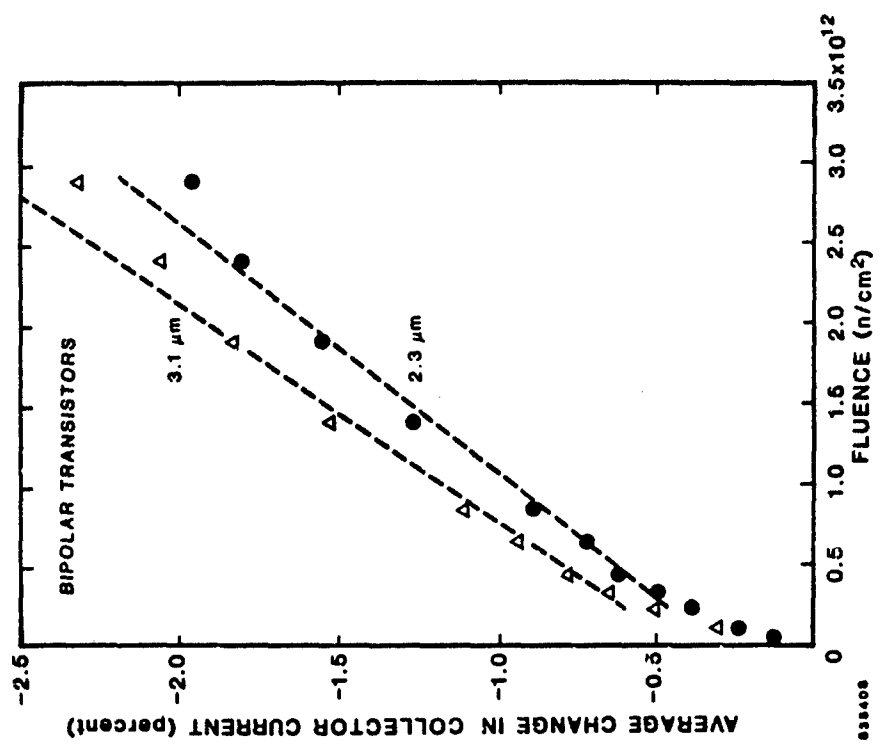
Figure 39. Average percent change in collector current vs. fluence for the two irradiated bipolar transistor populations.
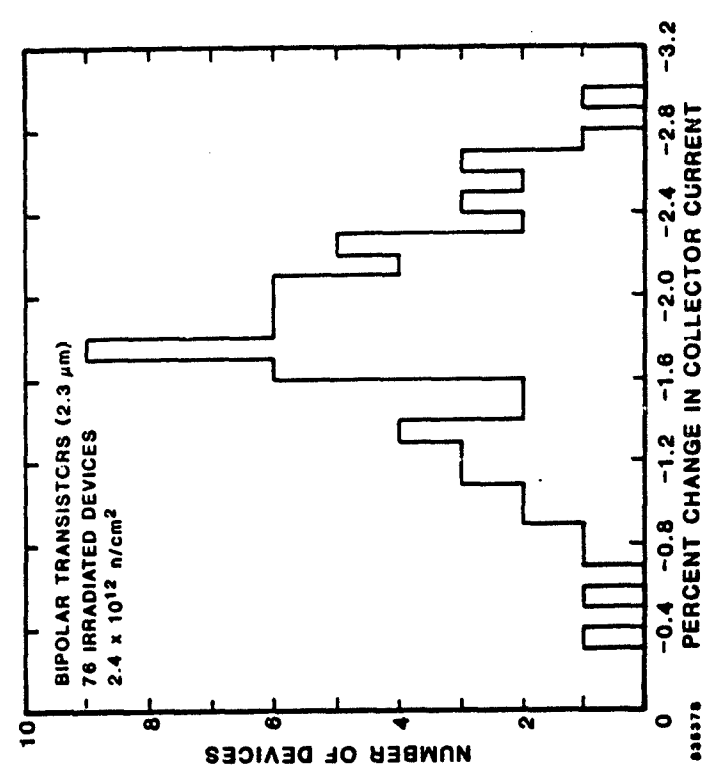

Figure 38. Histogram showing percent change in collector current for the irradiated 2.3-μm bipolar transistor population after 2.4 x 10^{12} n/cm^2.

61

I_c decreased in the irradiated transistors not only because of radiation-induced defects in the intrinsic base but also due to those present in the extrinsic base (Figure 24). The present data can be interpreted, at least qualitatively, on that basis. For example, at the highest fluence used (2.9×10^{12} n/cm^2) we calculate that, on the average, ~ 10 neutron interactions will have occurred in _every_ device in that portion of the extrinsic base expected to influence the collector current. In contrast, at that fluence an average of ~ 0.5 interactions will have occurred in the intrinsic base region of every device. These approximate calculations strongly suggest that the present transistor data are dominated by extrinsic base effects.

Additional analysis of the transistor data is planned, with the goal of determining the effect of a single neutron interaction on the collector current. Once that effect has been accurately determined based on our experimental findings, then the effect of a single interaction in the intrinsic base on transistor gain can be calculated for various VLSI geometries. Our plan of attack in this additional analysis is the following: 1) calculate the extrinsic and intrinsic contributions to pre-irradiation collector current for the present device geometry; 2) use the Poisson distribution and calculate the expected number of interactions in the extrinsic and intrinsic base regions as a function of fluence for the two device populations; 3) based on experimental data and results of the above calculations, determine the effect of a single defect cluster on collector current; take the cluster size distribution into account; 4) calculate the effect of a single damaged region on the gain in bipolar transistors of various geometries. Results of that work will be reported at a later date.

4.3 EXPERIMENTAL STUDY OF DISORDERED REGION PROPERTIES USING A SCANNING ELECTRON MICROSCOPE

During 1981, a program was initiated to observe single neutron-produced defect clusters through their effect on carrier recombination.[31] The experimental approach employed in this investigation was based on the use of a scanning electron microscope to yield a highly localized source of excess carriers. The variation in the electron-beam-induced current (EBIC) observed as the beam is scanned over an irradiated silicon sample was expected to reveal the influence of defect clusters. The selected test vehicle was a space-

quality thin silicon solar cell. Details of the experimental method as well as characterization of the solar cell prior to irradiation are given in reference 31.

In the present program, the test device was irradiated with 14-MeV neutrons to a fluence of 1.1×10^{11} n/cm^2. This fluence was chosen because of the desire, on the one hand, to have a reasonably high density of clusters to examine, and the necessity, on the other hand, not to degrade the diffusion length excessively because of the resulting loss in signal-to-noise ratio. Comparison of the pre- and post-irradiation data showed a significant reduction in the signal level. This reduction was translated into a macroscopic degradation of the minority-carrier lifetime. A recombination-lifetime neutron damage coefficient K_r was then determined through the relationship

$$\tau^{-1} = \tau_0^{-1} + \phi/K_r \quad , \tag{13}$$

where ϕ is fluence and τ_0 and τ are pre- and post-irradiation lifetimes, respectively. The damage coefficient was found to be $\sim 1 \times 10^5$ n-sec/cm^2. This coincides with the expected value extrapolated from higher resistivity data.[42] Another result of the irradiation was an increase by a factor of two of the noise level in the EBIC signal. Unfortunately, this increase in noise resulted in signal variations of a magnitude comparable to that expected for a single cluster. Hence, under the present experimental conditions individual damage clusters could not be discerned. Signal averaging of multiple data traces could, in principle, reduce the noise to the point where individual regions might be observable.

4.4 EXPERIMENTS ON MOS/VLSI TRANSISTORS

4.4.1 Introduction

The potential effects of a single neutron-produced disordered region on the electrical properties of small-geometry MOS transistors are described in Ref. 30. The anticipated effects are: threshold voltage shift, channel mobility degradation, and increased drain leakage current. We have performed experiments on MOS/VLSI transistors in an attempt to examine the validity of those concepts. Electrical properties were measured before and after a series of 14-MeV neutron irradiations.

4.4.2 Devices

A population of 42 unhardened n-channel MOS/VLSI transistors was used in this study, two of which were unirradiated controls. The gate oxide thickness was 45-50 nm and the substrate doping concentration was 2.3×10^{16} cm^{-3}. These devices were contained in nine chips, designated as numbers 41, 43, 46, 47, 49, 50, 52, 53, and 54. The individual transistors on a given chip were assigned the numbers given in Table 6, which also lists the device dimensions. For example, 46/10 designates transistor number 10 on chip number 46. (The yield was relatively low, so on some chips only a few devices were usable.)

Table 6. Channel width and channel length for MOS/VLSI transistors included in this investigation.

Device Number	Channel Width (μm)	Channel Length (μm)
/ 0	1.0	0.5
/ 1	2.0	0.5
/ 2	1.5	1.0
/ 3	1.0	1.0
/ 4	2.0	1.0
/ 5	2.0	1.5
/ 6	1.5	1.5
/ 9	2.0	1.5
/10	1.5	1.5
/11	2.0	1.0
/12	1.0	1.0
/13	1.5	1.0

4.4.3 Experimental Methods

The individual transistors were switched into test circuits under computer control. Parameters measured included leakage current, transconductance, and threshold voltage. All tests were performed in a temperature environment of $31 \pm 0.5°C$. The measurement system and its capabilites are described here.

Figure 40 shows a simplified version of the test circuit used to measure leakage current. A Keithley Model 616 Electrometer was used to measure the current to a resolution of 1 picoampere, with 0.2% full-scale accuracy.

HP 6113A
POWER SUPPLY

+V   −V

HP 3456A
DVM

TO
COMPUTER

KEITHLEY 616
ELECTROMETER

G   D
S

83087
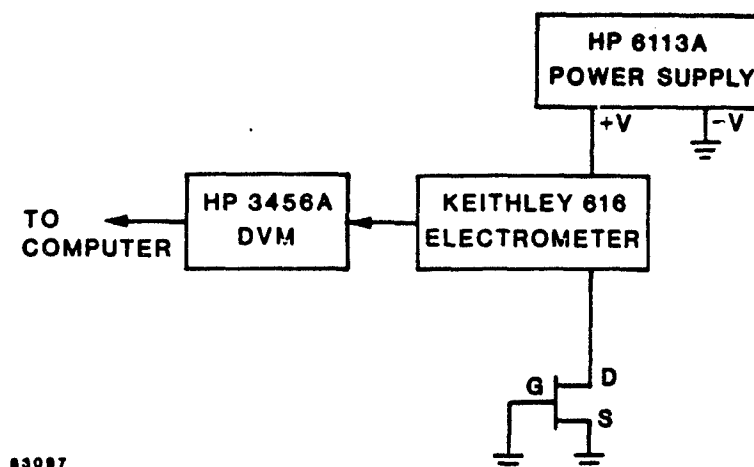
Figure 40. Simplified diagram of test set-up used
to measure leakage current.

A Hewlett-Packard Model 3456A DVM was used to read the output of the Keithley
and feed it to a Hewlett-Packard Model 9826 computer. The computer controlled
all test functions and also received and stored all data. Leakage current was
measured fourteen times. The average of these readings and its standard devia-
tion were stored on disc memory for later use.

Transconductance and threshold voltage were measured in the following
manner. A gate-to-source voltage (V_{gs}) of 100 mV was applied to a transistor
and the resultant drain current (I_d) measured and retained. V_{gs} was then in-
cremented by 25 mV and a new I_d measured. This process was continued until a
plot of I_d vs. V_{gs} was obtained. (See Figure 41.) The major slope of this
curve was then defined as the transconductance (g_m) and the voltage intercept
was defined as the threshold voltage (V_t). After g_m and V_t were obtained, the
entire test was repeated to obtain new values of g_m and V_t. This procedure
was repeated until fourteen values were obtained. The average of these values
and its standard deviation were stored on disc memory for later use. Figure 42
shows a simplified version of the test circuit used. Gate excitation was sup-
plied via a Hewlett-Packard Model 44429A digital-to-analog converter (DAC)
under computer control. Drain current was determined by measuring the voltage
drop across a precision resistor in the drain supply line. Figure 43 shows a
detailed wiring diagram of the test circuit. A simplified version of the com-
puter test flow diagram is shown in Figure 44.

SLOPE = g_m

I_d

V_t V_{gs}

83098
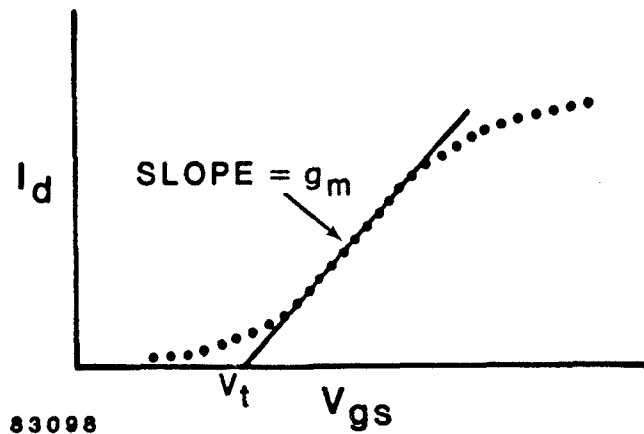
Figure 41. Plot of I_d vs. V_{gs} showing definition of transconductance (g_m) and threshold voltage (V_t).

HP 6113A
POWER SUPPLY

HP 3456A
DVM

TO
COMPUTER

+V   +V
(SENSE)   −V

10K
0.1%

$V_D = 100 \pm 0.5$ mV

FROM
COMPUTER

HP 44429A
DAC

G   D

S

83099
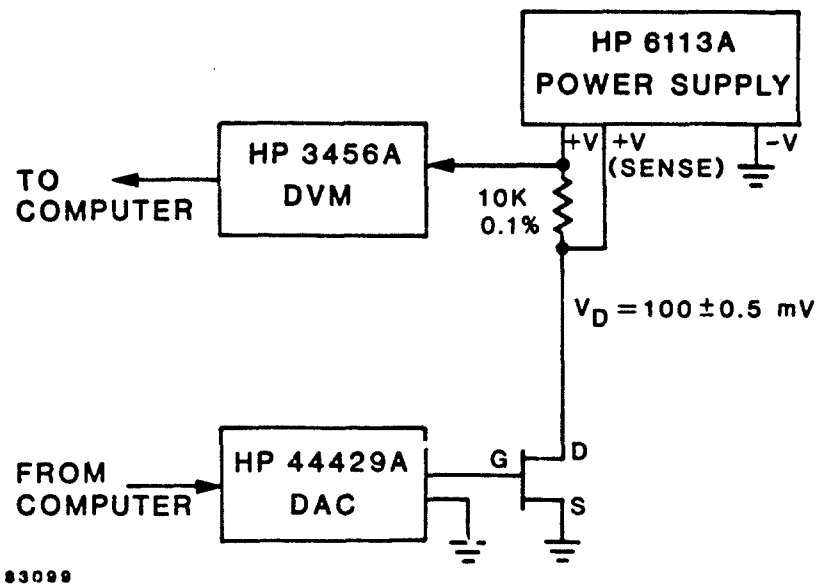
Figure 42. Simplified diagram of test set-up used to measure transconductance and threshold voltage.

66
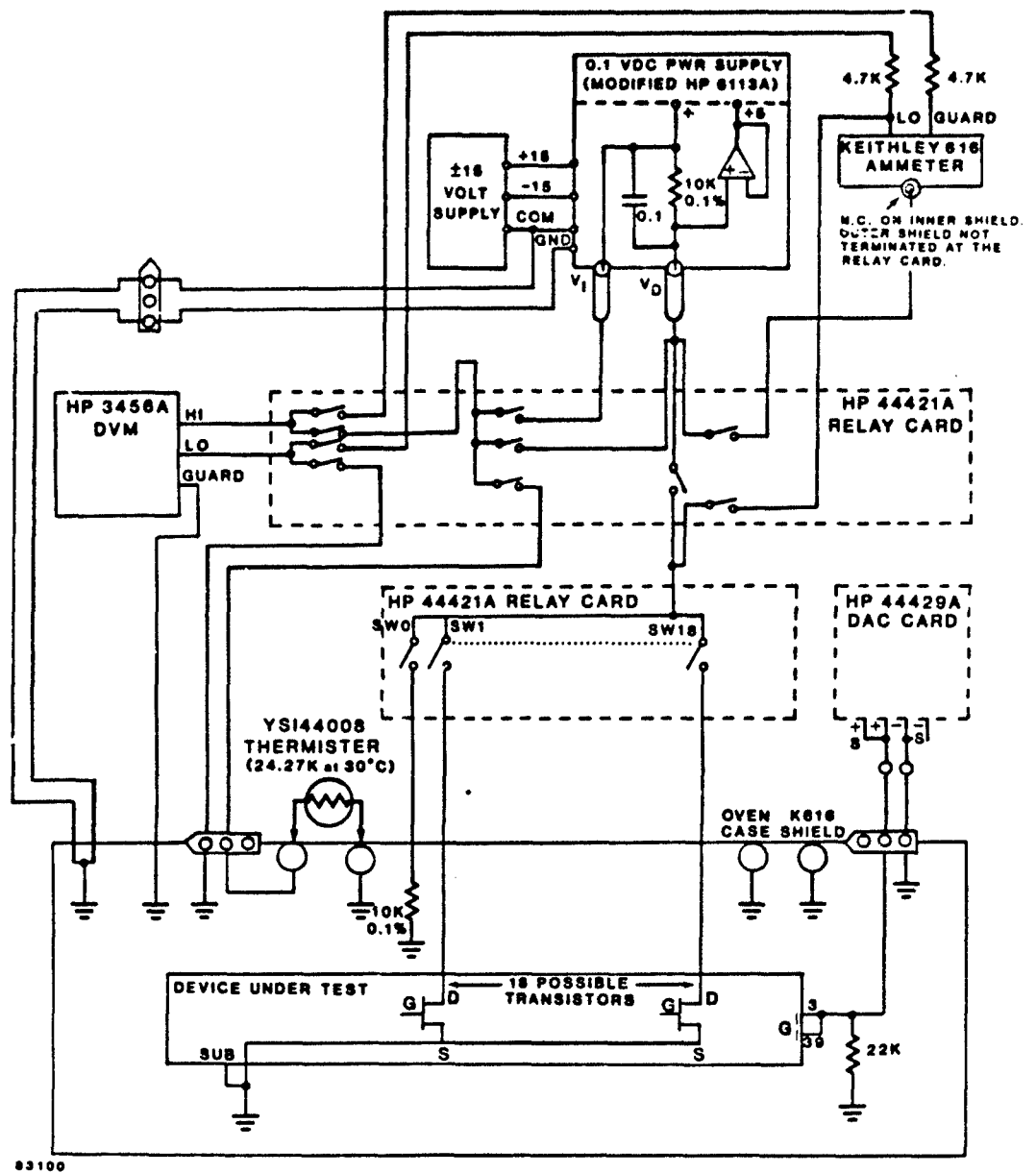
Figure 43. Wiring diagram for the circuit used in measuring leakage current, transconductance, and threshold voltage.
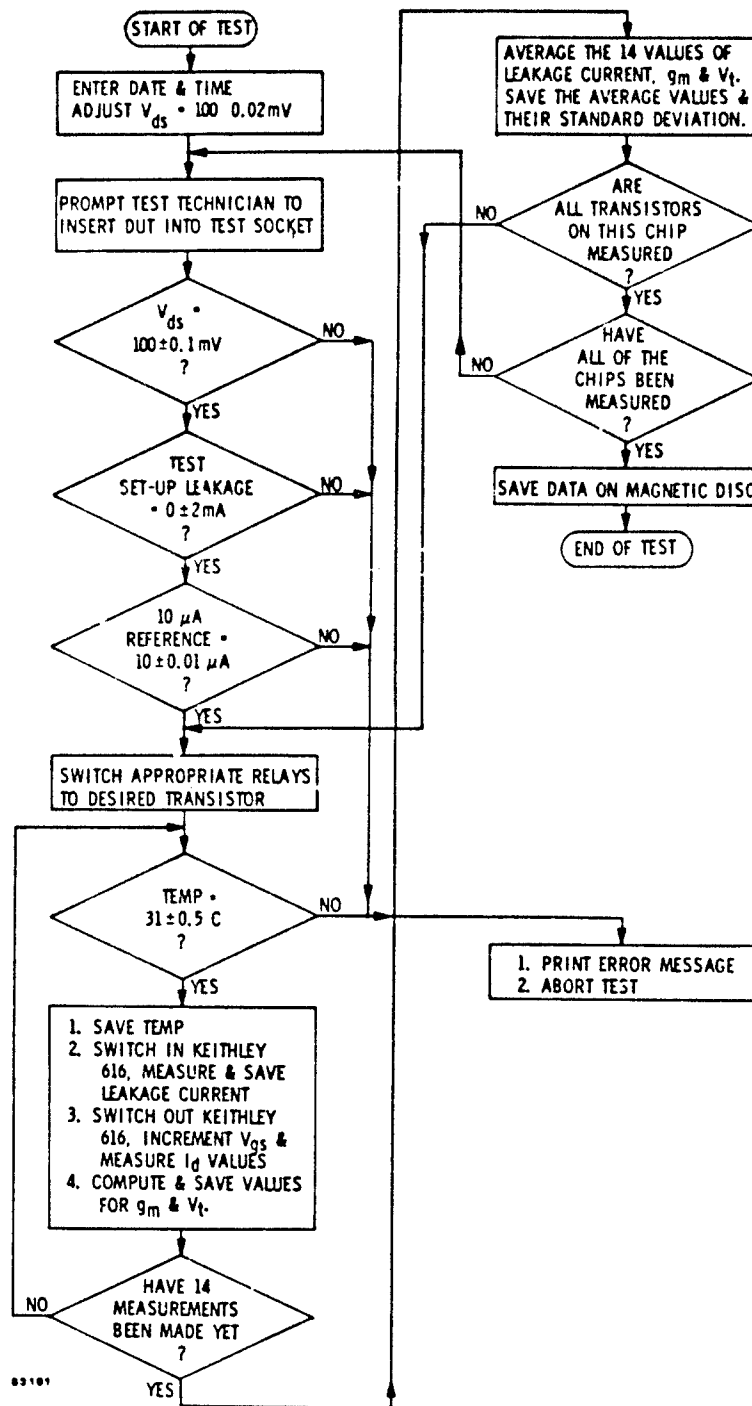
Figure 44. Simplified computer test flow diagram employed in MOS/VLSI transistor measurements.

68

A complete data set was obtained for the entire device population on a given day in the manner described above. In an attempt to improve experimental accuracy, additional complete data sets were obtained on subsequent days. Typically, five such sets were obtained and averaged. The resulting standard deviation, expressed as a percentage of the mean value, was < 1% for pre-irradiation threshold voltage and transconductance readings. For leakage current, the percent standard deviation was relatively large (> 10%) for devices with very low leakage (i.e., tens of picoamperes) and relatively small (< 1%) for devices with high leakage (i.e., tens of nanoamperes). Large standard deviations occurred when the measured leakage current was on the order of the system noise level. (Emphasis in this investigation was placed on examining radiation-induced changes in threshold voltage and not on transconductance and leakage current. The data presentations and related discussion given below reflect that emphasis.) After the last neutron irradiation, the percent standard deviation for V_t was < 1% for only one-half of the device population. Most of the remainder had a standard deviation < 3%, with a few exhibiting higher values. This decrease in experimental accuracy is attributed to a degradation with time in the operating stability of a portion of the population.

14-MeV neutron irradiations were conducted at the Lawrence Livermore Laboratory RTNS-II source. Four irradiations were performed under zero bias conditions, and the fluences are listed in Table 7. Following the series of neutron exposures, additional zero-bias irradiations were performed at the Northrop Research and Technology Center Co-60 source. Six irradiations were performed on chips 50 and 53 before annealing, and the total ionizing doses are listed in Table 8. Five Co-60 irradiations were also performed on chips 43, 47, and 49 and on chips 50 and 53 after annealing. Total doses used are listed in Table 9.

4.4.4 Results and Discussion

Table 10 lists threshold voltage shifts (ΔV_t) measured for the device population after each of the four neutron irradiations. In general, the population exhibits a monotonic decrease in V_t with fluence. There are a few exceptions, however. One of the unirradiated control devices (46/13) became unstable and exhibited a significant ΔV_t after the first two irradiations, then subsequently stabilized. The other control exhibited a small, but reasonably constant, ΔV_t. Devices 41/1 and 41/2 behaved in a manner consistent with the

69

Table 7. 14-MeV neutron fluences used in irradiations of MOS/VLSI transistors.

Irradiation Number	Incremental Fluence	Cumulative Fluence
1	5.7×10^{12} n/cm^2	5.7×10^{12} n/cm^2
2	1.2×10^{13}	1.8×10^{13}
3	2.2×10^{13}	3.9×10^{13}
4	5.6×10^{13}	9.6×10^{13}

Table 8. Total ionizing doses used in Co-60 irradiations of chips 50 and 53 before annealing.

Irradiation Number	Incremental Dose	Cumulative Dose
1	1.0×10^2 rad(Si)	1.0×10^2 rad(Si)
2	9.0×10^2	1.0×10^3
3	9.0×10^3	1.0×10^4
4	2.0×10^4	3.0×10^4
5	7.0×10^4	1.0×10^5
6	2.0×10^5	3.0×10^5

Table 9. Total ionizing doses used in Co-60 irradiations of chips 43, 47, 49, 50, and 53. (Irradiations of chips 50 and 53 were performed after an anneal, as discussed in the text.)

Irradiation Number	Incremental Dose	Cumulative Dose
1	2.4×10^3 rad(Si)	2.4×10^3 rad(Si)
2	2.6×10^3	5.0×10^3
3	5.0×10^3	1.0×10^4
4	1.0×10^4	2.0×10^4
5	3.0×10^4	5.0×10^4

Table 10. Threshold voltage shifts (in mV) measured for a population
of MOS transistors after each of four 14-MeV neutron irradiations. (Neutron fluences are given in Table 7.) The
first two devices listed are unirradiated controls.

DEVICE NUMBER	NEUTRON IRRADIATION NUMBER			
	1	2	3	4
46/ 10	-10.02	-8.20	-4.81	-6.54
46/ 13	63.03	133.82	130.41	127.06
41/ 1	-5.84	-20.28	-43.07	129.13
41/ 2	-6.24	-15.45	-34.32	-471.18
41/ 12	-9.89	-31.95	-39.90	-74.47
43/ 1	-14.67	-26.91	-60.88	-132.71
43/ 2	-11.71	-29.42	-58.45	-93.26
43/ 3	-14.19	-43.35	-70.89	-110.03
43/ 4	-7.45	-18.73	-39.80	-81.44
43/ 5	-10.05	-21.39	-40.89	-76.82
43/ 6	-7.81	-18.48	-36.68	-70.26
43/ 9	-8.42	-20.00	-40.19	-73.81
43/ 10	-9.99	-18.97	-32.96	-63.10
43/ 11	-6.53	-15.69	-32.77	-63.78
43/ 12	-8.00	-27.34	-52.50	-99.49
47/ 2	-8.87	-20.71	-30.45	-43.31
47/ 3	-12.13	-28.40	-37.98	-42.69
47/ 4	-4.97	-10.87	-18.21	-30.01
47/ 5	-5.59	-10.04	-17.67	-26.61
47/ 6	-7.72	-14.83	-22.47	-32.03
47/ 9	-6.47	-10.03	-25.53	-35.31
47/ 11	-3.30	-1.40	0.80	-15.55
49/ 2	-6.55	-17.37	-36.80	-66.07
49/ 3	-11.80	-28.74	-47.90	-79.69
49/ 5	-9.38	-19.14	-36.90	-58.78
49/ 6	-6.28	-15.35	-28.65	-55.32
49/ 9	-8.40	-22.23	-38.19	-78.54
49/ 11	-4.94	-10.02	-26.54	-63.45
49/ 12	-15.04	-22.85	-48.08	-88.69
49/ 13	-8.66	-18.26	-52.33	-114.55
50/ 2	-13.74	-32.70	-76.08	-119.39
50/ 3	-27.49	-51.92	-79.23	-135.28
50/ 4	-10.00	-24.96	-47.40	-91.93
50/ 9	-9.27	-20.13	-37.89	-73.92
50/ 10	-9.71	-25.61	-44.87	-82.21
52/ 6	-25.35	-58.76	-70.09	-78.64
53/ 9	-3.94	-12.16	-19.90	-30.82
53/ 10	-4.02	-13.00	-15.38	-17.10
53/ 11	-3.25	-9.07	-11.67	-17.42
53/ 13	-5.70	-9.68	-18.42	-35.89
54/ 0	-7.74	-17.12	-46.20	-89.52
54/ 2	-5.60	-11.85	-26.31	-47.56

rest of the population for the first three irradiations. After the fourth bombardment, these devices exhibited large changes in V_t which are most likely associated with the onset of an electrical instability or a device reliability problem. Device 47/11 also exhibited anomalous behavior in that very little radiation-induced change in V_t was observed.

The monotonic change in ΔV_t with irradiation observed for nearly all devices in the population was not anticipated. We were looking for occasional discrete changes in electrical properties similar to those noted in the pinch resistor experiments described in Section 4.2.3. Examples of the types of behavior actually observed are shown in Figures 45 and 46. Most of the devices behaved like 49/6 and 50/10 (Figure 45), exhibiting a slightly sublinear increase in $-\Delta V_t$ with fluence. A few devices exhibited the onset of saturation (52/6 and 53/10 in Figure 45). A few other devices showed a change in slope, as illustrated in Figure 46. We initially hypothesized that these slope changes were due to single neutron interactions in the channel region of a given device. As an example, if the third irradiation of device 41/12 produced a single defect cluster in the silicon substrate very near the SiO_2-Si interface, then the resulting Fermi-level pinning (postulated in Ref. 30) would make it more difficult to turn the device on. The subsequent shift in V_t would be in a direction opposite to that produced by positive charge buildup in the gate oxide.

Nearly all of the data suggest that some background effect occurred continuously, such as positive charge buildup due to ionizing radiation. If discrete neutron effects, such as that just described, did occur, then they would appear as perturbations on the background. This is a possible explanation for a slope change. The behavior exhibited by most devices (e.g., 49/6 and 50/10) is what one would expect for MOS devices in a purely ionizing radiation environment. In addition, the saturation exhibited in some cases (e.g., 52/6 and 53/10) is consistent with the formation of negatively charged interface states which begin to compensate for the built-up positive charge in the gate oxide. Two questions then arise: 1) Did the devices receive a background ionizing dose? 2) Are the slope changes evident in Figure 46 due to individual neutron interactions? These issues were addressed and our findings are now described.

Figure 46. Threshold voltage shift vs neutron fluence for irradiated MOS transistors.

Figure 45. Threshold voltage shift vs neutron fluence for irradiated MOS transistors.

73

It was necessary to irradiate the MOS transistor population to relatively high fluences because the population size and the device sizes were small. Thus, a relatively large fluence was required to produce a single neutron interaction in a device critical region. For example, the fluence needed to produce a single interaction within 10 nm of the SiO_2-Si interface in one device out of forty (assuming a 1 μm x 1 μm size) is calculated to be $\sim 3 \times 10^{13}$ n/cm^2. In addition, we simultaneously irradiated all chips, which were mounted in DIPs. The irradiated area was ~ 25 in^2 (~ 5 in x 5 in). To achieve a uniform fluence for all devices, it was therefore necessary to place the packages relatively far from the target at the RTNS-II facility. (For the first irradiation, the distance was 100 cm; for the other three irradiations, the distances varied from 50 to 58 cm.) Thus, irradiation times were of necessity relatively long.

Quantitative information regarding the background ionizing dose rate during neutron bombardment was not available. We assumed (evidently erroneously, as shown below) that this rate was low enough to be unimportant in the present experiment. Likely sources of an ionizing background are: 1) inelastic neutron scattering from the exposure room walls; 2) air ionization; 3) target activation; 4) activation of materials present in our experiment and in others being conducted simultaneously. Personnel at the RTNS-II source estimate that there is typically not a significant dependence of the background dose rate on position in the exposure room. Thus, to minimize the background total dose received, the irradiation time should be minimized. In our case, in retrospect we could have moved a factor of ~ 2 closer to the target and still have achieved about $\pm 10\%$ uniformity in neutron fluence over the irradiation area. This would have reduced the bombardment time, and thus the total ionizing dose, by a factor of ~ 4. Alternatively, chips could have been irradiated individually at a position much closer to the target. Another approach in a future experiment would be to use a significantly larger device population so that the required fluence, and thus the irradiation time, would be substantially reduced.

We next performed Co-60 gamma irradiations of the MOS devices in an attempt to determine whether the observed slope changes were due to neutron interactions and whether the results obtained from neutron irradiations were dominated by background ionization. Table 11 lists threshold voltage shifts measured for devices contained in chips 50 and 53 after a series of ionizing irradiations.

Table 11. Threshold voltage shifts (in mV) measured for MOS transistors contained in chips 50 and 53 after each of six Co-60 gamma irradiations. (Total doses are listed in Table 8.) These irradiations were performed before annealing.

Device Number	Gamma Irradiation Number					
	1	2	3	4	5	6
50/2	-0.4	0.8	-12.6	-43.2	-91.7	-110.0
50/3	-3.5	-3.8	-13.1	-32.1	-73.9	-107.0
50/4	-0.3	-0.6	-12.5	-31.5	-82.2	-121.0
50/9	-0.1	0.5	-7.1	-21.2	-56.1	-87.0
50/10	-0.1	-0.8	-11.8	-25.7	-65.8	-100.0
53/9	0.9	2.2	1.2	1.6	-1.0	15.9
53/10	-0.2	0.1	-2.1	-1.4	-5.8	8.2
53/11	1.7	1.7	-1.6	-11.1	-14.3	8.8
53/13	6.3	9.4	-1.9	1.6	-0.3	21.3

(Note that these chips had previously been irradiated to a neutron fluence of 9.6×10^{13} n/cm^2 and may have received considerable background ionizing radiation.) The ΔV_t values listed in the table are referenced to values of V_t measured before the Co-60 tests (i.e., after neutron exposure).

Devices contained in chip 53 showed very little change in V_t until the highest dose was reached, whereupon significant changes were noted and a sign reversal occurred. In the neutron bombardments, these devices exhibited saturation effects as shown in Figures 45 and 46 (53/10 and 53/11). The Co-60 results are consistent with those observations in that the devices remained in saturation until a sufficiently high dose was received to produce enough negatively charged interface states to compensate for the built-up positive charge in the gate oxide. Thus, results of Co-60 irradiations of transistors in chip 53 indicate that observations made on that chip in the neutron experiments were dominated by background ionizing radiation. The same conclusion can be made for chip 50. The monotonic, sublinear change in V_t noted in the neutron studies (see 50/10 in Figure 45) appeared to continue in the Co-60 experiments, with the onset of saturation becoming evident at the highest total dose.

Chips 50 and 53 were then annealed at 250°C for 20 min. at zero bias. Chip 50 was also annealed at 250°C for 20 min with -3 V gate bias applied. V_t values for chip 53 after anneal had recovered and were ~35 mV larger than pre-neutron-irradiation threshold voltages. Annealing attempts on chip 50 were unsuccessful; post-annealing values of V_t were actually less than before annealing.

A second series of Co-60 irradiations were then performed on five chips, and resulting threshold voltage shifts are listed in Table 12. Comparing results for the successfully annealed chip (53) with the previous neutron experiments (Table 10) suggests that the total ionizing dose received during the neutron exposures was ~5 x 10^4 rad(Si). For those chips that exhibited monotonic, sublinear changes in V_t in the Co-60 experiments (chip 50 pre-anneal and chips 43 and 49), more detailed calculations were performed* which yielded an average dose for the neutron experiments of ~7 x 10^4 rad(Si). It is then appropriate to examine the Co-60 data after adding that dose to those given in Tables 8 and 9, and after adding the ΔV_t values obtained following the fourth neutron irradiation to those given in Tables 11 and 12. Figure 47 shows typical examples of data plotted in that manner. ΔV_t values obtained in the neutron experiments are also shown. Total doses for those experiments are assumed to be proportional to the neutron fluence, with 9.6 x 10^{13} n/cm^2 being equated to an ionizing dose of 7 x 10^4 rad(Si). Devices 43/4 and 49/9 exhibit a continuation of the monotonic sublinear behavior evident in the neutron experiments, although the Co-60 incremental dose range examined is somewhat limited. Device 50/10 exhibits the onset of saturation beyond 10^5 rad(Si). Again the Co-60 results appear to be consistent with the neutron findings, which indicates that the latter experiments were dominated by background ionization.

---

*A linear relationship between neutron fluence and total ionizing dose was assumed. Next, ΔV_t values measured in the Co-60 experiments were plotted on straight-line extrapolations of fits (on log-log plots) to data obtained in the neutron experiments (e.g., 49/6 in Figure 45). With knowledge of the Co-60 doses, a straightforward calculation then yields the total dose received during neutron bombardment. This procedure yielded consistent values for moderate Co-60 doses. Deviations were noted at the highest doses which were probably due to the onset of saturation, i.e., deviation from the sublinear extrapolation. The value of 7 x 10^4 rad(Si) is an average based on calculations performed at moderate doses (1 to 3 x 10^4 rad).

Table 12. Threshold voltage shifts (in mV) measured for a population of MOS transistors after each of five Co-60 gamma irradiations. (Total doses are given in Table 9.) Irradiations of chips 50 and 53 were performed after an anneal. (See text for discussion.)

| DEVICE	GAMMA IRRADIATION NUMBER				
NUMBER	1	2	3	4	5
43/ 1	1.11	-1.33	-10.38	-38.46	-41.77
43/ 2	-1.84	-3.94	-10.54	-14.93	-28.44
43/ 3	-5.93	-10.86	-12.73	-20.42	-38.69
43/ 4	-2.32	-4.70	-8.32	-17.15	-37.34
43/ 5	-0.02	-0.72	-3.94	-12.82	-28.35
43/ 6	-2.92	-3.35	-9.31	-12.28	-27.34
43/ 9	-1.22	-4.18	-8.68	-14.05	-32.08
43/ 10	0.06	-2.24	-4.05	-9.77	-24.89
43/ 11	-1.69	-3.60	-6.21	-13.25	-29.67
43/ 12	-3.16	-3.65	-9.94	-18.35	-37.80
47/ 2	-2.85	-4.05	-6.01	-3.97	-5.84
47/ 3	-1.25	-2.37	-1.40	0.87	5.73
47/ 4	-0.24	-2.81	-4.95	-5.88	-7.85
47/ 5	-0.77	-0.77	-3.07	-6.06	-8.99
47/ 6	0.06	-1.29	-1.92	-6.55	-5.53
47/ 9	-1.04	-0.48	-2.93	-5.48	-8.98
49/ 2	-0.21	-2.46	-8.68	-14.40	-29.75
49/ 3	0.17	-1.93	-5.87	-14.66	-28.28
49/ 5	-1.79	-4.90	-5.97	-8.89	-17.78
49/ 6	0.25	-1.36	-2.81	-8.68	-13.91
49/ 9	0.44	-3.95	-6.02	-14.49	-34.38
49/ 11	-3.14	-5.39	-8.96	-18.34	-34.27
49/ 12	-1.55	-6.83	-11.22	-20.75	-57.50
49/ 13	1.53	-0.58	-7.15	-15.48	-45.57
50/ 2	-4.46	-7.69	-16.59	-31.30	-59.54
50/ 3	-1.61	-5.36	-12.59	-28.62	-71.71
50/ 4	-1.26	-3.49	-8.59	-16.97	-36.96
50/ 9	-0.82	-3.39	-7.31	-14.98	-30.70
50/ 10	-4.78	-7.43	-12.76	-25.42	-43.37
53/ 9	-1.80	-2.97	-5.47	-8.54	-17.66
53/ 10	-3.51	-3.81	-4.64	-11.48	-16.51
53/ 11	-1.92	-3.18	-6.85	-9.69	-16.69
53/ 13	-3.00	-4.61	-9.19	-16.17	-27.35
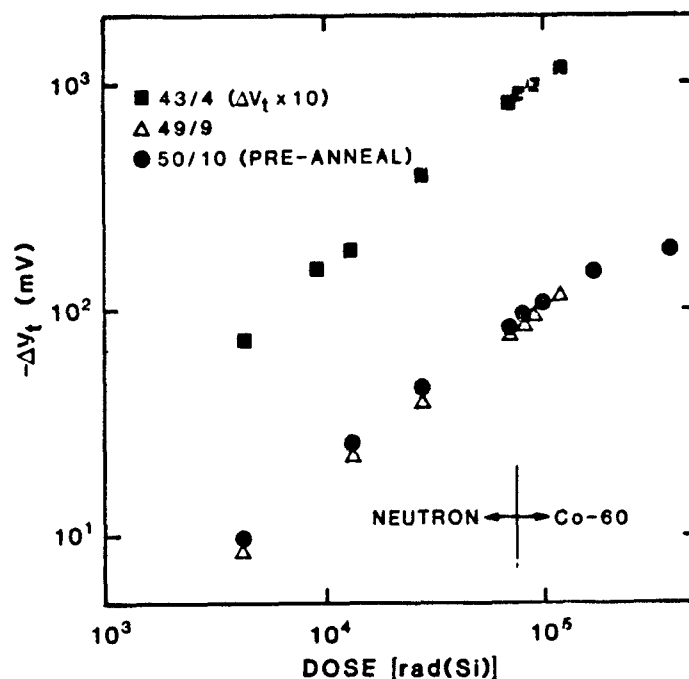
84s501

Figure 47. Threshold voltage shift vs ionizing dose for three MOS
transistors. Data obtained after both neutron bombard-
ment and Co-60 irradiation are shown. (See text for
discussion.) Values of -ΔVt for device 43/4 are
multiplied by 10 for clarity.
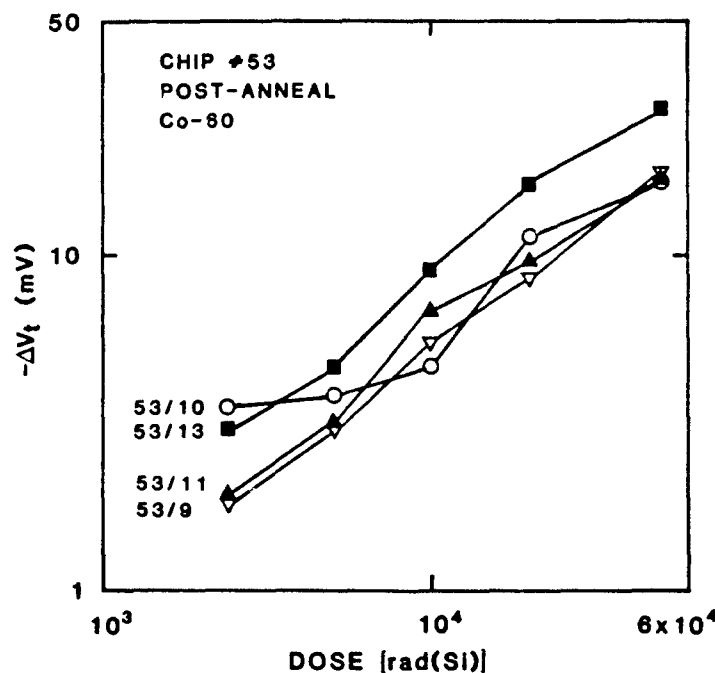
84s502

Figure 48. Threshold voltage shift vs Co-60 dose for
four MOS transistors in chip 53 after
annealing.

78

Figure 48 shows threshold voltage shift versus dose for chip 53 after annealing. (For this case, it is presumably appropriate to use the actual Co-60 doses and not add 7×10^4 rad to them.) Slope changes are evident for device 53/10, which suggests that the slope changes noted in a few cases during neutron irradiation (Figure 46) are not associated with single neutron interactions. However, further data are needed on other devices to substantiate this point. The occasional instabilities observed in the present device population (discussed above) make it difficult to be conclusive about the origin of the slope changes. In summary, electrical measurements on neutron-irradiated MOS/VLSI transistors appear to have been dominated by background ionizing radiation effects. It is not clear at present whether slope changes observed in plots of threshold voltage shift versus fluence are attributable to neutron interactions, to ionizing radiation, or to device instabilities.

4.5 SUMMARY

An experimental and analytical study of the effects of 14-MeV neutrons on silicon devices has been performed. Emphasis was placed on examining whether the permanent damage that results from a single neutron interaction could cause problems if that damage occurred in a sensitive region of a VLSI circuit. Determination of the energy and angular distributions of PKAs in 14-MeV neutron-irradiated silicon was made. These distributions were employed in a distributed cluster model that was used in an attempt to account for measured resistance changes in irradiated pinch resistors. Neutron irradiations of small-geometry bipolar transistors were also performed. Electrical measurements were dominated by damage produced in the extrinsic base region. An approach was developed for determining the effect on current gain of a single interaction in the intrinsic base region, and such experimentally-based calculations are planned. Neutron irradiations of MOS/VLSI transistors were performed. Observed threshold voltage shifts appeared to be largely attributable to background ionizing radiation present during the neutron irradiations. Slope changes were noted occasionally in plots of threshold voltage shift versus neutron fluence. Further study is needed to determine whether these slope changes are attributable to neutron interactions, to ionizing radiation, or to device instabilities.

SECTION 5

LIST OF REFERENCES

1. H.L. Hughes and R.A. Giroux, Electronics 37, 58 (1964).

2. Refer to the Dec. issues of IEEE Trans. Nucl. Sci. for extensive references.

3. M.H. Woods and R. Williams, J. Appl. Phys. 47, 1082 (1976).

4. J.M. Aitken, Final Report, RADC TR-81-113 (July 1981), pp. 49-64.

5. E.H. Nicollian, A. Goetzberger, and C.N. Berglund, Appl. Phys. Lett. 15, 174 (1969).

6. J. Lindmayer, IEEE Trans. Nucl. Sci. 18, 91 (Dec. 1971).

7. L. Manchanda, J. Vasi, and A.B. Bhattacharya, J. Appl. Phys. 52, 4690 (1981).

8. M. Bakowski, Physica Scripta 24, 410 (1981).

9. G.W. Hughes and J.H. Thomas III, Final Report, HDL-CR-79-159-1, Nov. 1981.

10. E. Harari, S. Wang, and B.S.H. Royce, J. Appl. Phys. 46, 1310 (1975).

11. E.H. Snow, A.S. Grove, and D.J. Fitzgerald, Proc. IEEE 55, 1168 (1967).

12. F.J. Grunthaner, B.F. Lewis, N. Zamini, and J. Maserjian, IEEE Trans. Nucl. Sci. NS-27, 1640 ('980); F.J. Grunthaner, P.J. Grunthaner, and J. Maserjian, IEEE Trans. Nucl. Sci. NS-29, 1462 (1982).

13. S.I. Raider and R. Flitsch, J. Electrochem. Soc. 123, 1754 (1976).

14. Thermally Stimulated Relaxation in Solids, P. Braünlich, Editor (Springer-Verlag, New York, 1979).

15. A.G. Milnes, Deep Impurities in Semiconductors (Wiley, New York, 1973).

16. J.T. Randall and M.H.F. Wilkins, Proc. Roy. Soc. (London) A184, 366, 390 (1945).

17. T.W. Hickmott, J. Appl. Phys. 46, 2583 (1975).

18. J.G. Simmons, G.W. Taylor, and M.C. Tam, Phys. Rev. B7, 3714 (1973).

19. A. Goetzberger, A.D. Lopez, and R.J. Strain, J. Electrochem. Soc. 120, 90 (1973).

20. M.R. Boudry and J.P. Stagg, J. Appl. Phys. 50, 942 (1979).

21. P.K. Nauta and M.W. Hillen, J. Appl. Phys. 49, 2862 (1978).

22. E.H. Nicollian and J.R. Brews, _MOS Physics and Technology_ (Wiley, New York, 1982), p. 794.

23. A. Goetzberger and H.E. Nigh, Proc. IEEE __54__, 1454 (1966).

24. Y. Miura and Y. Matukura, Japan J. Appl. Phys. __5__, 180 (1966).

25. N. Shiono, O. Nakajima, and C. Hashimoto, J. Electrochem. Soc. __130__, 138 (1983).

26. H.L. Hughes, IEEE Trans. Nucl. Sci. __NS-19__, 256 (1972); F.M. Fowkes and F.E. Witherell, IEEE Trans. Nucl. Sci. __NS-21__, 67 (1974).

27. C.M. Hsieh, P.C. Murley, and R.R. O'Brien, IEEE Elect. Dev. Lett. __EDL-2__, 103 (1981).

28. C.M. Hsieh, P.C. Murley, and R.R. O'Brien, IEEE Trans. Elect. Dev. __ED-30__, 636 (1983).

29. F.B. McLean and T.R. Oldham, IEEE Trans. Nucl. Sci. __29__, 2018 (1982).

30. J.R. Srour, S. Othmer, A. Bahraman, and R.A. Hartmann, IEEE Trans. Nucl. Sci. __28__, 3968 (1981).

31. S. Othmer, J.R. Srour, Z. Shanfield, R.A. Hartmann, M.A. Hopkins, A.H. Kalma and A. Bahraman, Report No. DNA 6178F-1, 1 August 1982.

32. D.I. Garber and R.R. Kinsey, "Neutron Cross Sections: Vol. II, Curves," BNL 325, Third Edition, January 1976.

33. D.I. Garber et al., "Angular Distributions in Neutron-Induced Reactions: Volume I, Z = 1 to 20," BNL 400, Third Edition, January 1970.

34. H.J. Stein, J. Appl. Phys. __38__, 204 (1967).

35. L.D. Landau and E.M. Lifshitz, _Mechanics_ (Pergamon, Oxford, 1960).

36. P.L. Meyer, _Introductory Probability and Statistical Applications_ (Addison-Wesley, Reading, 1965), pp. 77, 95.

37. C.M. Lederer, J.M. Hollander, and I. Perlman, _Table of Isotopes_ (Wiley, New York, 1968).

38. W. Hauser and H. Feshbach, Phys. Rev. __87__, 366 (1952).

39. B.R. Gossick, J. Appl. Phys. __30__, 1214 (1959).

40. G.P. Mueller, N.D. Wilsey, and M. Rosen, IEEE Trans. Nucl. Sci. __29__, 1493 (1982).

41. I. Manning and G.P. Mueller, Computer Phys. Comm. __7__, 85 (1974).

42. J.R. Srour, IEEE Trans. Nucl. Sci. __20__, 190 (Dec. 1973).

81

DISTRIBUTION LIST

DEPARTMENT OF DEFENSE

Assistant to the Secretary of Defense, Atomic Energy
    ATTN: Executive Assistant

Commander in Chief, Atlantic
    ATTN: J7

Defense Advanced Rsch Proj Agency
    ATTN: J. Fraser
    ATTN: R. Reynolds
    ATTN: S. Roosild

Defense Communications Engineer Center
    ATTN: Code R410
    ATTN: Code R720, C. Stansberry

Defense Electronic Supply Center
    ATTN: DEFC-ESA

Defense Intelligence Agency
    ATTN: DB-4C, Rsch, Phys Vuln Br
    ATTN: DT-1B
    ATTN: RTS-2B

Defense Logistics Agency
    ATTN: DLA-QEL, K. Mason
    ATTN: DLA-SEE, F. Harris

Defense Nuclear Agency
  3 cys ATTN: RAEV, Tree
  4 cys ATTN: STTI-CA

Defense Technical Information Center
  12 cys ATTN: DD

Field Command, Defense Nuclear Agency, Det 2
Lawrence Livermore National Lab
    ATTN: FC-1

DNA PACOM Liaison Office
    ATTN: J. Bartlett

Field Command, Defense Nuclear Agency
    ATTN: FCPF, R. Blackburn
    ATTN: FCPR
    ATTN: FCTT
    ATTN: FCTT, W. Summa
    ATTN: FCTXE

Joint Chiefs of Staff
    ATTN: C3S Evaluation Office, HD00

Joint Data System Support Ctr
    ATTN: C-312, R. Mason
    ATTN: C-330

Joint Strat Tgt Planning Staff
    ATTN: JLK, DNA Rep
    ATTN: JLKS
    ATTN: JPPFD
    ATTN: JPTM

National Communications System
    ATTN: NCS-TS
    ATTN: NCS-TS, P. Bodson

DEPARTMENT OF DEFENSE (Continued)

National Security Agency
    ATTN: P-3, R. Light
    ATTN: R-54, O. Van Gunten
    ATTN: S-4, T. Neal
    ATTN: S-5, J. Hilton
    ATTN: S-6, T. Brown

Under Secy of Def for Rsch & Engrg
    ATTN: Strat & Space Sys (OS)
    ATTN: Strat & Theater Nuc For, F. Vajda

DEPARTMENT OF THE ARMY

Applied Sciences Division
    ATTN: R. Williams

BMD Advanced Technology Center
    ATTN: ATC-O, F. Hoke
    ATTN: ATC-T

BMD Systems Command
    ATTN: BMDSC-AV, J. Harper
    ATTN: BMDSC-HW
    ATTN: BMDSC-HW, R. DeKalb
    ATTN: BMDSC-LEE, R. Webb

Commander, Fort Huachuca
    ATTN: Tech Ref Div

Harry Diamond Laboratories
    ATTN: C. Fazi
    ATTN: DELHD-NW-EA, J. Miletta
    ATTN: DELHD-NW-P, T. Flory
    ATTN: DELHD-NW-R, F. McLean, 22300
    ATTN: DELHD-NW-RH
    ATTN: SLCHD-NW-EC
    ATTN: SLCHD-NW-P
    ATTN: SLCHD-NW-R
    ATTN: SLCHD-NW-RA
    ATTN: SLCHD-NW-RC
    ATTN: T. Taylor
  2 cys ATTN: DELHD-NW-RA, W. Vault

US Army Armament Rsch Dev & Cmd
    ATTN: DRDAR-LCA-PD
    ATTN: DRDAR-LCN-F
    ATTN: DRDAR-TSI-E, A. Grinoch
    ATTN: DRDAR-TSS, Tech Div

US Army Armor & Engineer Board
    ATTN: ATZK-AE-AR, J. Dennis

US Army Ballistic Research Lab
    ATTN: DRDAR-BLB, W. Van Antwerp
    ATTN: DRDAR-BLT
    ATTN: DRDAR-BLV, D. Rigotti

US Army Chemical School
    ATTN: ATZN-CM-CS

US Army Communications R&D Command
    ATTN: DELET-IR, E. Hunter
    ATTN: DRSEL-NL-RO, R. Brown

DEPARTMENT OF THE ARMY (Continued)

US Army Engineer Div Huntsville
    ATTN: HNDED-ED, J. Harper

US Army Material & Mechanics Rsch Ctr
    ATTN: DRXMR-B, J. Hofmann
    ATTN: DRXMP-HH, J. Dignam

US Army Mobility Equip R&D Cmd
    ATTN: DRDME-E, J. Bond, Jr

US Army Nuclear & Chemical Agency
    ATTN: Library

US Army Research Office
    ATTN: R. Griffith

US Army Signal Warfare Lab
    ATTN: DELSW-D-OS
    ATTN: K. Erwin

US Army Test and Evaluation Comd
    ATTN: DRSTE-CM-F
    ATTN: DRSTE-CT-C

US Army Tradoc Sys Analysis Actvy
    ATTN: ATAA-TFC, O. Miller

US Army Training and Doctrine Comd
    ATTN: ATCD-Z

US Army White Sands Missile Range
    ATTN: STEWS-TE-AN, A. De La Paz
    ATTN: STEWS-TE-AN, J. Meason
    ATTN: STEWS-TE-AN, R. Dutchover
    ATTN: STEWS-TE-AN, R. Hays
    ATTN: STEWS-TE-N, K. Cummings
    ATTN: STEWS-TE-N, T. Arellanes
    ATTN: STEWS-TE-NT, M. Squires

USA Missile Command
    ATTN: AMSMI-SF, G. Thurlow
    ATTN: DRCPM-PE-EA, W. Wagner
    ATTN: Hawk Project Officer, DRCPM-HAER
3 cys ATTN: Documents Section

USA Night Vision & Electro-Optics Lab
    ATTN: DRSEL-NV-SD, A. Parker
    ATTN: DRSEL-NV-SD, J. Carter

XM-1 Tank System
    ATTN: DRCPM-GCM-SW

DEPARTMENT OF THE NAVY

Naval Air Systems Command
    ATTN: AIR 310
    ATTN: AIR 350F
    ATTN: AIR 54053

Naval Avionics Center
    ATTN: Code B415, D. Repass

Naval Intelligence Support Ctr
    ATTN: NISC Library

Naval Ocean Systems Center
    ATTN: Code 4471, Tech Lib

DEPARTMENT OF THE NAVY (Continued)

Naval Postgraduate School
    ATTN: Code 1424, Library

Naval Research Laboratory
    ATTN: Code 2627
    ATTN: Code 4040, J. Boris
    ATTN: Code 4154, J. Adams
    ATTN: Code 6600, D. Nagel
    ATTN: Code 6610, J. Ritter
    ATTN: Code 6611, E. Petersen
    ATTN: Code 6612, D. Walker
    ATTN: Code 6612, R. Statler
    ATTN: Code 6613, A. Campbell
    ATTN: Code 6614, L. August
    ATTN: Code 6614, P. Shapiro
    ATTN: Code 6652, G. Mueller
    ATTN: Code 6653, A. Namenson
    ATTN: Code 6673, A. Knudson
    ATTN: Code 6682, C. Dozier
    ATTN: Code 6682, D. Brown
    ATTN: Code 6701
    ATTN: Code 6810, J. Killiany
    ATTN: Code 6813, N. Saks
    ATTN: Code 6813, W. Jenkins
    ATTN: Code 6814, M. Peckerar
    ATTN: Code 6816, E. Richmond
    ATTN: Code 6816, H. Hughes
    ATTN: Code 6816, R. Hevey
    ATTN: Code 6816, R. Lambert
    ATTN: Code 6814, D. McCarthy

Naval Sea Systems Command
    ATTN: SEA-06J, R. Lane

Naval Surface Weapons Center
    ATTN: Code F30
    ATTN: Code F31
    ATTN: Code F31, F. Warnock
    ATTN: Code F31, K. Caudle
    ATTN: Code WA-52, R. Smith
    ATTN: F31, J. Downs

Naval Weapons Center
    ATTN: Code 343, FKA6A2, Tech Svcs

Naval Weapons Evaluation Facility
    ATTN: Code AT-6

Naval Weapons Support Center
    ATTN: Code 3073, T. Ellis
    ATTN: Code 605, J. Ramsey
    ATTN: Code 6054, D. Platteter

Nuclear Weapons Tng Group, Pacific
    ATTN: Code 32

Ofc of the Dep Asst Sec of the Navy
    ATTN: L. Abella

Ofc of the Deputy Chief of Naval Ops
    ATTN: NOP 985F

Office of Naval Research
    ATTN: Code 220, D. Lewis
    ATTN: Code 414, L. Cooper
    ATTN: Code 427

DEPARTMENT OF THE NAVY (Continued)

Space & Naval Warfare Systems Cmd
    ATTN: Code 5045.11, C. Suman
    ATTN: Code 50451
    ATTN: Navalex 51024, C. Watkins
    ATTN: PME 117-21

Strategic Systems Program
    ATTN: NSP-2301, M. Meserole
    ATTN: NSP-2430, J. Stillwell
    ATTN: NSP-2701
    ATTN: NSP-27331
    ATTN: NSP-27334

DEPARTMENT OF THE AIR FORCE

Aeronautical Systems Division
    ATTN: ASD/ENACC, R. Fish
    ATTN: ASD/ENESS, P. Marth
    ATTN: ASD/YH-EX, J. Sunkes

Air Force Geophysics Laboratory
    ATTN: PHG, M/S 30, E. Mullen
    ATTN: PLIG, R. Filz
    ATTN: SULL
    ATTN: SULL S-29

Air Force Institute of Technology
    ATTN: ENP, J. Bridgeman
    ATTN: J. Prince
    ATTN: Library

Air Force Systems Command
    ATTN: DLCAM
    ATTN: DLW

Air Force Technical Applications Ctr
    ATTN: TAE

Air Force Weapons Laboratory
    ATTN: NTAEE, C. Baum
    ATTN: NTC, M. Schneider
    ATTN: NTCAS, J. Ferry
    ATTN: NTCAS, J. Mullis
    ATTN: NTCOX, R. Tallon
    ATTN: NTCT, G. Goss
    ATTN: NTCTR, K. Hunt
    ATTN: NTCTR, R. Maier
    ATTN: SUL

Air Force Wright Aeronautical Lab
    ATTN: POD, P. Stover
    ATTN: POE-2, J. Wise

Air Force Wright Aeronautical Lab
    ATTN: DHE
    ATTN: DHE-2
    ATTN: LPO, R. Hickmott
    ATTN: LTE

Air Logistics Command
    ATTN: MMEDD
    ATTN: MMETH
    ATTN: MMETH, R. Blackburn
    ATTN: MMGRW, G. Fry
    ATTN: MMIFM, S. Mallory
    ATTN: OO-ALC/MM

Air University Library
    ATTN: AUL-LSE

DEPARTMENT OF THE AIR FORCE (Continued)

Assistant Chief of Staff, Studies & Analysis
2 cys ATTN: AF/SAMI, Tech Info Div

Ballistic Missile Office
    ATTN: ENSN, H. Ward
    ATTN: ENBE
    ATTN: ENMG
    ATTN: ENSN
    ATTN: ENSN, M. Williams
    ATTN: ENSN, W. Wilson
    ATTN: SYST
    ATTN: SYST, L. Bryant

Electronic Systems Division
    ATTN: INDC

Foreign Technology Division
    ATTN: TQTD, B. Ballard

Office of Space Systems
    ATTN: Director

Oklahoma City Air Logistics Ctr
    ATTN: DMM, R. Wallis

Rome Air Development Center
    ATTN: RBR, J. Brauer
    ATTN: RBRP, C. Lane

Rome Air Development Center
    ATTN: ESE, A. Kahan
    ATTN: ESR, B. Buchanan
    ATTN: ESR, J. Bradford, M/S 64
    ATTN: ESR, J. Schott
    ATTN: ESR, W. Shedd

Sacramento Air Logistics Center
    ATTN: MMEAE, R. Dallinger

Space Division
    ATTN: ALT
    ATTN: CFCT
    ATTN: YB
    ATTN: YD
    ATTN: YE
    ATTN: YG
    ATTN: YK
    ATTN: YKA, C. Kelly
    ATTN: YKS, P. Stadler
    ATTN: YN

Strategic Air Command
    ATTN: INAO
    ATTN: NRI/STINFO
    ATTN: XPFC
    ATTN: XPFS

Tactical Air Command
    ATTN: XPG

3416th Technical Training Squadron
    ATTN: TTV

DEPARTMENT OF ENERGY

Department of Energy
Albuquerque Operations Office
    ATTN: WSSB
    ATTN: WSSB, R. Shay

DEPARTMENT OF ENERGY (Continued)

University of California
Lawrence Libermore National Lab
    ATTN: L-10, H. Kruger
    ATTN: L-13, D. Meeker
    ATTN: L-156, J. Yee
    ATTN: L-156, R. Kalibjian
    ATTN: Technical Info Dept Library
    ATTN: W. Orvis

Los Alamos National Laboratory
    ATTN: D. Lynn
    ATTN: MS K 551, E. Leonard

Sandia National Laboratories
    ATTN: Div 1232, G. Baldwin
    ATTN: Org 2100, B. Gregory
    ATTN: Org 2110, W. Dawes
    ATTN: Org 2115, J. Gover
    ATTN: Org 2143, T. Dellon
    ATTN: Org 2144, P. Dressendorfer
    ATTN: Org 2150, J. Hood
    ATTN: Org 2320, J. Renken
    ATTN: Org 2321, L. Posey
    ATTN: Org 5143, J. Duncan
    ATTN: T. Wrobel

OTHER GOVERNMENT AGENCIES

Central Intelligence Agency
    ATTN: OSWR, T. Marquitz
    ATTN: OSWR/NED
    ATTN: OSWR/STD/MTB

Federal Aviation Administration
    ATTN: ARD-350

NASA, Goddard Space Flight Center
    ATTN: Code 311.3, D. Cleveland
    ATTN: Code 311A, J. Adolphsen
    ATTN: Code 601, E. Stassinopoulos
    ATTN: Code 654.2, V. Danchenko
    ATTN: Code 660, J. Trainor
    ATTN: Code 695, M. Acuna
    ATTN: Code 701, W. Redisch
    ATTN: Code 724.1, M. Jhabvala

NASA, George C. Marshall Space Flight Center
    ATTN: EG02
    ATTN: H. Yearwood
    ATTN: M. Nowakowski

NASA, Lewis Research Center
    ATTN: M. Baddour

NASA Headquarters
    ATTN: Code DP, B. Bernstein
    ATTN: Cude DP, R. Karpen

Department of Commerce
    ATTN: C. Wilson
    ATTN: Code A305, K. Galloway
    ATTN: Code A327, H. Schafft
    ATTN: Code A347, J. Mayo-Wells
    ATTN: Code A353, S. Chappell
    ATTN: Code A361, J. French
    ATTN: Code C216, J. Humphreys
    ATTN: T. Russell

DEPARTMENT OF DEFENSE CONTRACTORS

Advanced Research & Applications Corp
    ATTN: L. Palkuti
    ATTN: R. Armistead
    ATTN: T. Magee

Aerojet Electro-Systems Co
    ATTN: D. Toomb
    ATTN: P. Lathrop
    ATTN: SV/8711/70

Aerospace Corp
    ATTN: A. Carlan
    ATTN: B. Blake
    ATTN: D. Fresh
    ATTN: D. Schmunk
    ATTN: G. Gilley
    ATTN: I. Garfunkel
    ATTN: J. Reinheimer
    ATTN: J. Stoll
    ATTN: J. Weisner
    ATTN: M. Daugherty
    ATTN: P. Buchman
    ATTN: R. Crolius
    ATTN: R. Slaughter
    ATTN: S. Bower
    ATTN: V. Josephson
    ATTN: W. Crane, A2/1083
    ATTN: W. Kolasinski, MS/259

Aerospace Industries Assoc of America, Inc
    ATTN: S. Siegel

Allied Corp
    ATTN: Document Control

Allied Corp
    ATTN: E. Meeder

Allied Corp
    ATTN: M. Frank

Ampex Corp
    ATTN: K. Wright
    ATTN: P. Peyrot

Analytic Services, Inc, ANSER
    ATTN: A. Shostak
    ATTN: J. O'Sullivan
    ATTN: P. Szymanski

Applied Systems Engrg Director
    ATTN: J. Retzler, Nuc S/V Mang

AVCO Systems Division
    ATTN: C. Davis
    ATTN: D. Fann
    ATTN: D. Shrader
    ATTN: W. Broding

Battelle Memorial Institute
    ATTN: R. Thatcher

BDM Corp
    ATTN: C. Stickley
    ATTN: S. Meth

DEPARTMENT OF DEFENSE CONTRACTORS (Continued)

BDM Corp
    ATTN: D. Wunsch
    ATTN: Marketing
    ATTN: R. Antinone

Beers Associates, Inc
    ATTN: B. Beers
    ATTN: S. Ives

Bell Labs
    ATTN: D. Yaney
    ATTN: R. McPartland

Boeing Aerospace Co
    ATTN: M. Anaya, M/S 2A-87

Boeing Co
    ATTN: D. Egelkrout
    ATTN: H. Wicklein
    ATTN: R. Caldwell
    ATTN: 8K-38

Boeing Co
    ATTN: C. Dixon
    ATTN: MS-2R-00, A. Johnston
    ATTN: MS-2R-00, C. Rosenberg
    ATTN: MS-2R-00, E. Smith
    ATTN: MS-2R-00, I. Arimura
    ATTN: MS-81-36, P. Blakely
    ATTN: MS-81-36, W. Doherty
    ATTN: O. Mulkey

Booz-Allen & Hamilton, Inc
    ATTN: R. Chrisner

California Institute of Technology
    ATTN: A. Shumka
    ATTN: D. Nichols, T-1180
    ATTN: F. Grunthaner
    ATTN: J. Coss
    ATTN: K. Martin
    ATTN: P. Robinson
    ATTN: R. Covey
    ATTN: W. Price, MS-83-122
    ATTN: W. Scott

Calspan Corp
    ATTN: R. Thompson

Charles Stark Draper Lab, Inc
    ATTN: A. Freeman
    ATTN: J. Boyle
    ATTN: N. Tibbetts
    ATTN: P. Greiff
    ATTN: R. Bedingfield
    ATTN: R. Haltmaier
    ATTN: R. Ledger
    ATTN: Tech Library
    ATTN: W. Callender

Cincinnati Electronics Corp
    ATTN: L. Hammond

Clarkson College of Technology
    ATTN: P. McNulty

Computer Sciences Corp
    ATTN: A. Schiff

Control Data Corp
    ATTN: D. Newberry, BRR 142

University of Denver, Colorado Seminary
    ATTN: Sec Officer for F. Venditti

Develco, Inc
    ATTN: G. Hoffman

Dikewood Corp
    ATTN: Tech Lib for D. Pirio

E-Systems, Inc
    ATTN: K. Reis

E-Systems, Inc
    ATTN: Division Library

Eaton Corp
    ATTN: A. Anthony
    ATTN: R. Bryant

Electronic Industries Association
    ATTN: J. Kinn

FMC Corp
    ATTN: M. Pollock, MD 080

Ford Aerospace & Communications Corp
    ATTN: H. Linder
    ATTN: Technical Info Services

Garrett Corp
    ATTN: H. Weil

General Dynamics Corp
    ATTN: O. Wood
    ATTN: R. Fields, MZ 2839

General Electric Co
    ATTN: D. Tasca
    ATTN: J. Peden
    ATTN: R. Benedict
    ATTN: R. Casey
    ATTN: Technical Info Ctr for L. Chasen
    ATTN: Technical Library

General Electric Co
    ATTN: B. Flaherty
    ATTN: G. Bender
    ATTN: L. Hauge

General Electric Co
    ATTN: G. Gati, MD-E184

General Electric Co
    ATTN: C. Hewison
    ATTN: D. Cole

General Electric Co
    ATTN: D. Pepin

General Research Corp
    ATTN: A. Hunt

George Washington University
    ATTN: A. Friedman

Georgia Institute of Technology
    ATTN: Res & Sec Coord for H. Denny

Goodyear Aerospace Corp
    ATTN: Security Control Station

Grumman Aerospace Corp
    ATTN: J. Rogers

GTE Communications Products Corp
    ATTN: H & V Group
    ATTN: J. McElroy
    ATTN: P. Fredrickson

GTE Communications Products Corp
    ATTN: F. Krch

GTE Communications Products Corp
    ATTN: J. Waldron
    ATTN: M. Snow
    ATTN: W. Dunnett

GTE Government Systems Corp
    ATTN: L. Lesinski
    ATTN: L. Pauplis

Harris Corp
    ATTN: E. Yost
    ATTN: W. Abare

Harris Corp
    ATTN: B. Gingerich, MS-51-120
    ATTN: C. Anderson
    ATTN: D. Williams, MS-51-75
    ATTN: J. Cornell
    ATTN: J. Schroeder
    ATTN: Mgr Linear Engineering
    ATTN: Mngr Bipolar Digital Eng
    ATTN: T. Sanders, MS-51-121

Honeywell, Inc
    ATTN: D. Nielsen, MN 14-3015
    ATTN: J. Moylan
    ATTN: R. Gumm

Honeywell Inc
    ATTN: H. Noble
    ATTN: J. Schafer
    ATTN: J. Zawacki
    ATTN: MS 725-5
    ATTN: R. Reinecke

Honeywell, Inc
    ATTN: Technical Library

Honeywell, Inc
    ATTN: L. Lavoie

Honeywell, Inc
    ATTN: D. Herold, MS-MN 17-2334
    ATTN: D. Lamb, MS-MN 17-2334
    ATTN: R. Belt, MS-MN 17-2334

Hughes Aircraft Co
    ATTN: B. Campbell, E1/E110
    ATTN: D. Binder
    ATTN: R. McGowan

Hughes Aircraft Co
    ATTN: R. Henderson

Hughes Aircraft Co
    ATTN: MS-A2408, J. Hall

Hughes Aircraft Intl Svc Co
    ATTN: A. Narevsky, S32/C332
    ATTN: D. Shumake
    ATTN: F. Kubo
    ATTN: W. Scott, S32/C332

IBM Corp
    ATTN: Electromagnetic Compatibility
    ATTN: H. Mathers
    ATTN: Mono Memory Systems
    ATTN: T. Martin

IBM Corp
    ATTN: J. Ziegler

IBM Corp
    ATTN: A. Edenfeld
    ATTN: H. Kotecha
    ATTN: L. Rockett, MS 110-020
    ATTN: MS 110-036, F. Tietze
    ATTN: N. Haddad
    ATTN: O. Spencer
    ATTN: W. Doughten
    ATTN: W. Henley

IIT Research Institute
    ATTN: I. Mindel
    ATTN: R. Sutkowski

Illinois Computer Research, Inc
    ATTN: E. Davidson

Institute for Defense Analyses
    ATTN: Tech Info Services

Intel Corp
    ATTN: T. May

IRT Corp
    ATTN: J. Azarewicz
    ATTN: J. Harrity
    ATTN: M. Rose
    ATTN: MDC
    ATTN: N. Rudie
    ATTN: Physics Division
    ATTN: R. Mertz
    ATTN: Systems Effects Division

JAYCOR
    ATTN: M. Treadaway
    ATTN: R. Berger
    ATTN: R. Stahl
    ATTN: T. Flanagan

JAYCOR
    ATTN: R. Sullivan

JAYCOR
    ATTN: C. Rogers
    ATTN: R. Poll

Johns Hopkins University
    ATTN: P. Partridge
    ATTN: R. Maurer

Johns Hopkins University
    ATTN: G. Masson, Dept of Elec Engr

Kaman Sciences Corp
    ATTN: C. Baker
    ATTN: Dir Science & Technology Div
    ATTN: J. Erskine
    ATTN: N. Beauchamp
    ATTN: W. Rich

Kaman Sciences Corp
    ATTN: E. Conrad

Kaman Tempo
    ATTN: DASIAC
    ATTN: R. Rutherford
    ATTN: W. McNamara

Kaman Tempo
    ATTN: DASIAC

Litton Systems, Inc
    ATTN: E. Zimmerman
    ATTN: F. Motter

Lockheed Electronics Co, Inc
    ATTN: R. Corn

Lockheed Georgia Co
    ATTN: Dept 662 Zone 22, E. Harris

Lockheed Missiles & Space Co, Inc
    ATTN: F. Junga, 95-43
    ATTN: J. Smith
    ATTN: Reports Library

Lockheed Missiles & Space Co, Inc
    ATTN: A. Borofsky, Dept 66-60, B/577N
    ATTN: B. Kimura
    ATTN: E. Hessee
    ATTN: J. Lee
    ATTN: J. Cayot, Dept 81-63
    ATTN: L. Rossi
    ATTN: P. Bene
    ATTN: S. Taimuty, Dept 81-74/154

LTV Aerospace & Defense Company
    ATTN: Library
    ATTN: R. Tomme
    ATTN: Technical Data Center

M I T Lincoln Lab
    ATTN: P. McKenzie

Magnavox Advanced Products & Sys Co
    ATTN: W. Hagemeier

Magnavox Govt & Indus Electronics Co
    ATTN: W. Richeson

Martin Marietta Denver Aerospace
    ATTN: Goodwin
    ATTN: MS-D6074, M. Polzella
    ATTN: P. Kase
    ATTN: R. Anderson
    ATTN: Research Library

Martin Marietta Corp
    ATTN: H. Cates
    ATTN: J. Tanke
    ATTN: J. Ward
    ATTN: MP-163, W. Bruce
    ATTN: R. Gaynor
    ATTN: R. Yokomoto
    ATTN: S. Bennett
    ATTN: TIC/MP-30
    ATTN: W. Brockett

Martin Marietta Corp
    ATTN: T. Davis

University of Maryland
    ATTN: H. Lin

McDonnell Douglas Corp
    ATTN: A. Munie
    ATTN: D. Dohm
    ATTN: Library
    ATTN: M. Stitch, Dept E003
    ATTN: R. Kloster, Dept E451
    ATTN: T. Ender, 33/6/618

McDonnell Douglas Corp
    ATTN: D. Fitzgerald
    ATTN: J. Imai
    ATTN: M. Onoda
    ATTN: M. Ralsten
    ATTN: P. Albrecht
    ATTN: P. Bretch
    ATTN: R. Lothringer

McDonnell Douglas Corp
    ATTN: Technical Library

George C. Messenger, Consulting Engineer
    ATTN: G. Messenger

Mission Research Corp
    ATTN: C. Longmire
    ATTN: M. Van Blaricum

Mission Research Corp
    ATTN: D. Alexander
    ATTN: D. Merewether
    ATTN: R. Pease
    ATTN: R. Turfler

Mission Research Corp
    ATTN: J. Lubell
    ATTN: R. Curry
    ATTN: W. Ware

Mission Research Corp, San Diego
    ATTN: J. Raymond
    ATTN: V. Van Lint

Mitre Corp
    ATTN: M. Fitzgerald

Motorola, Inc
    ATTN: A. Christensen

Motorola, Inc
    ATTN: C. Lund
    ATTN: L. Clark
    ATTN: O. Edwards

National Academy of Sciences
    ATTN: National Materials Advisory Board

National Semiconductor Corp
    ATTN: F. Jones

University of New Mexico
    ATTN: H. Southward

New Technology, Inc
    ATTN: D. Divis

Norden Systems, Inc
    ATTN: Technical Library

Northrop Corp
    ATTN: A. Bahraman
    ATTN: J. Srour
    ATTN: P. Eisenberg
    ATTN: S. Othmer
    ATTN: Z. Shanfield
    ATTN: M. Hopkins
    ATTN: R. Hartmann
    ATTN: D. Newberry

Northrop Corp
    ATTN: E. King, C3323/WC
    ATTN: L. Apodaca
    ATTN: P. Gardner
    ATTN: S. Stewart
    ATTN: T. Jackson

Pacific-Sierra Research Corp
    ATTN: H. Brode, Chairman SAGE

Palisades Inst for Rsch Services, Inc
    ATTN: Secretary

Physics International Co
    ATTN: Division 6000
    ATTN: J. Shea

Power Conversion Technology, Inc
    ATTN: V. Fargo

R & D Associates
    ATTN: P. Haas
    ATTN: W. Karzas

Rand Corp
    ATTN: C. Crain
    ATTN: P. Davis

Rand Corp
    ATTN: B. Bennett

Raytheon Co
    ATTN: G. Joshi
    ATTN: J. Ciccio
    ATTN: T. Wein

Raytheon Co
    ATTN: A. Van Doren
    ATTN: H. Flescher

RCA Corp
    ATTN: G. Brucker
    ATTN: V. Mancino

RCA Corp
    ATTN: Office N103
    ATTN: R. Smeltzer

RCA Corp
    ATTN: R. Killion

RCA Corp
    ATTN: E. Schmitt
    ATTN: L. Debacker
    ATTN: W. Allen

RCA Corp
    ATTN: E. Van Keuren
    ATTN: J. Saultz
    ATTN: R. Magyarics
    ATTN: W. Heagerty

Rensselaer Polytechnic Institute
    ATTN: R. Gutmann
    ATTN: R. Ryan

Research Triangle Institute
    ATTN: M. Simons

Rockwell International Corp
    ATTN: A. Rovell
    ATTN: GA50 TIC, L. Green
    ATTN: J. Bell
    ATTN: J. Blandford
    ATTN: J. Burson
    ATTN: J. Pickel, Code 031-BB01
    ATTN: K. Hull
    ATTN: R. Pancholy
    ATTN: V. De Martino
    ATTN: V. Strahan

Rockwell International Corp
    ATTN: D. Stevens
    ATTN: TIC D/41-092 AJ01

Rockwell International Corp
    ATTN: L. Pinkston, 106-183
    ATTN: TIC 124-203

Rockwell International Corp
    ATTN: T. Yates
    ATTN: TIC BA08

Sanders Associates, Inc
    ATTN: L. Brodeur

Science Applications Intl Corp
    ATTN: D. Long
    ATTN: D. Millward
    ATTN: D. Strobel
    ATTN: J. Beyster
    ATTN: J. Naber
    ATTN: J. Retzler
    ATTN: J. Spratt
    ATTN: L. Scott
    ATTN: R. Fitzwilson
    ATTN: V. Orphan
    ATTN: V. Verbinski

Science Applications Intl Corp
    ATTN: J. Wallace
    ATTN: W. Chadsey

DEPARTMENT OF DEFENSE CONTRACTORS (Continued)

Science Applications, Inc
    ATTN: D. Stribling

Scientific Research Assoc, Inc
    ATTN: H. Grubin

Signetics Corp
    ATTN: J. Lambert

Singer Co
    ATTN: J. Brinkman
    ATTN: R. Spiegel
    ATTN: Technical Information Center

Sperry Corp
    ATTN: Engineering Laboratory

Sperry Corp
    ATTN: J. Inda

Sperry Corp
    ATTN: C. Craig
    ATTN: F. Scaravaglione
    ATTN: P. Maraffino
    ATTN: R. Viola

Sperry Corp
    ATTN: D. Schow

SRI International
    ATTN: A. Whitson
    ATTN: M. Tarrasch

SRI International
    ATTN: A. Padgett

Sundstrand Corp
    ATTN: C. White
    ATTN: Research Department

System Development Corp
    ATTN: Product Evaluation Laboratory

Systron-Donner Corp
    ATTN: J. Indelicato

Teledyne Systems Co
    ATTN: R. Suhrke

Teledyne Brown Engineering
    ATTN: B. Hartway
    ATTN: D. Guice

Texas Instruments, Inc
    ATTN: D. Manus
    ATTN: D. Mercer
    ATTN: E. Jeffrey, MS 961
    ATTN: F. Poblenz, MS 3143
    ATTN: R. Carroll, MS 3143
    ATTN: R. McGrath
    ATTN: R. Stehlin
    ATTN: T. Cheek, MS 3143

TRW Electronics & Defense Sector
    ATTN: A. Witteles, MS R1/2144
    ATTN: D. Clement
    ATTN: F. Friedt
    ATTN: H. Holloway
    ATTN: M. Ash
    ATTN: P. Guilfoyle
    ATTN: P. Reid, MS R6/2541
    ATTN: R. Kingsland
    ATTN: R. Von Hatten
    ATTN: Technical Information Center
    ATTN: W. Adelman
    ATTN: W. Rowan
    ATTN: W. Willis
2 cys ATTN: O. Adams
2 cys ATTN: R. Plebuch

TRW Electronics & Defense Sector
    ATTN: C. Blasnek
    ATTN: F. Fay
    ATTN: J. Gorman

Westinghouse Electric Corp
    ATTN: E. Vitek, MS 3200
    ATTN: H. Kalapaca, MS 3330
    ATTN: J. Cricchi
    ATTN: L. McPherson
    ATTN: MS 330, D. Grimes
    ATTN: MS 3330
    ATTN: N. Bluzer

Westinghouse Electric Corp
    ATTN: S. Wood